STUDYING THE ROLE OF THE DIVALENT METAL CATION ACTIVATOR OF THE CAMBIALISTIC ENZYME MANDELATE RACEMASE

by

Matthew L. Harty

Submitted in partial fulfilment of the requirements
for the degree of Master of Science

at

Dalhousie University
Halifax, Nova Scotia
July 2015

© Copyright by Matthew L. Harty, 2015

TABLE OF CONTENTS

LIST OF FIGURES

LIST OF TABLES

LIST OF SCHEMES

ABSTRACT

Mandalate racemase (MR) from *Pseudomonas putida* requires a divalent metal cation, usually Mg^{2+}, to catalyze the interconversion of the enantiomers of mandelate. Typical of a cambialistic enzyme, the active site Mg^{2+} may be replaced by other metal ions. Replacement by Co^{2+}, Ni^{2+}, and Mn^{2+} does not significantly alter the kinetic parameters K_m^{app}, k_{cat}^{app}, and $(k_{cat}/K_m)^{app}$ for the substrates (*R*)– and (*S*)–mandelate, and the alternative substrate (*S*)–trifluorolactate. The competitive inhibition constants (K_i) for inhibition of each metalloenzyme by benzohydroxamate did not vary significantly with the identity of the metal ion; however, marked variation of the stability constant (K_1) for metal ion–BzH complex formation in solution was observed. Thus the enzyme appears to modify the properties of the bound metal ion so that the catalytic roles of the different metal ions are relatively invariant compared to their properties in solution ('Hephaestus effect'). The slight reduction in catalytic efficiency by Mn^{2+}–MR was studied by examining the dependence of k_{cat}^{app} and $(k_{cat}/K_m)^{app}$ for Mn^{2+}–MR on the solvent microviscosity. These studies showed that the metal ion plays a role in the uniform binding of the transition states for substrate/product association/dissociation and the chemical step.

LIST OF ABBREVIATIONS USED

α–HBP	α–hydroxybenzylphosphonate
BSA	bovine serum albumin
BzP	benzoylphosphonate
BzH	benzohydroxamate
CD	circular dichroism
DCPIP	2,6–dichlorophenolindophenol
EDTA	ethylenediaminetetraacetic acid disodium salt dihydrate
EPR	electron paramagnetic resonance
GH38	GH38 class II α-mannosidase (EC 3.2.1.24)
GlxI	glyoxalase I (EC 4.4.1.5)
HEPES	4–(2–hydroxyethyl)piperazine–1–ethanesulfonic acid
IPTG	isopropyl β–D–thiogalactopyranoside
ITC	isothermal titration calorimetry
LB	Luria–Bertani
LFSE	ligand field stabilization energy
LFT	ligand field theory
MeOH	methanol
MR	mandelate racemase (EC 5.1.2.2)
MW	molecular weight
NMR	nuclear magnetic resonance
OD	optical density
PDB	Protein Data Bank
RMS	root mean square
TFHTP	3,3,3–trifluoro–2–hydroxy–2–(trifluoromethyl)–propanoate
TFLA	trifluorolactic acid
TRIS	2-amino-2-hydroxymethyl-propane-1,3-diol
WTMR	wild–type mandelate racemase

ACKNOWLEDGEMENTS

First and foremost, I would like to acknowledge anyone who has ever worked on mandelate racemase. I would especially like to thank two researchers, my predecessor Mitesh Nagar, and my spiritual predecessor, Martin St. Maurice, for paving the way in the Bearne Lab. There's a feeling you get, when writing about mandelate racemase, that you're standing on the shoulders of giants. At the end of this thesis you will find a brief list of some of the finest scientists of our time. Much of my work exists because of their work.

I owe an eternal debt of gratitude (one which I can never repay) to my wife Ashley. No one has supported my choices and decisions in life as completely and selflessly as she has. Her devotion to mine and our daughter Aria's health and well–being is the greatest form of love there is.

I would also like to thank my parents Dale and Elaine. Everything I've done in my life, for better or worse, is a reflection of the values and morals they've instilled in me. My accomplishments are their accomplishments.

I'd like to thank my supervisory committee members for their confidence in my abilities and their encouragement throughout the course of my work. If I could choose another lab to work in it would be Dr. Jan Rainey's. And, if I could have travelled back in time twenty years and chosen a lab to work in it, would have been Dr Carmichael Wallace's.

I would like to thank the Nova Scotia Health Research Foundation for choosing me as the recipient of a Master's Award scholarship. Every little bit helps.

Last but not least I am compelled to thank my supervisor Dr. Stephen Bearne. To say that Dr. Bearne was a mentor to me would be grossly incorrect. Instead I would say this; a person who challenges you to become the best researcher you can be, forcing you to strive for nothing short of excellence, and, who constantly confronts and challenges your ideas and principles, is something much nobler and greater than a mentor, they are a teacher. Dr. Bearne is a true teacher in every sense of the word. From him, I have received two of the greatest things any man can be given, an opportunity and an education; for that, I thank you.

My parting contribution to this thesis is a quote from a brilliant philosopher, which I feel summarizes my brief moment in academia;

‘Some people have no idea what they're doing, and a lot of them are really good at it.’

– George Carlin

Chapter 1
Introduction

1.1 A Brief History of Mandelate Racemase

1.1.1 Early Characterization of Mandelate Racemase

Mandalate racemase (MR, EC 5.1.2.2) from *Pseudomonas putida* catalyzes the interconversion of the enantiomers of mandelic acid via a two–base mechanism (**Scheme 1.1**). The enzyme was first identified in 1950 when Stanier and co–workers discovered that *P. putida* could grow on media containing either enantiomer of mandelic acid as a sole source of carbon (Stanier, 1950). As a result of further work by Gansulalus *et al*. (1953), a complex system of enzymes consisting of two main groups were characterized; D-mandelate is converted into benzoic acid by 'the mandelate group' (**Figure 1.1**), and 'the β-ketoadipate group' (**Figure 1.1**), further breaks down benzoic acid into succinic acid and acetyl–CoA for use in the citric acid cycle (Gansalus *et al*., 1953a; Gunsalus *et al*., 1953b; Stanier *et al*., 1953). Initial research studied the regulation of the inducible enzymes of the mandelate group in *P. putida*, rather than the mechanisms of the enzymes involved.

Early studies by Weil-Malherbe (1966) determined that MR was activated by Mg^{2+}, Mn^{2+}, Co^{2+}, and, to a lesser extent, Ni^{2+} (Weil-Malherbe, 1966). Fee *et al*. (1974) later confirmed that these divalent metal cations were essential for catalysis. Weil-Malherbe also determined the optimum pH (~7.8) for catalysis and conducted measurements of MR activity using a coupled assay with L–mandelate dehydrogenase and benzoylformic dehydrogenase in which the production of benzaldehyde was observed at 250 nm (Weil-Malherbe, 1966). Hegemon *et al*. (1970a) later replaced this

Scheme 1.1 Mechanism for the reaction catalyzed by mandelate racemase

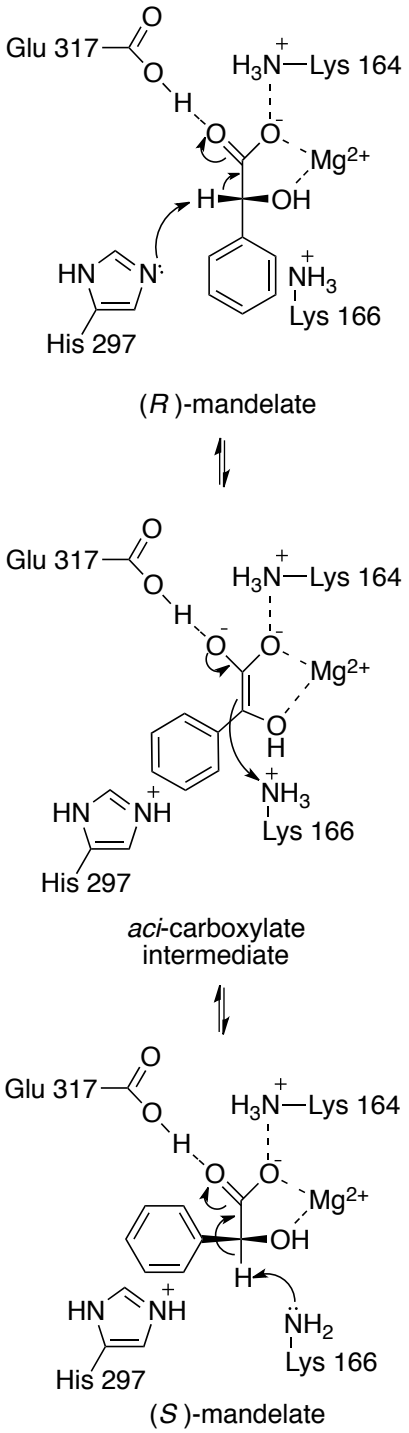

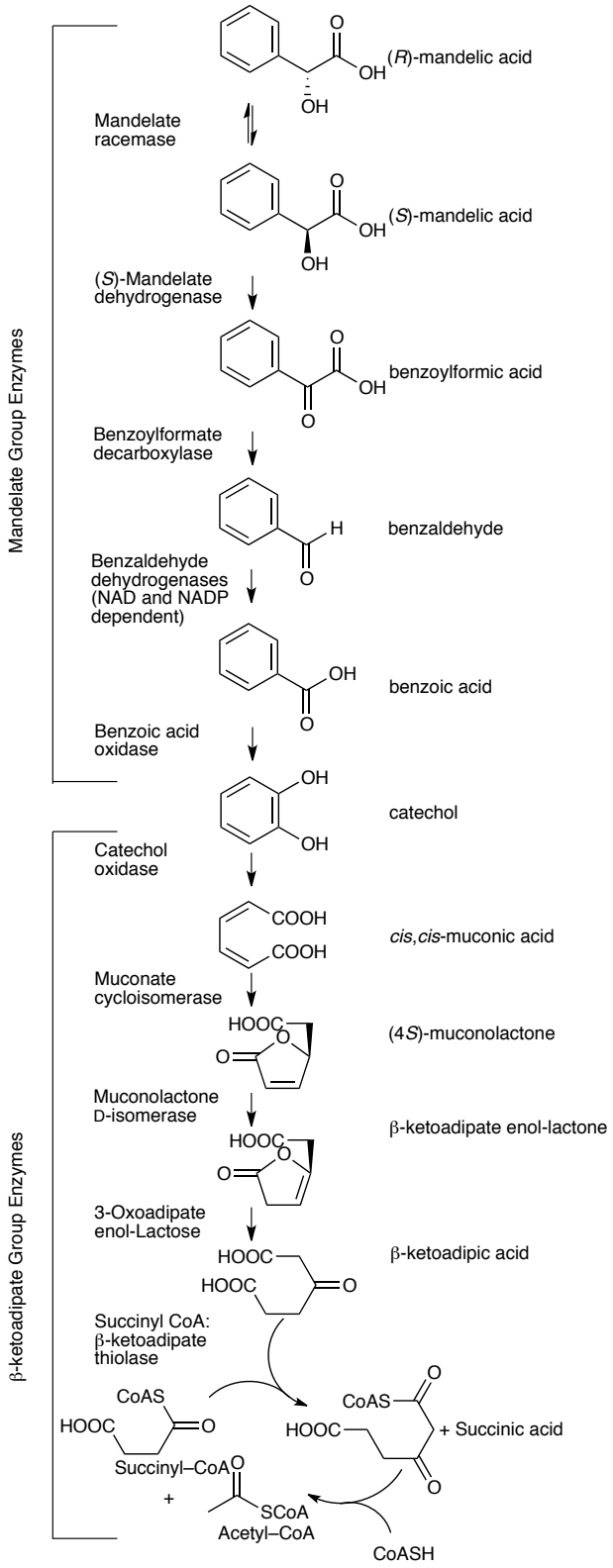

Figure 1.1 Metabolic pathway for the catabolism of (*R*)- and (*S*)-mandelic acid by *Pseudomonas putida* (Hegeman *et al*., 1970)

assay with a more accurate coupled assay in which the chromophore 2,6-dichlorophenolindophenol (DCPIP, λ_{max} = 600 nm) is bleached during the oxidation of L-mandelate to produce benzoylformic acid by L-mandelate–specific dehydrogenase (**Scheme 1.2**). This assay suffered from several major drawbacks, such as a high pH requirement for observation of DCPIP, highly turbid assay mixtures causing light scattering, and an inability to observe the reaction when L-mandelate is the substrate (Hegemon *et al*., 1970a).

Sharp *et al*. (1978) developed a direct kinetic assay, employing circular dichroism, allowing more precise kinetic measurement of MR activity. Since this is the principal assay utilized in this thesis, it will be discussed in greater detail in Chapter 2. More recently, Bearne *et al*. (1999) developed a fixed-time assay for the quantification of MR activity. The assay consists of the separation and quantification of substrate (either *(S)*– or *(R)*–mandelate) and product using isocratic reversed-phase high-performance liquid chromatography on a Sumichiral OA-6100 column, and following the absorbance at 254 nm (Bearne *et al*., 1999). This method allows for observation of initial rates at substrate concentrations well below K_m values. Some drawbacks to this assay are that it is time consuming, and sometimes incompatible with inhibitors that have a similar retention time to either the product or substrate (Bearne *et al*., 1999).

Early characterization of MR quaternary structure by Fee *et al*. (1974) showed that it was a tetramer with each subunit having a molecular mass of 69 500 Da for a total molecular mass of 278 000 Da. They also determined that the primary structure was comprised of 325 amino acids (Fee *et al*., 1974). These early determinations were not entirely accurate, and it wasn't until Ransom *et al*. (1988) isolated and purified a

Scheme 1.2 Mechanism of coupled assay involving DCPIP and L–mandelate dehydrogenase

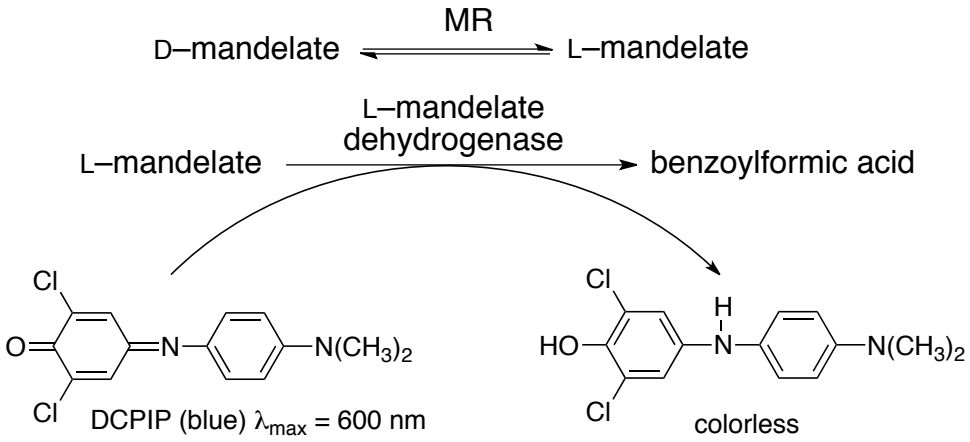

homogenous sample of MR from *P. putida* that MR was revealed to be an octamer. Sequencing of the gene encoding MR also predicted a primary sequence of 359 amino acids and a molecular mass of 38 570 Da per subunit (Ransom *et al.,* 1988).

1.1.2 Key Structural Features of MR

The first crystal structure of MR was reported by Neidhart *et al*. in 1988, and subsequently solved three years later at a resolution of 2.5–Å (Neidhart *et al.,* 1991). The quaternary structure of MR is an octamer of identical subunits, each containing an independent active site (Neidhart *et al.,* 1991). Each active site contains residues from a neighbouring subunit; these tightly associated subunits are why MR is described as a 'tetramer of dimers' (Neidhart *et al.,* 1991). Each monomer comprises three distinct structural domains. Residues 5–126 are referred to as the N-terminal domain, which consists of an antiparallel four–α–helix bundle and a three-stranded antiparallel β–sheet. Residues 331-359 make-up the C–terminal domain, and residues 134–319 comprise the prominent α/β–barrel domain, composed of 8 central strands of β–sheet and 7 α–helices (Neidhart *et al.,* 1991).

The active site (**Figure 1.2**) of MR is located at the C-terminal ends of the β–strands of the α/β–barrel domain. Three residues, Asp 195, Glu 221, and Glu 247, residing at the end of β–strands 3, 4, and 5, respectively, coordinate the active site metal ion (Neidhart *et al.,* 1991). At the end of β–strands 2 and 7 are the basic residues Lys 166 and His 297. Their position adjacent to the chiral centre of the substrate analogue (*S)*–atrolactate led to the early identification of these residues as the catalytic amino acids responsible for removal and addition of the proton during the chemical step of catalysis

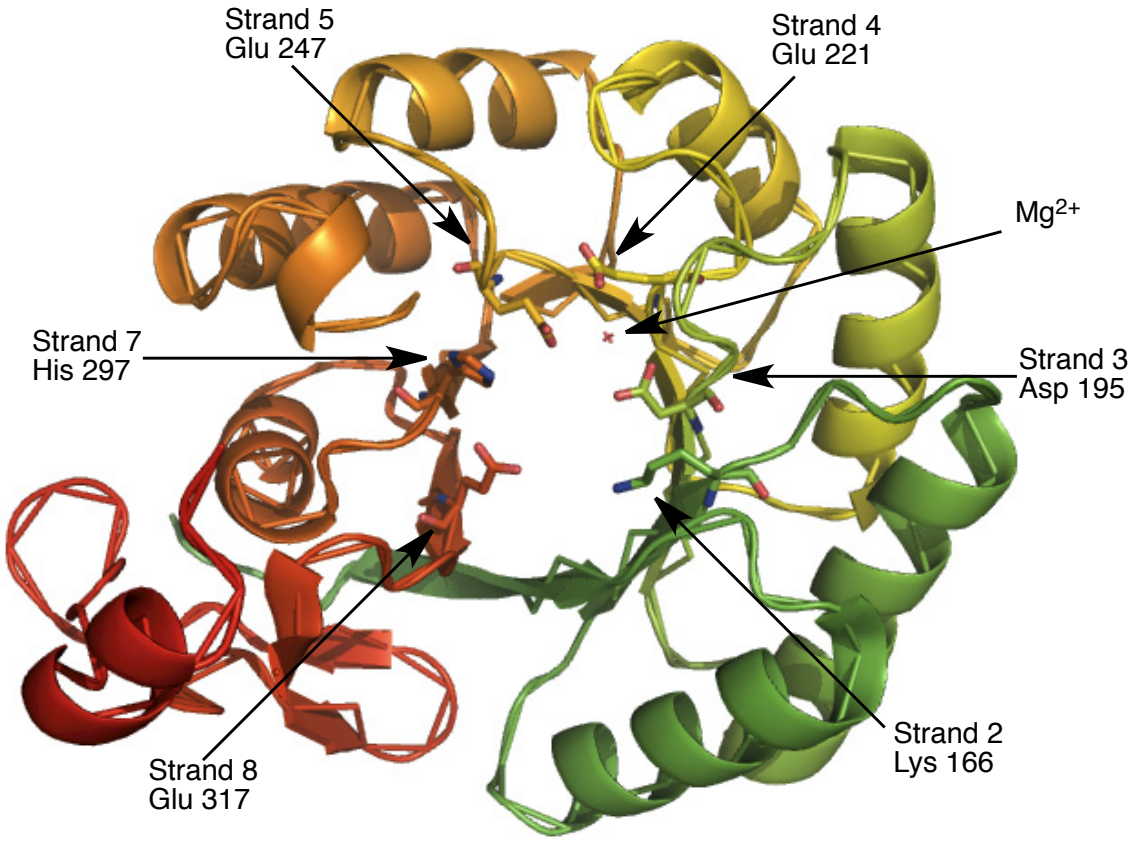

Figure 1.2 Structure of MR showing strands of the α/β-barrel domain, with metal ion co–ordinating ligands (Asp 195, Glu 221 and Glu 247), and Brønsted basic/acidic catalysts (Lys 166 and His 297) and general acid catalyst (Glu 317) in the active site. Created using MacPyMol from PDB structure 1MDR (Neidhart *et al*., 1991).

(**Scheme 1.1**) (Neidhart *et al.,* 1991). Additional crystal structures of wild–type MR and site–directed mutagenesis followed by structural and kinetic studies, confirmed that these were indeed the two Brønsted acid-base catalysts (Landro *et al.,* 1991; Landro *et al.,* 1994; Kallarakal *et al.,* 1995). The active site also contains Glu 317, which is located at the C–terminal end of β–strand 8. This residue participates in catalysis by acting as a general acid catalyst to stabilize the enolate intermediate (**Scheme 1.1**) (Mitra *et al.,* 1995).

At the opening of the MR active site lies a large cavity composed of hydrophobic amino acid residues from both the N-terminal and central α/β–barrel domains, as well as Leu 93 from the adjacent subunit (Neidhart *et al.*, 1991). Probing this hydrophobic 'pocket' with a number of substrate analogues (glycolates) and intermediate analogues (hydroxamates), as well as the alternative substrate 2–naphthylglycolate, demonstrated that steric restrictions placed on the binding of the substrate are minimal but increased steric bulk impairs stabilization of the transition state/intermediate (St. Maurice and Bearne, 2004). Further studies, involving site–directed mutagenesis of hydrophobic pocket residues, support the proposal that, during racemization, the phenyl group of the substrate moves between an *R*-pocket comprised of residues from the 50s loop, predominantly Phe 52 and Tyr 54, and an *S*–pocket, comprised of residues from the 20s loop (Siddiqi *et al.,* 2005). The 20s loop (primarily the hydrophobic residues Val 22, Thr 24, Ala 25, Val 26, and, Val 29) constitutes a flap covering the active site cavity, shielding the active site from solvent, and playing a role in determining substrate specificity (Bourque and Bearne, 2008; Siddiqi *et al.,* 2005).

1.1.3 Mechanism of the Reaction Catalyzed by MR

MR catalyzes the Mg^{2+}–dependent 1,1–proton transfer reaction that interconverts the enantiomers of mandelic acid (**Scheme 1.1**). In addition to utilizing mandelate as a substrate, the enzyme will also interconvert a number of aromatic-substituted α–hydroxy acids (Hegeman *et al*., 1970; Felfer *et al*., 2001), the non-aromatic substrates vinylglycolate and 2-hydroxybut–3–enoate (Kenyon *et al*., 1995), a number of non–natural α–hydroxycarboxylic acids (Felfer *et al*., 2005) and, most recently discovered, trifluorolactic acid (Nagar *et al*., 2011). The reaction proceeds via a two–base mechanism in which Lys 166 abstracts the α–proton from (*S*)–mandelate and His 297 abstracts the α–proton from (*R*)–mandelate (Gerlt *et al*., 1995; Landro *et al*., 1994; Neidhart *et al*., 1991). This is a stepwise mechanism (Landro *et al*. 1991; Powers *et al*. 1991), and it has long been proposed that the intermediate of this reaction is a resonance–stabilized carbanion intermediate (Hegeman *et al*., 1970; Kenyon and Hegeman, 1970). Despite overwhelming kinetic evidence, this proposal was often met with criticism, due to the high–energy carbanion intermediate having an exceptionally short lifetime and being too unstable to account for the observed rate of the reaction catalyzed by MR (Thibbin and Jencks, 1979).

Recent studies have suggested that MR stabilizes an enolate intermediate (Mitra *et al*., 1995; Neidhart *et al*. 1991; St. Maurice and Bearne, 2000). During catalysis, Glu 317 acts as a Brønsted acid, donating a proton to the substrate's carboxylic acid and stabilizing the transient enolate intermediate (**Figure 1.3**) (Landro *et al*., 1994, Mitra *et al*., 1995). Catalysis is also assisted by an electrostatic interaction between Lys 164 (**Figure 1.3**) and the carboxylate group of mandelate, which lowers the p*K*a of the α–

Figure 1.3 Stabilization of the putative enolate intermediate by key residues in the active site of MR.

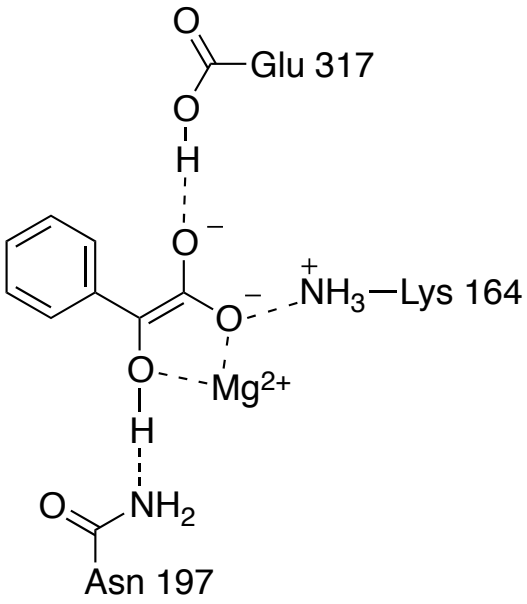

proton by nearly 7 units (Neidhart *et al*., 1991; Gerlt and Gassman, 1993). By estimating the effective molarity of Glu 317, His 297, and Lys 166 to be, $\geq 3\times10^5$, $\geq 3\times10^3$, and $\geq$ 622 M respectively, Bearne and Wolfenden (1997) lent credibility to the hypothesis that general acid-base catalysis becomes an efficient mode of catalysis when structural complementarity between MR and its substrate is optimized in the transition state.

Recent studies have also shown the importance of Asn 197 during the reaction catalyzed by MR (St. Maurice *et al*. 2000). Recognizing that Asn 197 is within hydrogen bonding distance of the hydroxyl group of bound substrate analogue (*S*)-atrolactate (Landro *et al*., 1994), the Bearne research group engineered the N197A mutant and measured the competitive inhibition constants of several intermediate analogues (**Figure 1.4**) (St. Maurice *et al*. 2000). The result of this study was the proposal that hydrogen bonding between Asn 197 and the hydroxyl group of the bound substrate (**Figure 1.3**) could provide approximately 3.5 kcal/mol of free energy to differentially stabilize the transition state relative to the ground state (St. Maurice *et al*., 2000). It is also commonly proposed that Mg^{2+} plays an important role in catalysis by neutralizing the increased negative charge of the enolate transition state (Guthrie and Kluger, 1993). The role of the essential metal–ion in MR catalysis is the main investigation of this thesis and will be discussed in greater detail in subsequent chapters.

1.1.4 Kinetics and Thermodynamics of MR Catalysis

A possible kinetic mechanism for a reversible, unireactant enzyme-catalyzed reaction, such as the one catalyzed by MR, is shown in **Scheme 1.3**. Using this mechanism, the steady-state approximation, and assuming initial velocity conditions, the

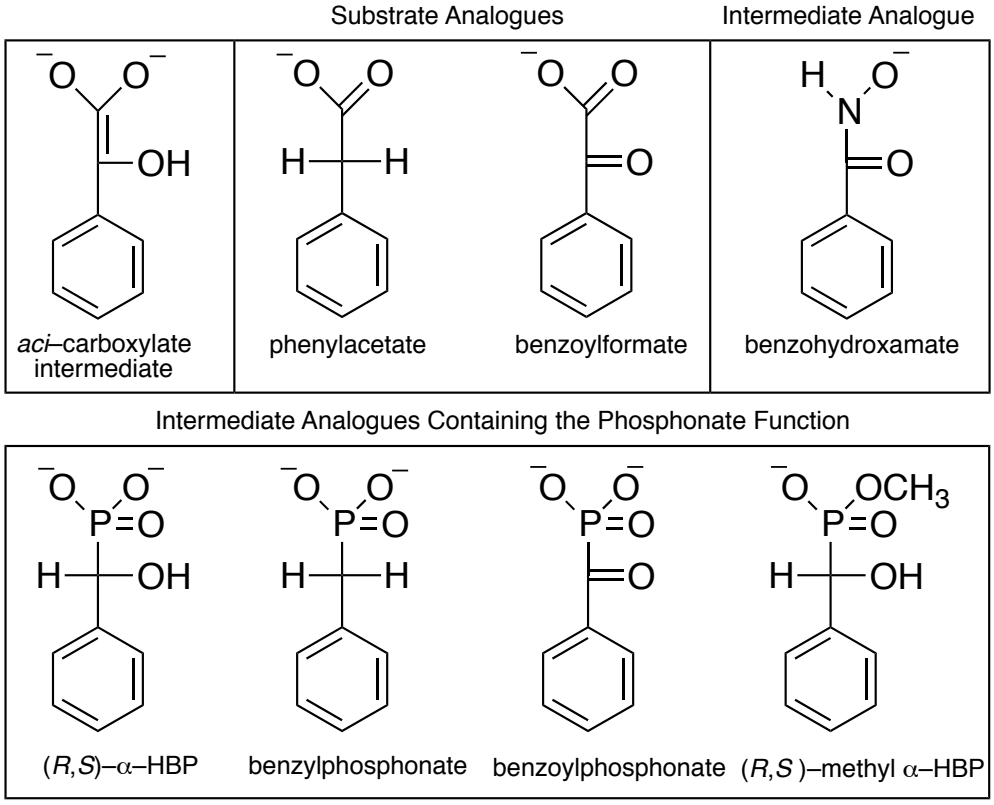

Figure 1.4 Structures of a number of substrate and intermediate analogues of the *aci*-carboxylate intermediate formed during MR catalysis (St. Maurice and Bearne 2000).

Scheme 1.3 A possible kinetic mechanism for the reaction catalyzed by MR (Note: This mechanism does not include an enzyme–bound intermediate.)

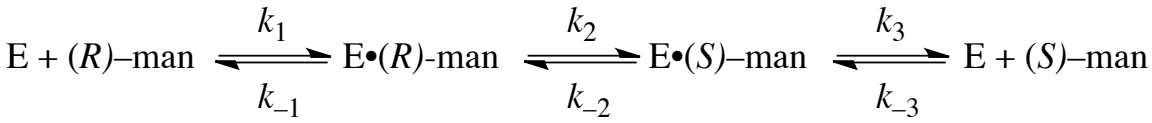

apparent kinetic parameters k_{cat}, K_m and k_{cat}/K_m for the reaction catalyzed by MR can be derived in both the $R \rightarrow S$ (eqns 1.1–3) and $S \rightarrow R$ (eqns 1.4–6) reaction directions.

$$k_{cat}^{R \rightarrow S} = \frac{k_2 k_3}{k_{-2} + k_2 + k_3} \quad 1.1$$

$$K_m^{(R)-man} = \frac{k_{-1}k_2 + k_{-1}k_3 + k_2 k_3}{k_1(k_2 + k_{-2} + k_3)} \quad 1.2$$

$$\frac{k_{cat}^{R \rightarrow S}}{K_m^{(R)-man}} = \frac{k_1 k_2 k_3}{k_{-1}k_{-2} + k_{-1}k_3 + k_2 k_3} \quad 1.3$$

$$k_{cat}^{S \rightarrow R} = \frac{k_{-1}k_{-2}}{k_{-1} + k_{-2} + k_2} \quad 1.4$$

$$K_m^{(S)-man} = \frac{k_{-1}k_2 + k_{-1}k_3 + k_2 k_3}{k_{-3}(k_{-2} + k_2 + k_{-1})} \quad 1.5$$

$$\frac{k_{cat}^{S \rightarrow R}}{K_m^{(S)-man}} = \frac{k_{-1}k_{-2}k_{-3}}{k_{-1}k_{-2} + k_{-1}k_3 + k_2 k_3} \quad 1.6$$

In 2002, St. Maurice and Bearne conducted an in depth study of the viscosity dependence of the reaction catalyzed by MR in order to estimate the rate constants for all steps along the reaction pathway. The apparent turnover rate (k_{cat}) and the catalytic efficiency (k_{cat}/K_m) of MR were observed to be partially dependent on solvent microviscosity, indicating that external steps such as enzyme-substrate association (k_1 or k_{-3}) and enzyme-product dissociation (k_3 or k_{-1}) were not significantly faster than the internal chemical step (k_2, k_{-2}) and, therefore, partially rate–limiting (St. Maurice and Bearne, 2002). Furthermore, by using the alternatative substrate (*S*)–*p*–nitromandelate and (*R*,*S*)–mandelate as a competitive inhibitor, St. Maurice and Bearne showed that the Michaelis constant (K_m) is approximately equal to the dissociation constant (K_s) for either

reaction direction, consistent with prior studies using an NMR titration experiment (Fee *et al.,* 1974) and by protection experiments using the irreversible inactivator (*R*,*S*)-phenylglycidate (Maggio *et al.,* 1975).

The enolase superfamily of enzymes catalyze the abstraction of α–protons from carboxylic acid substrates to yield enolate intermediates (Babbitt *et al.,* 1996). As a member of this family, MR has often been studied as a paradigm for understanding how enzymes catalyze the deprotonation of a carbon acid with a relatively high pK_a value. MR is very proficient at discriminating between the substrate in the ground state and the altered substrate in the transition state, producing a rate enhancement exceeding 15 orders of magnitude and reducing the activation barrier of the reaction by 26 kcal/mol (Bearne and Wolfenden, 1997). The virtual dissociation constant of the enzyme-substrate complex in the transition state (K_{tx}) is defined as the reciprocal of the proficiency of an enzyme as shown in eqn 1.7 (rearrangement of eqn. 1.13 from section 1.3.2) (Radzicka and Wolfenden, 1995).

$$K_{tx} = k_{non}/(k_{cat}/K_s) \qquad 1.7$$

By determining the dependence of the catalytic efficiency (k_{cat}/K_s) and the non-enzymatic rate constant (k_{non}) on temperature, the temperature dependence of K_{tx} was estimated and used to calculate the enthalpic and entropic contributions to the free energy of transition state stabilization (St. Maurice and Bearne, 2002; Bearne and Wolfenden, 1997). Substrate binding accompanies a loss of entropy (–4.8 kcal/mol at 25 ˚C) and a release of enthalpy (–8.9 kcal/mol), consistent with formation of non-covalent interactions between the free enzyme and substrate (**Figure 1.5**) (St. Maurice and Bearne, 2002). The chemical step has a large enthalpy of activation (+15.4 kcal/mol) and a

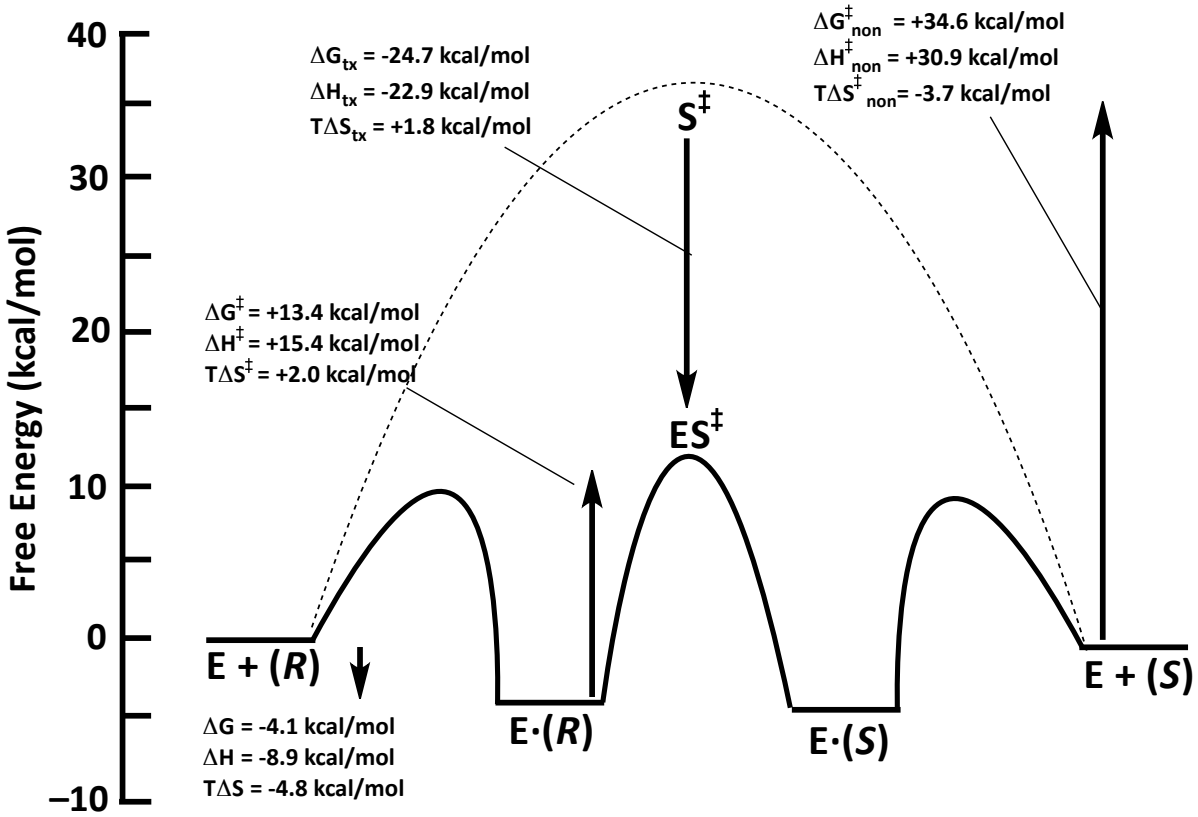

Figure 1.5 Free energy profile (pH 7.5, 25 ˚C) for MR catalyzed (solid line) and uncatalyzed (dashed line) racemization of (*R*)– and (*S*)–mandelate. Free energies are drawn to scale and determined from rate constants for both enzymatic (St. Maurice and Bearne, 2002) and non-enzymatic (Bearne and Wolfenden, 1997) reactions, including the calculated change in enthalpy ($\Delta H^{\ddagger}$) and entropy ($T\Delta S^{\ddagger}$).

favourable gain in entropy (+2 kcal/mol at 25 ˚C) compared to the non-ezymatic reaction ($\Delta H^{\ddagger}$ = + 30.9 kcal/mol, $T\Delta S^{\ddagger}$ = –3.7 kcal/mol at 25 ˚C (Bearne and Wolfenden, 1997)), indicating that the proficiency of MR arises predominantly from an enthalpic reduction, as well as, a slightly favourable entropic contribution (St. Maurice and Bearne, 2002). A free energy profile summarizing of these findings is presented in **Figure 1.5**.

1.1.5 Pseudosymmetry in MR Catalysis

Racemases catalyze racemization reactions in an asymmetric environment. The overall equilibrium constant (K_{eq}) is equal to unity and, according to the Haldane relationship, the experimentally derived k_{cat}/K_m in the forward direction must equal the k_{cat}/K_m in the reverse direction (Briggs and Haldane, 1925; Segel, 1993). MR displays a kinetic symmetry, where the values for the individual kinetic constants k_{cat} and K_m have been reported to be virtually identical in both directions (Whitman *et al.,* 1985; Maggio *et al.*, 1975), giving rise to approximately equal k_{cat}/K_m values in both reaction directions. The fact that k_{cat} and K_m values are approximately equal for both reaction directions arises fortuitously, considering the asymmetric environment of the active site.

1.2 Magnesium in Biochemistry

Since MR is regarded as a metalloenzyme, requiring Mg^{2+} as an essential cofactor, this section will discuss some general aspects of Mg^{2+} in biological systems.

1.2.1 Chemical Properties of Magnesium in Biological Systems

Magnesium is the eighth most abundant element on earth and the fourth most abundant element in prokaryotes, with intracellular cytosolic concentrations of approximately 0.5 mM (Frausto da Silva and Williams, 1991). Furthermore, an estimated 16% of all known enzymes require magnesium as an essential cofactor (Waldron *et al.*,

2009). The chemical properties of magnesium make it unique among biological cations and significantly different from the other alkali and alkaline earth metals. Mg^{2+} has the smallest ionic radius of all cations (0.65 Å) but the largest hydration radius (4.76 Å), corresponding to an astounding volume difference of ~ 400 $Å^3$ between the hydrated and dehydrated forms (**Table 1.1**) (Diebler *et al*.; 1969; Eigen, 1963). By comparison, K^+ has an ionic radius of 1.38 Å and a hydration radius of only 2.32 Å, giving a volume difference of ~ 40 $Å^3$, and Ca^+ (ionic radius 0.99 Å, hydration radius 2.95 Å) has a volume difference of ~ 100 $Å^3$ (Diebler *et al*., 1969; Eigen, 1963). Due to the slow water exchange rate of Mg^{2+} (10^5 s^{-1}), the hydrated cation is the most common form found in solution, which means proteins and ligands must interact directly with the large, hydrated ion prior to dehydration and binding of the small free cation (Diebler *et al*., 1969).

Mg^{2+} is invariably hexacoordinate, with an octahedral coordination sphere containing six ligands, usually water (**Figure 1.6**). The typical Mg^{2+} coordinate bond length is between 2.05 and 2.25 Å, with little deviation in the standard 90° bond angle (**Figure 1.6**) (Maguire and Cowan, 2002). Crystal structures show that when directly bound to a protein, three or fewer of the Mg^{2+} coordination sites are occupied by the oxygen atom of acidic residues, with the other sites occupied by water or other ligands (Black *et al*. 1994; Cowan 1997). Comparatively, Ca^{2+} can coordinate 6, 7, or even 8 ligands, and when bound to a protein, all sites can be occupied by a number of different sidechains of the amino acid residues (Einsphar and Bugg, 1984). The amount of variance in bond length (2.2-2.7 Å) and bond angle (up to 40 °) is much greater in Ca^{2+} as well (Einsphar and Bugg, 1984). These properties, coupled with its small ionic radius,

Table 1.1 Comparing the hydrated and dehydrated ionic radii for common biological cations.

Ion	Ionic radius (Å)[a]	Hydrated radius (Å)[a]	Ionic volume ($Å^3$)	Hydrated Volume ($Å^3$)	Ratio of volumes
Na^+	0.95	2.75	3.6	88.3	24.5
K^+	1.38	2.32	11	52.5	4.8
Ca^{2+}	0.99	2.95	4.1	108	26.3
Mg^{2+}	0.65	4.76	1.2	453	394

[a]Ionic and hydrated radii from ref (Diebler *et al*., 1969; Eigen, 1963)

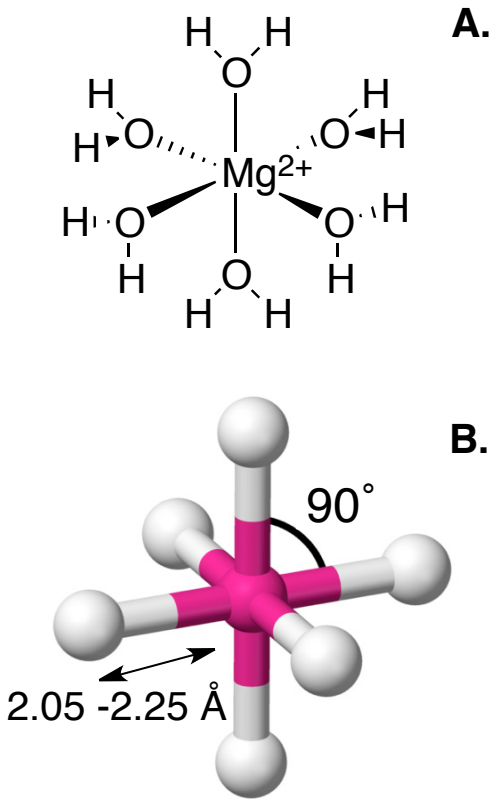

Figure 1.6 Mg^{2+} hexacoordinated to six water molecules in an octahedral geometry (A). The calculated average bond angles and lengths for octahedrally coordinated Mg^{2+} (B), for all known ligands as compiled by Maguire and Cowan (2002).

high charge density, and redox inertness make Mg^{2+} a chemically unique biological cation.

1.2.2 Common Roles of the Magnesium Ion as a Cofactor in Enzymatic Catalysis

There are two general mechanisms by which an enzyme will utilize Mg^{2+} as a cofactor: either Mg^{2+} will bind to the substrate altering its electrostatic or geometric properties to allow for recognition by the enzyme, or the enzyme will bind Mg^{2+}, causing the enzyme to undergo a conformational change to allow for recognition of the substrate. As an example of the former type, consider isocitrate lyase, which catalyzes the reversible cleavage of isocitrate to form glyoxylate and succinate (**Scheme 1.4**) (Britton *et al.,* 2000). In solution, isocitrate will complex free Mg^{2} via coordination to a carboxylate and hydroxyl group, prior to binding to the enzyme (**Scheme 1.4**). The enzyme has a very low affinity for either of the free components with a K_d of ~ 6 mM for Mg^{2+} and undetectable binding for the free isocitrate (Britton *et al.,* 2000). In this case, the Mg^{2+}–isocitrate complex is the true substrate for the reaction with a high affinity (K_m ~ 40 μM) for the active site of isocitrate lyase (Britton *et al.,* 2000).

MR is an example of the second type of mechanism, where Mg^{2+} has little or no affinity for the substrate (either (*R*)- or (*S*)-mandelate) in solution, but binds to the apo-enzyme prior to formation of the enzyme-substrate complex (Fee *et al.,* 1974). In the case of this type of enzyme, the metal ion can alter the conformation of the enzyme's active site, play a direct role in catalysis, or, perhaps, do both. Because of its high charge density, Mg^{2+} is an excellent Lewis acid and enzyme–bound Mg^{2+} will bind a substrate to either make it more reactive or to orient it correctly for catalysis. A classic example of

Scheme 1.4 Proposed mechanism for isocitrate lyase (Britton *et al*., 2000).

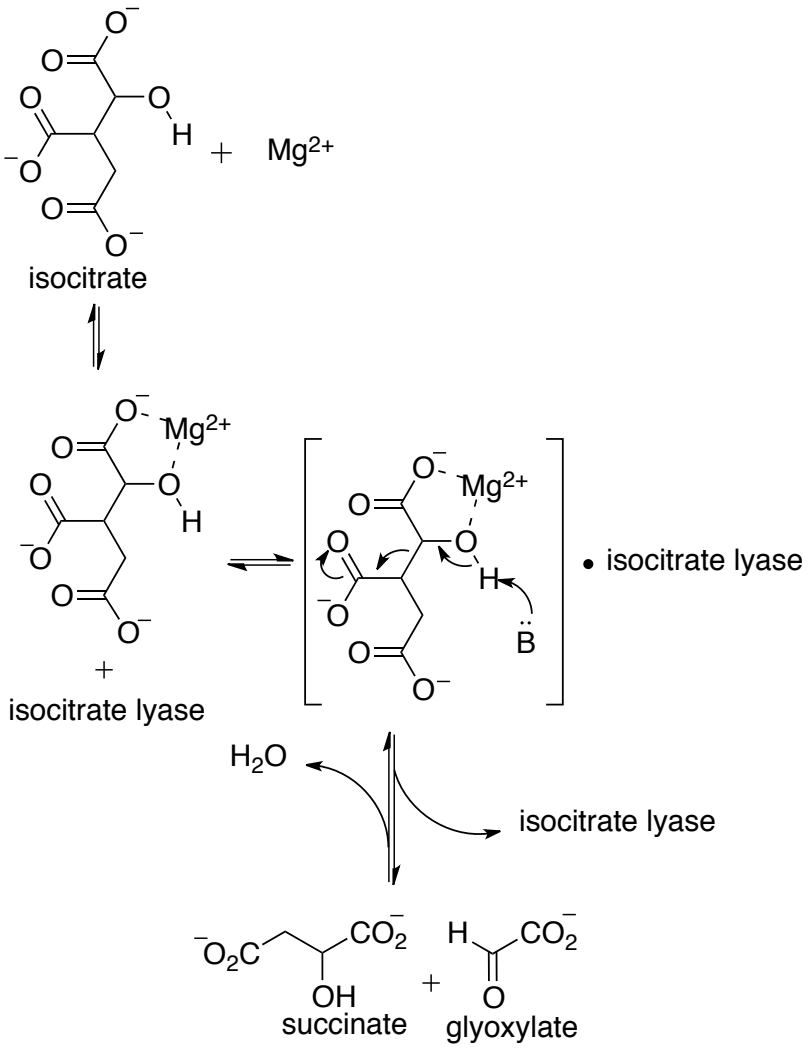

this type of Mg^{2+}–dependent catalysis has been proposed in nuclease enzymes, such as *Eco*RI and *Eco*RV (Cowan, 1998). These enzymes require Mg^{2+} as an essential cofactor in order to orient the nucleotide correctly and to promote nucleophilic attack on the substrate by withdrawing electron density from the phosphate group. It can also stabilize a high–energy intermediate through electrostatic interactions, as it has often been proposed to do during the reaction catalyzed by MR (**Figure 1.7**) (Neidhart *et al.,* 1991).

1.2.3 Outer-sphere Versus Inner-sphere Coordination

When complexed with a substrate at an active site, Mg^{2+} could interact with a ligand through inner-sphere or outer-sphere coordination. Outer-sphere coordination is often encountered in metal-mediated phosphate ester hydrolysis reactions, such as those catalyzed by nucleases. Complexation to a fully hydrated magnesium ion has been shown to stabilize the increased negative charge of a transition state through both hydrogen bonding and electrostatic contributions (**Figure 1.8**) (Black *et al*., 1996; Black *et al*., 1997). Inner-sphere coordination, on the other hand, requires displacement of one or more of the six coordinated water molecules and direct chelation of the new ligand to the Mg^{2+} ion. Even though water-ligand exchange rates for Mg^{2+} in aqueous solutions are both slow and thermodynamically unfavourable, these exchange reactions will occur in environments with low dielectric constants ($\varepsilon \leq 4$), such as the interior of a protein (Dudev *et al.,* 1999). In fact, hexahydrated magnesium dications are predicted to have overwhelmingly high affinities for anionic acidic residues in active sites with low dieletric constants; but only three acidic residues at any one time can replace water molecules in the first coordination shell (Dudev *et al.,* 1999). The displacement of a fourth water molecule by an acidic protein residue has not been observed in nature and is

Figure 1.7 Predicted model of Mg^{2+}–bound MR stabilizing the putative enolate intermediate.

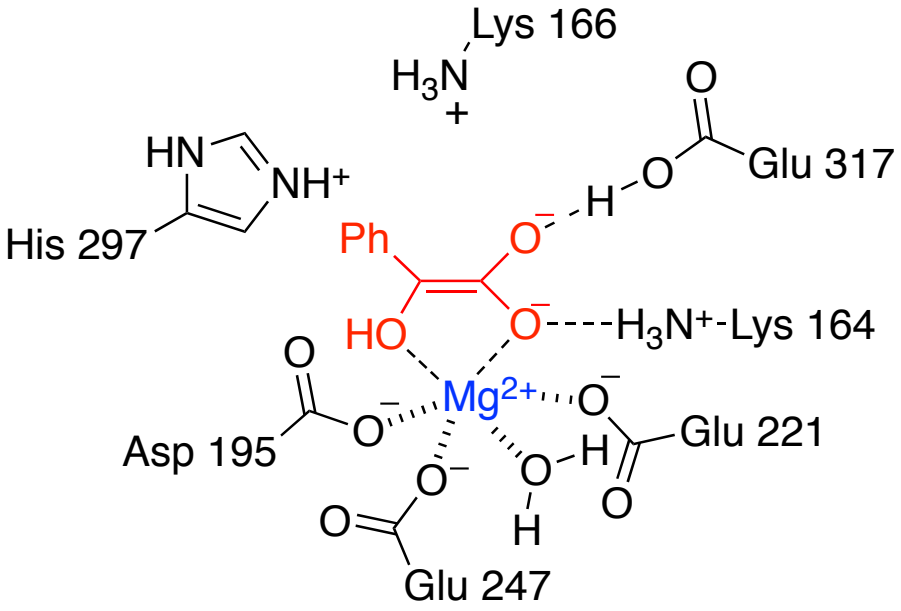

Figure 1.8 Proposed model for outer–sphere coordination to Mg^{2+} to stabilize the transition state for phosphoester hydrolysis (Black *et al*., 1996; Black *et al*., 1997)

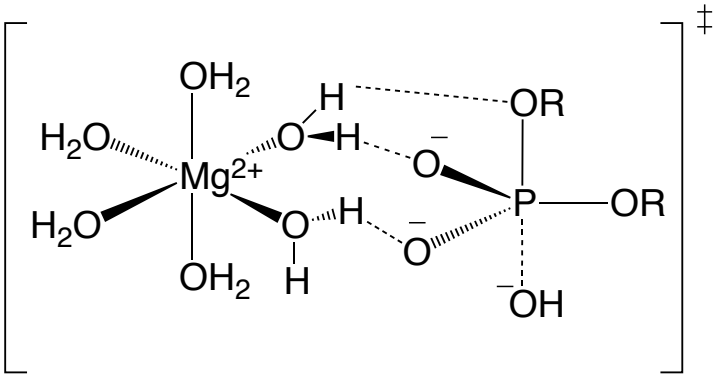

predicted to be thermodynamically unstable (Dudev *et al*., 1999). Very few studies have been done on Mg^{2+} outer-sphere coordination stabilization effects and even fewer studies have been conducted that observe the kinetics of inner-sphere coordination and its effects on enzymatic catalysis.

1.2.4 Magnesium in MR

Only a few studies have focused on the role of Mg^{2+} in the reaction catalyzed by MR. An earlier study (Weil-Malherbe, 1966) identified Mg^{2+} as an activator, but not an essential one, and stated that Mn^{2+}, Co^{2+}, and to a lesser extent Ni^{2+} could also activate MR (Weil-Malherbe, 1966). It wasn't until a study by Fee *et al*. (1974) that Mg^{2+} was identified as an essential activator and that the activity of the apo-enzyme was shown to be restored by Mn^{2+}, Co^{2+}, Ni^{2+}, and possibly Fe^{2+}. This study did not fully characterize the effects of the alternative metal cations on catalysis, or attempt to identify what role, if any, Mg^{2+} has in stabilization of the high energy intermediate (Fee *et al*., 1974).

Maggio *et al*. (1975) were the first to conduct extensive studies on Mn^{2+}–bound MR. By using racemic mandelate, isotopically labelled with ^{13}C at either the α-C or the carboxylate carbon, and conducting electron paramagnetic resonance (EPR) measurements with Mn^{2+}, they came to the conclusion that there was no direct coordination to Mn^{2+}, only outer–sphere coordination with both oxygens of the carboxylate functional group hydrogen bonded to a water molecule (**Figure 1.9**). The EPR study also revealed that at least one, and possibly two, water molecules were displaced from the active site by substrate binding and this may or may not have been related to ligand coordination to the metal ion cofactor (Magio *et al*., 1975). The first

Figure 1.9 Proposed outer–sphere coordination of Mn^{2+} in the active site of MR by (*R,S*)–mandelate (Maggio *et al*., 1975). The distances shown were estimated from EPR studies.

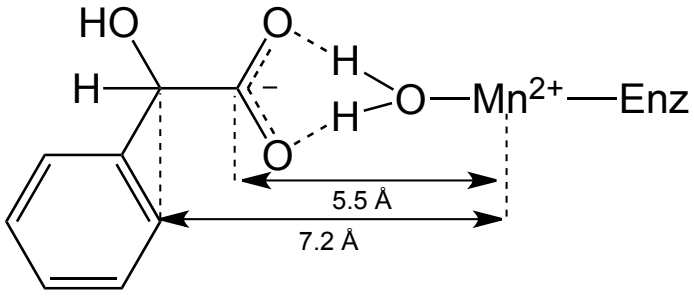

crystal structures solved by Neidhart *et al*. (1991), and every crystal structure since, discredit these early findings by showing that Mg^{2+} (and in one case Mn^{2+}) is bound in a hexacoordinated octahedral geometry to the active site residues Asp 195, Glu 221, and Glu 247, and that the other three sites were occupied by either water molecules, or one oxygen from a ligand carboxylate and another oxygen from the hydroxyl group of the same molecule (i.e., inner–sphere coordination).

An early crystal structure of MR that has been solved has Eu^{2+} coordinated to the active site with octahedral geometry (Neidhart, 1991). However, since Eu^{2+} is a known potent inhibitor of MR it is unlikely this is an active form of the enzyme (Powers, 1989).

1.3 Transition state theory in enzyme catalysis

Linus Pauling (1948) proposed that the rate enhancement provided by an enzyme arises from its ability to stabilize the transition state relative to the ground state, thereby lowering the activation energy. Wolfenden and coworkers (1972) further developed the hypothesis that the rate increase afforded by an enzyme is proportional to the affinity of the enzyme for the transition state structure relative to the ground state. This concept can be easily conveyed using a free energy diagram showing the reaction coordinates for a single substrate reaction in the presence and absence of an enzyme (**Figure 1.10**). In **Figure 1.10**, we can clearly see that the free energy of transition state stabilization provided by the enzyme (ΔG_{tx}) is equal to the free energy difference of the activation barriers for the uncatalyzed ($\Delta G^{\ddagger}_{non}$) and catalyzed ($\Delta G^{\ddagger}_{E}$) reactions.

Since the lifetime of the transition state complex is approximately 10^{-13} s, or roughly the length of time it takes for a single bond vibration, it is difficult to directly observe the structure of a transition state (Schramm 1998). We can, however,

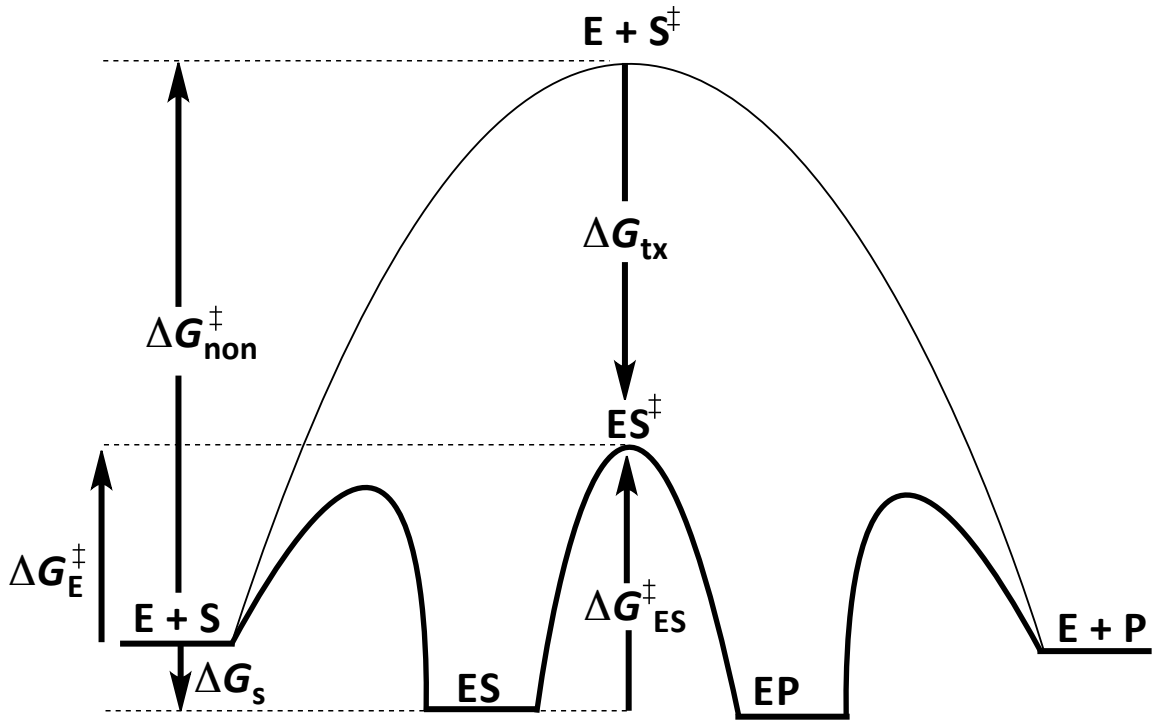

Figure 1.10 Relative free energy profiles for an uncatalyzed (thin line) and enzyme catalyzed (thick line) reaction for a hypothetical single substrate reaction. The free energy of transition state stabilization provided by the enzyme (ΔG_{tx}) is equal to the difference of free energy for the uncatalyzed ($\Delta G^{\ddagger}_{non}$) and catalyzed ($\Delta G_E^{\ddagger}$) reactions (where $\Delta G_E^{\ddagger} = \Delta G_{ES}^{\ddagger} - \Delta G_S$).

experimentally estimate the extent of transition state stabilization utilizing a thermodynamic cycle originally developed for acid catalysis by Kurz (1963) and applied to enzymatic catalysis by Wolfenden (1969) and Lienhard (1973) (**Scheme 1.5**). The thermodynamic cycle can be used to relate the equilibrium constants to give equation 1.12, which can be modified using transition state theory and equation 1.10, to give equation 1.13, where the ratio of the κν terms are essentially unity.

$$\frac{K_S}{K_{\mathrm{Tx}}} = \frac{K_{ES}^{\ddagger}}{K_S^{\ddagger}} \qquad 1.12$$

$$\frac{k_{\mathrm{cat}}}{k_{\mathrm{non}}} = \frac{\kappa\nu K_{\mathrm{ES}}^{\ddagger}}{\kappa\nu K_{\mathrm{S}}^{\ddagger}} \approx \frac{K^{\ddagger}_{\mathrm{ES}}}{K^{\ddagger}_{\mathrm{S}}} = \frac{K_S}{K_{\mathrm{Tx}}} \qquad 1.13$$

This allows us to estimate the virtual dissociation constant for the enzyme-substrate complex in the transition state (K_{Tx}), by using the experimentally measured nonenzymatic rate of catalysis (k_{non}) and the efficiency of the enzyme ($k_{\mathrm{cat}}/K_{\mathrm{S}}$).

1.4 Intermediate Analogues as Potent Inhibitors of MR

Designing a stable molecule that mimics the electrostatic and geometric properties of the transition state requires prior knowledge of its structure. In the case of MR, site–directed mutagenesis, X–ray crystallography, and extensive kinetic studies have all predicted that the reaction catalyzed by MR will proceed via a high-energy enolate intermediate (**Figure 1.3**) (Landro *et al*., 1994; Mitra *et al*., 1995; Neidhart *et al*., 1991). Several potent, reversible, competitive inhibitors of MR, shown in **Figure 1.11**, have been discovered which are thought to be analogues of the *aci*-carboxylate intermediate (Bourque *et al*., 2007; Burley and Bearne, 2005, St. Maurice and Bearne, 2000; St. Maurice *et al*., 2003).

Scheme 1.5 Thermodynamic cycle describing the enzyme–catalyzed and non–enzymatic conversion of substrate into product (Note: $K^{\ddagger}_{S}$ and $K^{\ddagger}_{ES}$ are association constants.)

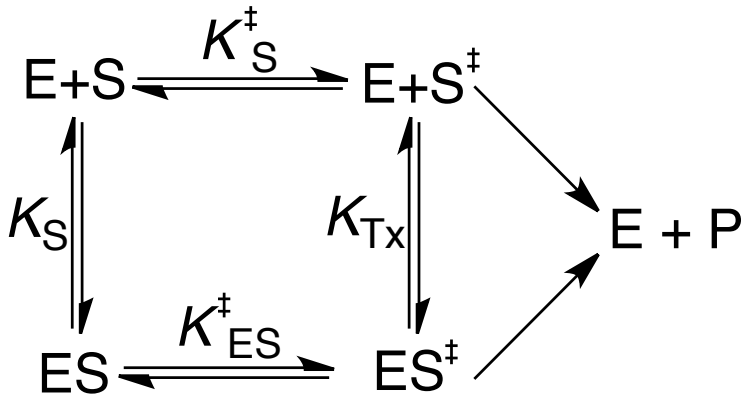

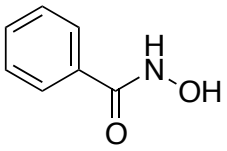

benzohydroxamic acid

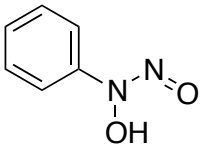

Cupferron

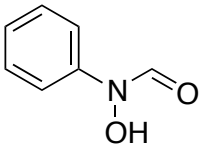

N–hydroxyformanilide

Figure 1.11 Analogues of the enolate intermediate of the reaction catalyzed by MR.

The retro-hydroxamate *N*-hydroxyformanilide (K_i = 2.79 ± 0.19 μM) (Bourque *et al*., 2007) has a similar binding affinity for the active site to Cupferron (K_i = 2.67 ± 0.09 μM) (Bourque *et al*., 2007) and benzohydroxamate (K_i = 11.7 ± 0.01 μM) (St. Maurice and Bearne, 2004). Crystal structures exist for wild–type MR bound to both Cupferron and benzohydroxamate and, while no crystal structure exists for MR bound *N*–hydroxyformanilide, it is reasonable to propose that it binds in a manner similar to Cupferron, due to their similarity in structure and binding affinity (Lietzan *et al*., 2012; Bourque *et al*., 2007).

These ligands can be considered good intermediate analogues for several reasons. First, they have a similar geometry to the *aci*–carboxylate intermediate (Bourque *et al*., 2007). Crystal structures of MR bound to both Cupferron and benzohydroxamate show that the phenyl ring is planar to both carboxylate oxygens and interacts significantly with both the hydrophobic (*R)*– and (*S*)–pockets (Lietzan *et al*., 2012). Second, both ligands chelate the Mg^{2+} ion with a shorter coordinate bond distance (0.1–0.2 Å) than the substrate analogue (*S*)–atrolactate, although the significance of this has never been investigated (Lietzan *et al*., 2012). Third, the crystal structure shows the α-carbon of both benzohydroxamate and Cupferron at equal distances between the catalytic residues Lys 166 and His 297 (Lietzan *et al*., 2012). Despite the electrostatics being unable to perfectly mimic the enolate intermediate (monoanionic analogues versus dianionic intermediate), geometrically speaking, the interaction between these ligands and the active site of MR is very similar to what might be expected for the *aci*–carboxylate intermediate (Lietzan *et al*., 2012)

It is also of note that the chiral compound α-hydroxybenzylphosphonate (α–HBP) (**Figure 1.4**) is a potent inhibitor and not a substrate of MR, despite its configuration resembling mandelic acid around the α-carbon (St. Maurice and Bearne, 2000). As well, the enantiomers of α-HBP have different binding affinities for the active site (K_i = 1.1 μM for 82% ee (*S*) and 34 μM for 76% ee (*R*)) with the absolute configurations of (*S*)– and (*R*)–α–HBP resembling (*R)*– and (*S*)–mandelate, respectively (St. Maurice and Bearne 2000)). This feature, coupled with the lack of crystal structures for any phosphonate-containing compound in the active site of MR, makes it difficult to include the enantiomers of α-HBP on the list of possible intermediate analogues. It may be that the strong binding affinity of α-HBP is due to a different binding orientation than has been observed for other ligands, and in no way resembles the binding orientation of either the substrate or intermediate.

1.5 The Entatic State Hypothesis

When first introduced by Vallee and Williams (1968), entatic state theory proposed that the efficiency of an enzyme relied, in part, on its ability to bind a cofactor and adopt a catalytically poised state in the absence of a substrate (Vallee and Williams, 1968). Since then, the theory has broadened to apply to any protein that adapts the geometric and/or electronic properties of an atom or group to perform a function (Williams, 1985). A primary application of entatic state theory is in the field of metalloenzymes. When a metalloenzyme binds a metal ion, the energy of the protein scaffold will enforce properties on the metal ion that enhance its potential catalytic function. This very unique protein–metal ion interaction alters the properties of each component and the result is a catalytically active state (Williams, 1985). Redox–active

copper enzymes provide an example of this phenomenon where the protein scaffold geometrically constrains copper cofactor to adopt a coordination geometry that is unfavorable in solution but optimal for catalysis (Williams, 1995; Yu *et al*., 2001). In principle, an entatic state does not have to be only a geometrically constrained state. It is entirely possible that the geometry of a metal ion bound to a protein can resemble that of its solution state, and that the entatic state only pertains to the alteration of its electrostatic properties.

The entatic state does not always cause a destabilization of the metal ion, nor is it always accompanied by a conformational change of the protein. It is often incorrectly associated with the 'rack mechanism', which proposes that a protein acts as a structure–enforcing scaffold; however, these two theories are mutually exclusive (Lumry and Erying, 1954). The IUPAC definition of the entatic state refers to the state of an atom or group which, due to its binding in a protein, has its geometric or electronic condition adapted for function; however, as it pertains to an enzyme, the entatic state can be simply described as the best ground state conformation for catalysis, which arises from binding a cofactor (IUPAC Recommendations, 1997). The formation of an entatic state does not require a dramatic change in the ground state energy of the protein, or, a conformational change that is complementary to the transition state (Williams, 1985). Since, MR requires coordination of a metal ion cofactor prior to substrate binding (Maggio *et al*., 1975), it must therefore enter an entatic state prior to catalysis. The nature of the entatic state of MR has not been discussed or explored previously.

1.6 Overview

MR catalyzes the interconversion of the enantiomers of mandelate via an *aci*–carboxylate intermediate. Extensive studies have identified the catalytic residues involved in the reaction and estimated their energetic contributions to catalysis; however, there are limited experimental data delineating the role of the essential cofactor Mg^{2+}. Is the role of Mg^{2+} to remove electron density of the enzyme–bound substrate in the ground–state to lower the p*K*a of the α-carbon proton? Or does it play a role in stabilizing the increased negative charge of the enolate intermediate? It is possible that the metal ion's contribution is not an electrostatic one, but instead that the metal ion acts to orient the active site and coordinate the substrate, locking it in position for catalysis. Perhaps it induces an energetically unstable conformation of the substrate in the active site to allow for catalysis. These are some of the questions I intend to address in this thesis.

Chapter 2 will outline the experimental identification of metal ions that are cofactors for MR and provide insight into the nature of their interaction with MR. It also includes the kinetic characterization of each metalloenzyme with the natural substrates (*R*)– and (S)–mandelate and the resulting alteration of the pseudosymmetry of the enzyme. Consideration will also be given as to how MR differentiates between metal ions and how they alter the kinetics of the reaction catalyzed by MR.

Chapter 3 focuses on determining the effect that changing the metal ion has on the ability of MR to stabilize the transition state. Generally, for a series of mutant enzymes that catalyze the same reaction, an ideal transition state mimic will give a slope equal to 1 in a linear free energy plot of log K_i versus log (K_m/k_{cat}) (Mader and Bartlett, 1997). If the metal ion plays a role in transition state stabilization, then the change in binding affinity (K_i) of the intermediate analogue benzohydroxamate should parallel the change in

catalytic efficiency (k_{cat}/K_m) that arises due to metal ion substitution. Chapter 3 will focus on describing how the binding affinity of the dianionic inhibitor benzoylphophonate compares between metalloenzymes, to determine if the interaction between ligand and metal ion is predominantly charge related. Chapter 3 also details an isothermal titration calorimetry (ITC) study on complexes formed between the metal ions Mg^{2+}, Ni^{2+}, Co^{2+} and Mn^{2+} with the inhibitors benzoylphosphonate and benzohydroxamate. The stability constants determined by this ITC study will be used to adjust the binding constants (K_i) of the two inhibitors for MR, thereby accounting for a reduction in their apparent solution concentrations arising from complex formation.

In Chapter 4, I measured the ability of the different metal bound variants of MR to catalyze the racemization of the alternative substrate (*S*)–trifluorolactate (TFLA). The racemization of TFLA by MR is a reaction for which the chemical step (k_2) is rate limiting (Nagar *et al*., 2011). If the role of the metal ion is to stabilize the high–energy intermediate, then the efficiency for the reaction involving the alternative substrate TFLA should change upon substitution of the various metal ions. Chapter 4 will also address the effect of varying the microviscosity of the solvent on the reaction catalyzed by Mn^{2+}–bound MR to determine if the partial dependence of k_{cat} and k_{cat}/K_m on product dissociation and/or substrate association changes relative to the wild–type MR.

Finally, Chapter 5 provides a summary of the findings of this thesis and outline proposed future work. The overarching goal of this thesis is to more clearly establish the role of the metal ion cofactor in the reaction catalyzed by MR.

Chapter 2

Metal Ion Activation of MR

2.1 Introduction

MR from *Pseudomonas putida* requires the divalent metal cation Mg^{2+} as an essential activator to catalyze the racemization of mandelate, but will also utilize Ni^{2+}, Co^{2+}, Mn^{2+}, and possibly Fe^{2+}, in place of Mg^{2+} (Weil-Malherbe, 1966; Fee *et al*., 1974). To date, only these metal ions have been identified as cofactors of MR. As such, MR may be considered a cambialistic (from the latin *cambialis*, meaning change) enzyme because of its ability to substitute its metal ion cofactor (see discussion for further information). Crystal structures of MR also show Mg^{2+} (Landro, *et al*. 1994; Neidhart, *et al*. 1991; Nagar *et al*. 2014; Schafer *et al*. 1996; Lietzan, *et al*. 2012), and in one case Mn^{2+} (Neidhart, *et al*. 1991), to be invariably octahedrally coordinated to the MR active site residues Glu 247, Glu 221, and Asp 195 (Neidhart *et al*., 1991). X–ray crystal structures of MR show that either three water molecules, or one water molecule and a bidentate chelated ligand, will occupy the other three sites of the octahedron. A visual example of this can be seen in the crystal structure of the (*S*)–mandelate analogue, (*S*)–atrolactate, bound to wild–type MR (**Figure 2.1**) (Landro *et al*. 1994). Incubation of apo–enzyme with Zn^{2+} prior to introducing Mg^{2+} will prevent Mg^{2+} activation without mis–folding of the protein, indicating that Zn^{2+} and Mg^{2+} bind at the same site; however, the enzyme is inactive when Zn^{2+} is bound (Fee *et al*., 1974). One crystal structure of MR shows Eu^{2+} bound at the Mg^{2+} site of MR, and it is known to be a potent inhibitor of MR (Neidhart *et al*., 1991; Powers, 1989).

At present, it is presumed that the role of Mg^{2+} in MR catalysis is to stabilize the increased negative charge of the enolate intermediate and/or enhance binding of the

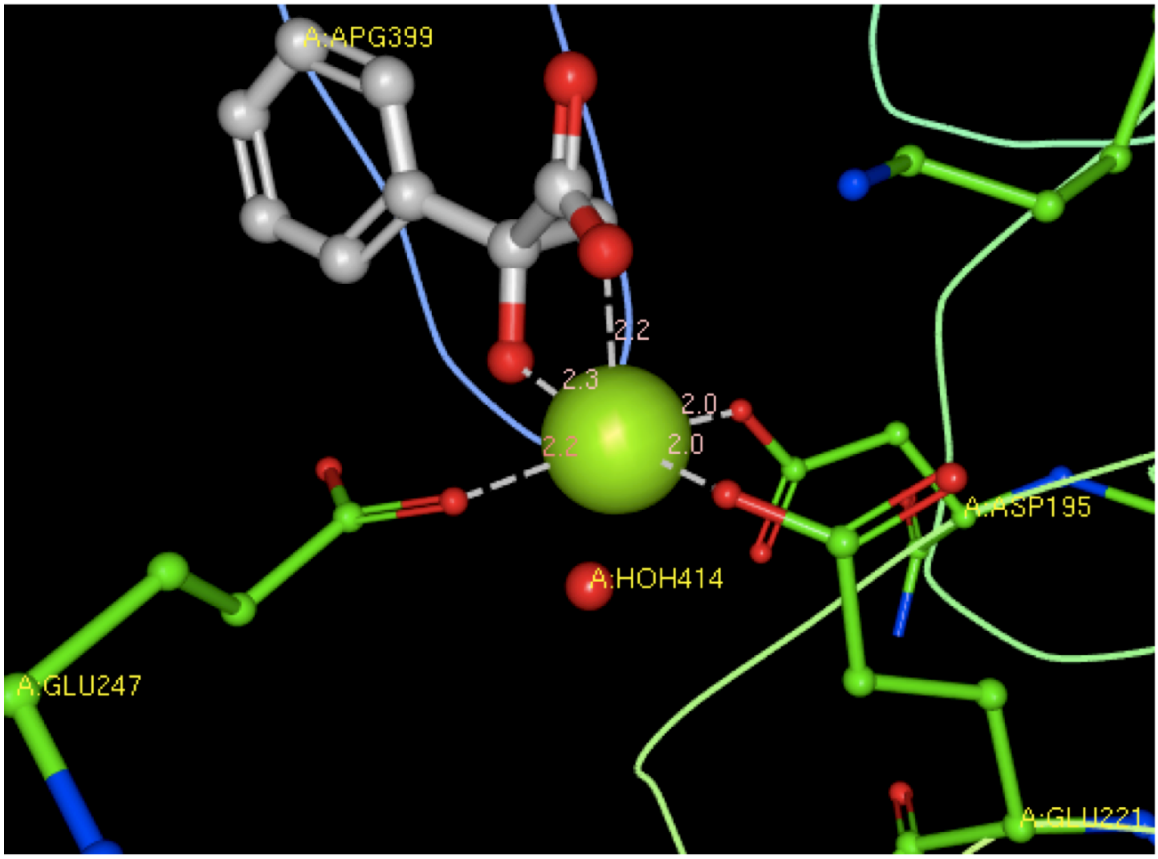

Figure 2.1 X–ray crystal structure of MR highlighting the active site Mg^{2+} bound with an octahedral geometry [PDB = 1MDR (Landro *et al.*, 1994)]. Mg^{2+} is shown coordinated to the active site residues Glu 247, Glu 221, and Asp 195, one water molecule, and chelated in a bidentate fashion by the substrate analogue (*S*)–atrolactate. The distances shown are in Å.

substrate in the ground–state and, by withdrawing electron density, lower the pK_a of the α–proton (Guthrie and Kluger, 1993). In either scenario, the possibility arises that a number of divalent metal cations can be substituted for Mg^{2+} and that these metal ions will provide enough of an electrostatic interaction for MR to retain its catalytic activity, albeit with less efficiency. The identification of a number of different metal ion cofactors provides an opportunity to study a number of metal ion–bound variants of MR with varying efficiencies and should allow us to probe the role of the metal ion in catalysis.

In addition to outlining some of the common techniques used throughout this thesis, such as the expression, purification, and CD–based assay for MR, the main foci of this chapter will be the identification of metal ions that activate MR and the determination of the activation constants (K_A) for those metals. To accomplish this, all possible contaminating divalent metals were removed from the expressed recombinant enzyme to generate the inactive apo–enzyme. Next, a number of divalent, and a few mono– and trivalent, metal cations were incubated with the apo–enzyme at varying concentrations in an attempt to restore activity. Despite extensive testing on a wide range of metals, the only metal ions found to restore activity to MR were Mg^{2+}, and the 3d–block transition metals Mn^{2+}, Ni^{2+}, Co^{2+} and Fe^{2+}. Metal–ion bound MR was fully characterized using either (*R*)– or (*S*)–mandelate as substrate (the exception being Fe^{2+} which proved problematic for reasons to be addressed later in this chapter). These findings are similar to what had been found previously by Fee *et al*. (1974); however, the present study builds on the previous studies by providing a detailed kinetic characterization of the MR–metal ion variants. This chapter will focus on understanding

the preference MR shows for various metal ions as activators, and demonstrate the effect of altering the type of activator on the activity of MR.

2.2 Materials and Methods

2.2.1 General

(*R*)–Mandelic acid, ethylenediaminetetraacetic acid disodium salt dihydrate (EDTA), anhydrous or hydrated metal–chlorides (**Table 2.1**) and all chemicals, unless otherwise stated, were of reagent grade or better and purchased from Sigma–Aldrich Canada, Ltd. (Oakville, ON). Circular dichroism (CD) assays were conducted using a JASCO J–810 spectropolarimeter.

2.2.2 Expression and Purification of Recombinant StrepII–MR

Recombinant MR from *Pseudomonas putida* was over–expressed in and purified from *Escherichia coli* BL21 (DE3) cells transformed with a pET–52b(+)–wtMR plasmid containing the MR open reading frame, encoding the MR gene product (MASWSHPQFEKGALEVLFQGPGYHM$_1$...MR) as a fusion protein with an N–terminal StrepII tag (underlined; M_1 represents the first amino acid of wild-type MR) (Narmandakh and Bearne, 2010). In all assays, the recombinant MR bearing the N–terminal StrepII tag was used as it was previously shown that removal of this tag had no effect on k_{cat} or K_m (Narmandakh and Bearne, 2010). *E. coli* cells were grown without induction in Luria–Bertani (LB) medium (2 L) containing ampicillin (100 μg/mL) at 37 ˚C. Isopropyl β–D–thiogalactopyranoside (IPTG) was not used for induction of expression because the levels of soluble protein are approximately equal with and without addition of IPTG (Narmandakh and Bearne, 2010).

The cells were harvested at logarithmic phase (OD_{600}~1) after 5 h of growth by

centrifugation (1541 × *g*, 10 min, 4 ˚C), suspended in 20 mL of 0.1 M Tris–HCl buffer, pH 8.0 containing 150 mM NaCl and 1 mM EDTA, and lysed by sonication on ice (6 × 15 s bursts with 30 s cooling intervals using a Branson sonifier 250 with a power setting of 5.5). The crude cell lysate was clarified by ultracentrifugation (109,760 × *g*, 30 min, 4 ˚C), and the enzyme was purified by affinity chromatography using *Strep*–Tactin Superflow resin according to the manufacturer's instructions (IBA GmbH, Göttingen, Germany) and published protocols (Narmandakh and Bearne, 2010). The affinity–purified enzyme was eluted with 0.1 M Tris–HCl buffer, pH 8, containing 150 mM NaCl, 1 mM EDTA, and 2.5 mM desthiobiotin, and dialyzed twice against 0.1 M Na^+–HEPES buffer, pH 7.5, containing 200 mM NaCl and 10% v/v glycerol, at 4 ˚C for over 16 h.

2.2.3 Generating Metal Ion–Free Apo–MR

The above protocol was altered to include extensive dialysis of wild–type MR to purify the metal ion–free apo–enzyme. After elution from the *Strep*–Tactin resin, the enzyme was dialyzed against 0.1 M Na^+–HEPES buffer (1L), pH 7.5, containing 10 mM EDTA twice for 16 h, followed by dialysis four times for 24 h against 0.1 M Na^+–HEPES buffer (1L), pH 7.5, containing 200 mM NaCl, in order to remove EDTA. The apo–enzyme was aliquoted (500 μL) and stored at –20 ˚C. No activity was observed for the apo–enzyme.

2.2.4 Circular Dichroism (CD)–Based Assay of MR Activity

MR activity was measured using the circular dichroism (CD)–based assay developed by Sharp *et al*. (1979). The approach to equilibrium can be measured for either (*R*)– or (*S*)– mandelate by observing the dichroic absorption band at 260 nm (molar ellipticity of +370 and –370 deg $mol^{-1}cm^2$ for (*R*)– and (*S*)–mandelate, respectively).

Equation 2.1 shows the change in ellipticity for the system.

$$\frac{d\theta}{dt} = [\theta]_R l\left(\frac{d[R]}{dt} - \frac{d[S]}{dt}\right) \quad 2.1$$

The observed ellipticity (θ) for the sample is in degrees, R and S represent the molar concentrations of (*R*)– and (*S*)–mandelate, respectively, $[\theta]_R$ is the molar ellipticity of (*R)*–mandelate (deg M^{-1} cm^{-1}) and l is the pathlength (cm). Modification of this equation gives equation 2.2,

$$v_i = \frac{1}{2[\theta]_R l}\left(\frac{d\theta}{dt}\right) \quad 2.2$$

which allows determination of the initial velocity of the reaction catalyzed by mandelate racemase by following the change in the observed ellipticity with time(Sharp *et al*., 1979).

All metal ion activation assays were conducted at 25 ˚C using a quartz cuvette with a 1–cm pathlength (total volume 2 mL) in Na^+–HEPES buffer (100 mM, pH 7.5). Prior to initiating the reaction by addition of a saturating concentration of the substrate (*R*)–mandelate (10 mM), varying concentrations of MR (typically between 0.15 and 1.5 μg/mL) were incubated (20 min) with an increasing concentration of the metal ion activator (0.001 mM – 10.000 mM of metal–chloride salt in assay buffer).

Upon the identification of activating metal ions, an appropriate concentration of enzyme was used for each activator (0.15, 0.20, 0.20, and 1.05 μg/mL for Mg^{2+}, Co^{2+}, Ni^{2+}, and Mn^{2+} respectively, containing 0.05% BSA) to conduct the activation assay and determine the activation constant (K_A). Following this, MR enzymatic activity was determined in the presence of saturating concentrations of each metal ion ($10 \times K_A$), and

varying concentrations of either (*R*)– or (*S*)–mandelate from 0.25–15.00 mM to determine the kinetic parameters K_m and k_{cat}.

2.2.5 Data Analysis

The apparent values of K_A were determined from plots of the initial velocity (v_i) versus metal ion concentration ($[M^{n+}]$ where M is a cation and n is an integer equal to 1, 2, or 3) by fitting equation 2.3 to the initial velocity data.

$$v_i = \frac{V_{max}[M^{n+}]}{K_A + [M^{n+}]} \tag{2.3}$$

A second apparent binding constant (K_A'), observed for Co^{2+} and Ni^{2+}, was determined by fitting equation 2.4 to the initial velocity data.

$$v_i = \frac{V_{max}[M^{n+}]}{K_A + [M^{n+}]\left(1 + \frac{[M^{n+}]}{K_A'}\right)} \tag{2.4}$$

The apparent values of V_{max} and K_m were determined from plots of the initial velocity (v_i) versus substrate concentration ([S]) in the presence of a saturating concentration of metal ion ($[M^{n+}] = 10 \times K_A$) by fitting equation 2.5 to the initial velocity data.

$$v_i = \frac{V_{max}[S]}{K_m + [S]} \tag{2.5}$$

Curve fitting was conducted using nonlinear regression analysis and the program *KaleidaGraph* v. 4.0 from Synergy Software (Reading, PA). All kinetic parameters were determined in triplicate and average values are reported, with the reported errors being standard deviations. Protein concentrations were determined by measuring the absorbance at 280 nm using the molar extinction coefficient of 53, 400 $M^{-1}cm^{-1}$ (calculated using ProtParam tool available on the ExPASy server:

http://web.expasy.org/protparam (Gasteiger *et al*., 2005)). The k_{cat} values were calculated by dividing V_{max} values by total enzyme concentrations ($[E]_t$) using an MW value of 41, 264 Da.

2.2.6 CD Spectra of Apo– and Metal Ion-Bound MR

The CD spectra for both apo and metal ion–bound MR were recorded in sodium phosphate buffer (25 mM, pH 7.5) in a quartz cuvette with a 0.1–cm light path over a wavelength range from 195 nm to 260 nm at 25 ˚C. The enzyme concentration used was 65 μg/mL, the apo–enzyme solution contained no metal ion. Metal ion-bound variants contained excess amounts of Mg^{2+} (3.9 mM), Co^{2+} (1 mM), Mn^{2+} (1 mM), or Ni^{2+} (1 mM) as their chloride salts. This experiment was conducted in an attempt to observe alterations to the secondary structure of MR in both the presence and absence of metal ions. The ellipticity of three spectra of buffer were averaged and subtracted from corresponding averaged values from three spectra of the enzyme containing solution.

2.3 Results

2.3.1 Identification of MR Activators

A list of the metal ions tested and the determined binding constants (K_A) are given in **Table 2.1**. Before a metal ion was deemed not to be an activator, it was extensively assayed using a wide range of enzyme concentrations, varied lengths of time, and saturating concentrations of substrate. Of all metal ions tested, only Mg^{2+}, Mn^{2+}, Co^{2+}, Ni^{2+}, and Fe^{2+}, were able to restore activity. The binding constants followed the order of $Mg^{2+} > Ni^{2+} > Co^{2+} > Mn^{2+}$. The K_A of Fe^{2+} was immeasurable, due to fluctuation of the observed ellipticity during the assay and precipitation of the protein over a short amount of time. Measurements of solutions containing metal ion and substrate were conducted to

Table 2.1 MR activation constants for cations tested[a].

cation	corresponding salt	K_A (mM)	K_A' (mM)
Li^+	$LiCl_2$	–[b]	–
Mg^{2+}	$MgCl_2$	0.394 (± 0.001)	NA[c]
Al^{3+}	$AlCl_3$	–	–
Ca^{2+}	$CaCl_2•2H_2O$	–	–
Sc^{3+}	$ScCl_3$	–	–
V^{2+}	VCl_2	–	–
Cr^{2+}	$CrCl_2$	–	–
Cr^{3+}	$CrCl_3•6H_2O$	–	–
Mn^{2+}	$MnCl_2•4H_2O$	0.040 (± 0.002)	NA
Fe^{2+}	$FeCl_2$	immeasurable	unknown
Co^{2+}	$CoCl_2•6H_2O$	0.057 (± 0.004)	4.1 (± 0.6)
Ni^{2+}	$NiCl_2$	0.091 (± 0.001)	11 (± 1)
Cu^{2+}	$CuCl_2$	–	–
Zn^{2+}	$ZnCl_2$	–	–
Sr^{2+}	$SrCl_2$	–	–
Cd^{2+}	$CdCl_2•2½H_2O$	–	–
Ba^{2+}	$BaCl_2•2H_2O$	–	–
Hg^{2+}	$HgCl_2$	–	–

[a]Values are means of triplicate trials and reported errors are standard deviations.
[b]No activation observed
[c]Not applicalble

determine if complexation with, and/or racemization of, the substrate occurred in the absence of enzyme. Two metal ions, V^{2+} and Sc^{3+}, were found to form complexes with mandelate at low concentrations, which resulted in a change of the observed ellipticity, but failed to restore MR activity. The CD spectra of apo–enzyme before and after incubation with the activating metal ions showed no change to the secondary structure of MR upon metal ion binding and activation (**Section 2.3.4** and **Figure 2.4**). Two of the metal–ions, Ni^{2+} and Co^{2+}, were found to inhibit MR at higher concentrations and a second binding constant (K_A') was observed (**Figure 2.2**) and measured (**Table 2.1**). The observed inhibition was modeled using **Scheme 2.1** from which equation 2.4 is derived.

2.3.2 Kinetic Characterization of Metal Ion–Bound Variants of MR With the Substrates (*R*)– and (*S*)–Mandelate

The kinetic parameters for MR bound to each metal ion are shown in **Table 2.2**. Interestingly, the kinetic parameter $K_m^{R\rightarrow S}$ for the metalloenzymes follows the order $Mg^{2+} < Ni^{2+} < Co^{2+} < Mn^{2+}$, but the parameter $K_m^{S\rightarrow R}$ follows the reverse trend of $Mg^{2+} > Ni^{2+} > Co^{2+} > Mn^{2+}$. The turnover numbers ($k_{cat}^{R\rightarrow S}$ and $k_{cat}^{S\rightarrow R}$) for the metal ions do not follow a discernable trend, but the result for each reaction direction is that Mg^{2+} has the greatest k_{cat} value and Mn^{2+} the lowest k_{cat} value regardless of the enantiomer used as the substrate. Ni^{2+} and Co^{2+} have very similar values of k_{cat} and vary only in that the k_{cat} of Ni^{2+} is slightly higher in the $S\rightarrow R$ reaction direction and the k_{cat} of Co^{2+} is slightly higher in the $R\rightarrow S$ reaction direction. The efficiencies (k_{cat}/K_m) follow the order $Mg^{2+} > Co^{2+} > Ni^{2+} > Mn^{2+}$ in the $R\rightarrow S$ reaction direction and $Co^{2+} \approx Mg^{2+} > Ni^{2+} > Mn^{2+}$ in the $S\rightarrow R$ reaction direction. Interestingly, there is a change in the apparent equilibrium constant calculated using the Haldane relationship (**Section 1.1.5**), such that a deviation from

Scheme 2.1 A possible kinetic mechanism for the inhibition of MR by metal ion activator dependent upon occurrence of a second binding event. M^{n+} depicts any metal ion activator. Note: this mechanism does not include any possible isoforms of the enzyme or enzyme bound intermediates.

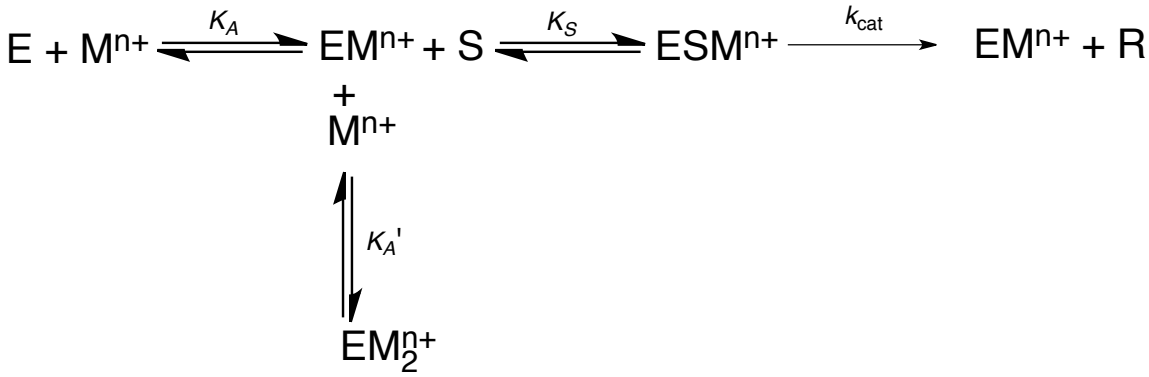

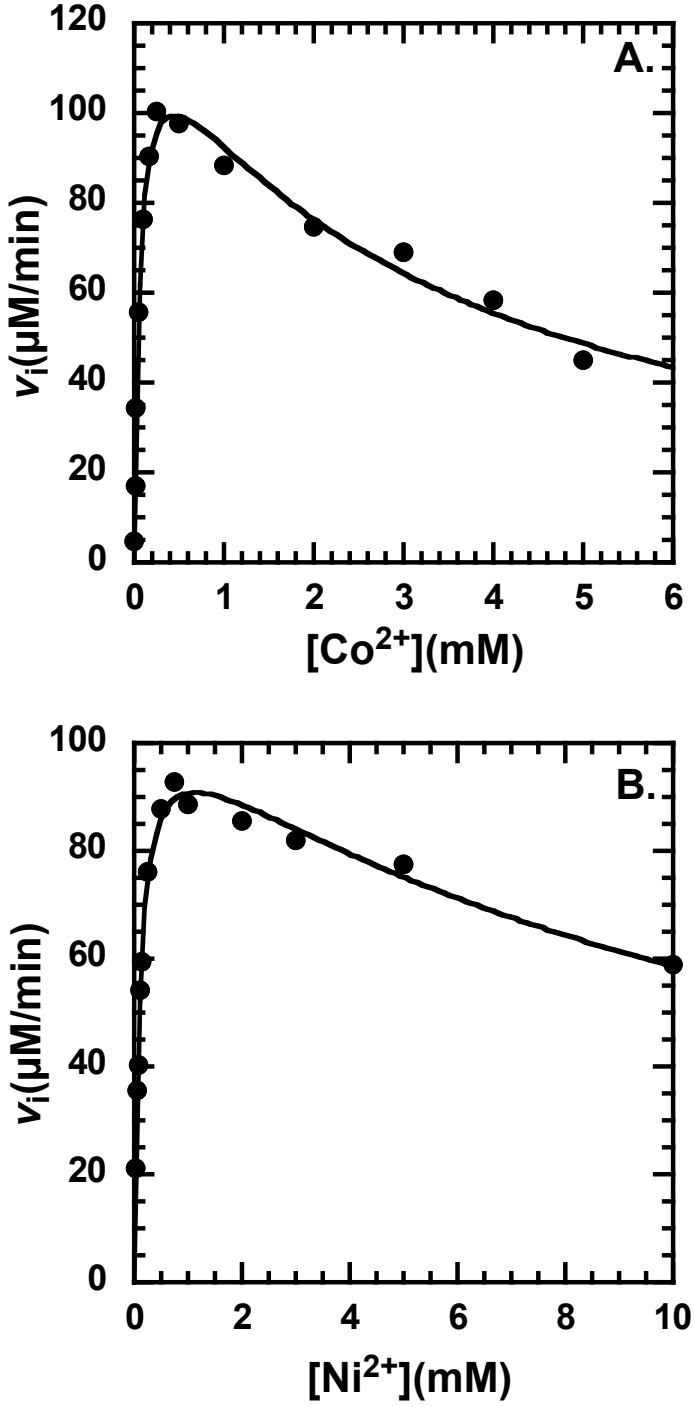

Figure 2.2 Representative plots for the activation of MR by Co^{2+} (A) and Ni^{2+} (B). MR (0.2 μg/mL) was incubated for 20 min with varying concentrations of respective metal ion prior to addition of saturating concentration of substrate (*R*)–mandelate (10 mM). Binding constants (K_A and K_A') were determined using equation 2.4.

Table 2.2 Kinetic constants for the metallo–variants of MR[a]

	$R \rightarrow S$			$S \rightarrow R$			
Metal ion	$K_m^{R\rightarrow S}$ **(mM)**	$k_{cat}^{R\rightarrow S}$ **(s^{-1})**	$k_{cat}/K_m^{R\rightarrow S}$ **($M^{-1}s^{-1}$)**	$K_m^{S\rightarrow R}$ **(mM)**	$k_{cat}^{S\rightarrow R}$ **(s^{-1})**	$k_{cat}/K_m^{S\rightarrow R}$ **($M^{-1}s^{-1}$)**	K_{eq} [b]
Mg^{2+}	0.95 (± 0.07)	753 (± 6)	7.9 (± 0.6) × 10^5	0.71 (± 0.07)	537 (± 14)	7.6 (± 0.8) × 10^5	1.04 (± 0.14)
Mn^{2+}	1.24 (± 0.10)	104 (± 6)	8.4 (± 0.8) × 10^4	0.39 (± 0.02)	70.2 (± 1.4)	1.8 (± 0.1) × 10^5	0.47 (± 0.05)
Co^{2+}	1.10 (± 0.06)	567 (± 30)	5.1 (± 0.4) × 10^5	0.57 (± 0.06)	440 (± 18)	7.7 (± 0.9) × 10^5	0.66 (± 0.09)
Ni^{2+}	1.01 (± 0.05)	506 (± 16)	5.0 (± 0.3) × 10^5	0.66 (± 0.03)	462 (± 29)	7.0 (± 0.5) × 10^5	0.71 (± 0.07)

[a]Values are means of triplicate trials and reported errors are standard deviations.
[b]Calculated from the Haldane relationship: $K_{eq} = ((k_{cat}^{R\rightarrow S}/K_m^{R\rightarrow S})/(k_{cat}^{S\rightarrow R}/K_m^{S\rightarrow R}))$

unity is observed (**Table 2.2**).

2.3.3 Autoxidation of Fe^{2+} to Fe^{3+} and MR Assay Incompatibility

At low concentrations of Fe^{2+} (1 μM), restoration of apo–MR activity was observed; however, as concentrations of Fe^{2+} approached less than half of the probable K_A the observed ellipticity fluctuated dramatically and the assay mixture formed a precipitate. This is not an unexpected phenomenon since it is well–documented that in Good's buffers Fe^{2+} will readily, and rapidly, autoxidize at pH values above 7 to form Fe^{3+} (Welch *et al*., 2002; Tadolini, 1987; Grady *et al*., 1988). The autoxidation in itself is not as problematic as the concurrent production of free radicals of HEPES, which is also, well–studied and well–documented (Welch *et al*., 2002; Tadolini, 1987; Grady *et al*., 1988). The free radicals created, resulted in either polymerization of HEPES and/or denaturation of protein, resulting in precipitate formation. In order to prevent autoxidation, alterations must be made to the assay conditions; this would entail, lowering the pH, lowering the temperature, or addition of a chemical to act as a reducing agent and/or $^{\bullet}OH$ scavenger. Since changing these conditions would no doubt change the efficiency of the enzyme and because Fe^{2+} activation did not appear to activate apo–MR in a manner measurably different than either Ni^{2+} or Co^{2+}, the assay conditions were left as is and Fe^{2+} was not used in subsequent studies. Furthermore, Fe^{2+} binds to benzohydroxamate and forms a complex that precipitates, which would be incompatible with future inhibition experiments with benzohydroxamate that are integral to this thesis (see **Chapter 3**).

2.3.4 Free Energy Profiles of the Reactions Catalyzed by Metalloenzyme Variants of MR

Using the dissociation constants listed in **Table 2.2** as well as equation 2.6:

$$\Delta G^\circ = RT\ln K \qquad 2.6$$

where R is the ideal gas constant, T is the absolute temperature, and K is the dissociation constant (in M), the standard free energy changes accompanying activation by the metal ion (ΔG°_A) and ground state binding (ΔG°_R or ΔG°_S depending on which enantiomer is the substrate and knowing $K_S \approx K_m$ (St. Maurice and Bearne, 2002)) were calculated for each metalloenzyme under standard state conditions and are listed in **Table 2.3**. Using the kinetic parameters listed in **Table 2.2** and equation 2.7:

$$\Delta G^{\ddagger\circ} = RT\ln\left(\frac{k_B T}{h}\right) - RT\ln k \qquad 2.7$$

where k_B is the Boltzman constant, h is Planck's constant, and k is the rate constant k_{cat} (units of s^{-1}) or (k_{cat}/K_m) (units of $M^{-1}s^{-1}$), the free energies of activation were calculated for either the enzyme substrate complex ($\Delta G^{\ddagger\circ}_{ER}$ or $\Delta G^{\ddagger\circ}_{ES}$) and/or the free enzyme and free substrate ($\Delta G^{\ddagger\circ}_{E+R}$ or $\Delta G^{\ddagger\circ}_{E+S}$) for each of the metalloenzymes and are listed in **Table 2.3**.

Since the efficiency of Mn^{2+}–MR was the lowest relative to Mg^{2+}–MR, the free energy profiles for the reactions catalyzed by both Mg^{2+}– and Mn^{2+}–bound MR (**Figure 2.3)** are employed to compare the effect that metal–ion replacement has on MR catalysis. From **Figure 2.3** it is apparent that the most significant energetic change between Mg^{2+}– and Mn^{2+}– bound MR is in the various $\Delta G^{\ddagger}_{E+S}$ and $\Delta G^{\ddagger}_{E+R}$ values and in the ΔG°_{eq} for the reaction. When Mg^{2+} is bound, ΔG°_{eq} is approximately zero but, when Mn^{2+} is the cofactor, ΔG°_{eq} is slightly altered to 0.4 kcal/mol. The most likely explanation for this observation is that altering the metal–ion perturbs the equilibrium between two

Table 2.3 Standard free energy changes for the reaction catalyzed by the metallo–variants of MR.

Metal ion	Mg^{2+}	Mn^{2+}	Co^{2+}	Ni^{2+}
$\Delta G°_{R}$(kcal/mol)	–4.1 (± 0.3)[a]	–3.9 (± 0.3)	–4.0 (0.2)	–4.0 (0.2)
$\Delta G^{‡°}_{ER}$(kcal/mol)	13.53 (± 0.05)	14.7 (± 0.4)	13.7 (± 0.3)	13.8 (± 0.2)
$\Delta G^{‡°}_{E+R}$(kcal/mol)	9.4 (± 0.3)	10.7 (± 0.4)	9.7 (± 0.3)	9.7 (± 0.2)
$\Delta G°_{S}$(kcal/mol)	–4.3 (± 0.4)	–4.7 (± 0.2)	–4.4 (± 0.3)	–4.3 (± 0.3)
$\Delta G^{‡°}_{ES}$(kcal/mol)	13.7 (± 0.1)	14.9 (± 0.1)	13.8 (± 0.2)	13.8 (± 0.4)
$\Delta G^{‡°}_{E+S}$(kcal/mol)	9.4 (± 0.4)	10.3 (± 0.2)	9.4 (± 0.5)	9.5 (± 0.3)
$\Delta G°_{A}$(kcal/mol)	–4.64 (± 0.01)	–6.0 (± 0.3)	–5.8 (0.4)	–5.51 (0.06)
$\Delta G°_{eq}$(kcal/mol)	0.023 (± 0.003)	0.45 (± 0.05)	0.25 (± 0.03)	0.20 (± 0.02)
$\Delta G^{‡°}_{E+R+A}$(kcal/mol)	4.8 (± 0.2)	4.8 (± 0.2)	3.9 (± 0.3)	4.2 (± 0.1)
$\Delta G^{‡°}_{E+S+A}$(kcal/mol)	4.8 (± 0.1)	4.3 (± 0.3)	3.7 (± 0.3)	3.99 (± 0.09)

[a]Values are calculated from **Table 2.2** using equations 2.6 and 2.7.

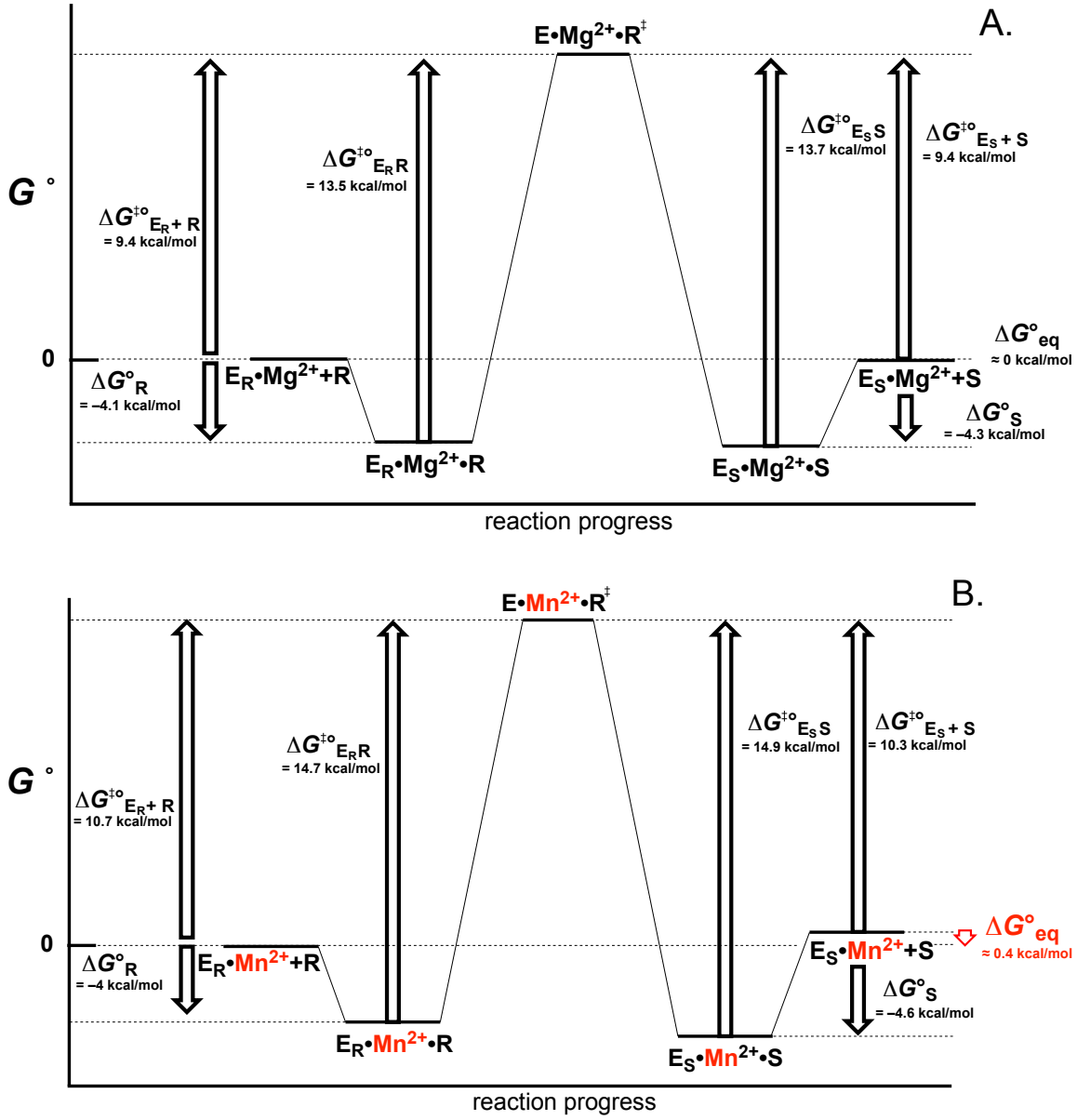

Figure 2.3 Free energy profiles for the reactions catalyzed by MR when either Mg^{2+} (A) or Mn^{2+} (B) is the cofactor. Profiles were constructed using parameters from **Table 2.2** and equations 2.6 and 2.7. The most significant difference between Mg^{2+}–and Mn^{2+}–bound MR is in the ability of the enzyme to stabilize the altered substrate in the transition state and in the free energy of the equilibrium of the enzyme–catalyzed reaction.

conformations of MR; an E_R and an E_S conformation. This effect is most pronounced for Mn^{2+}, although the equilibrum shift is also observed for Co^{2+} and Ni^{2+} albeit to a lesser degree (**Table 2.2**). Replacing Mg^{2+} with Mn^{2+} also moderately (~1 kcal/mol) increases not only the $\Delta G^{\ddagger\circ}_{E+R}$ and $\Delta G^{\ddagger\circ}_{E+S}$ values, but also the $\Delta G^{\ddagger\circ}_{ER}$, and $\Delta G^{\ddagger\circ}_{ES}$ values, indicating that replacing the metal ion alters the ability of the enzyme to stabilize the altered substrate in the transition state; which in the case of Mn^{2+} results in a less efficient enzyme.

2.3.5 CD Spectra of Apo and Metal Ion-Bound MR

The CD spectra of apo–MR and each of the metal ion–bound variants of MR were measured in order to verify that metal ion binding does not cause significant perturbations to the overall protein secondary structure. The dependence of molar ellipticity ($[\theta]$) of MR at various wavelengths remained unchanged in the presence and absence of all metal ion activators, indicating no disturbance to the secondary structure of MR upon metal binding (**Figure 2.4**). An overlay of the $[\theta]$ over a wavelength range from 195 nm to 260 nm for apo, Mg^{2+}, and Mn^{2+}–bound MR, and apo, Co^{2+} and Ni^{2+}–bound MR are shown in **Figure 2.4** as panels **(A)** and **(B)** respectively. There is no observable difference among these plots.

2.4 Discussion

As mentioned in section 2.1, the word cambialistic refers to an enzyme capable of making a cofactor substitution depending upon availability. It has predominantly been used in reference to superoxide dismutase to distinguish between variants that can use different metal–ion cofactors and ones that cannot (Martin *et al*. 1986). In addition to superoxide dismutase, there are several other enzymes that can be classified as

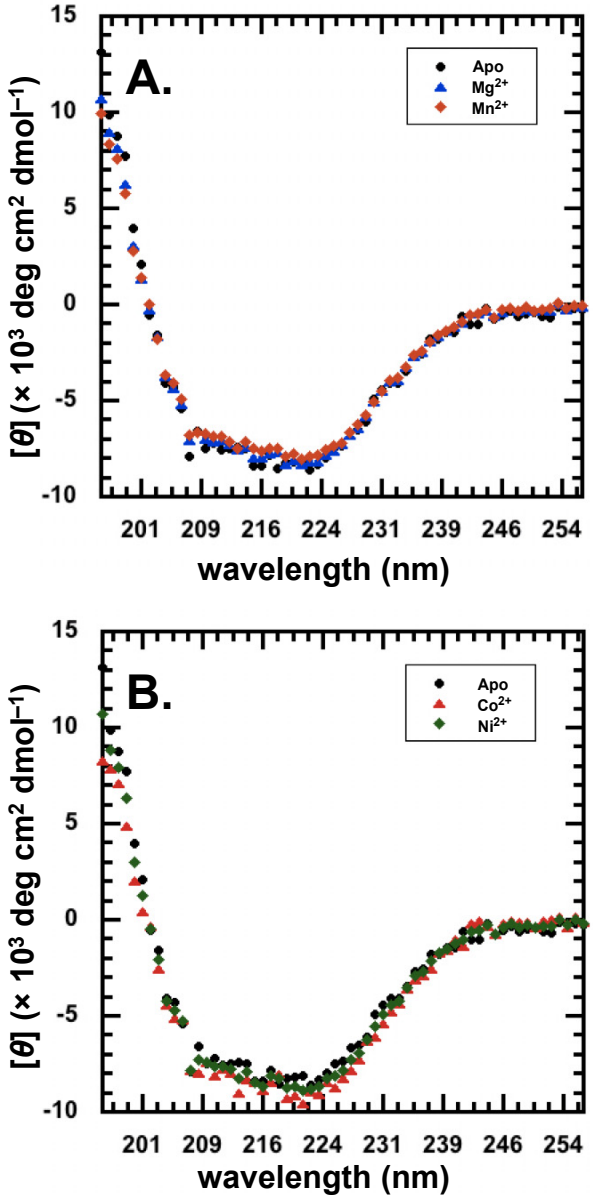

Figure 2.4 CD spectra for apo–MR, Mg^{2+}–bound (A), Mn^{2+}–bound (A), Co^{2+}–bound (B), and Ni^{2+}–bound (B) MR. Molar ellipticities as a function of wavelength are plotted for metal ion–free MR (black), and MR in presence of Mg^{2+} (3.9 mM, blue, plot A), Mn^{2+} (1 mM, red, plot A) Co^{2+} (1 mM, red, plot B), and Ni^{2+} (1mM, green, plot B). Spectra were recorded in Na^{+}-phosphate buffer (25 mM, pH 7.5), at 25 ˚C, with MR concentration of 65 μg/mL and pathlength of 0.1 cm. The molar ellipticity of MR as a function of wavelength did not change in the presence of any of the metal ion activators.

cambialistic. Rat erythrocyte glyoxalase I, for example, utilizes the same divalent metal ions as MR (Mg^{2+}, Mn^{2+}, Co^{2+}, or Ni^{2+}) with little variance amongst K_m and k_{cat} (Han *et al*., 1977). Crystal structures of both human and *E. coli* glyoxalase I (GlxI), with different metal ions bound, indicate that the geometry of the metal ion in the active site determines whether or not the complex is catalytically active (Min He *et al*., 2000). The *E. coli* variant, for example, is inactive when Zn^{2+} is bound but optimally active in the presence of Ni^{2+} and Co^{2+} (Min He *et al*., 2000). Crystal structures of the inactive Zn^{2+} variant revealed that Zn^{2+} binds with trigonal bipyramidal coordination (Min He *et al*., 2000). Conversely, the crystal structures of the active Ni^{2+}– and Co^{2+}–bound forms show octahedral coordination of the metal ion (Min He *et al*., 2000). The apo–GlxI crystal structure shows an RMS of 0.32 Å with the Ni^{2+}–bound variant indicating no significant structural change to GlxI occurs upon binding of the metal ion (Clugston *et al*., 1998). In the case of *E. coli* GlxI, the geometry of the metal ion, rather than the species of the metal ion itself, is a crucial determinant of catalytic activity (Min He *et al*., 2000).

The class II α–mannosidase (GH38) also requires a divalent metal cation for catalysis and can be classified as a cambialistic enzyme, utilizing Co^{2+}, Zn^{2+}, Mn^{2+}, or Cd^{2+} (Nielson *et al*. 2012). Crystal structures of GH38 show the metal ion octahedrally coordinated to 4 residues (2 aspartates and 2 histidines) of the enzyme and bidentate coordination with the substrate (Zhong *et al*., 2008). Despite the fact that GH38 exhibits geometry and coordination of the metal ion that is similar to that of MR, Mg^{2+} does not bind to the active site of GH38 and hence is not an activator of GH38 (Zhong *et al*., 2008). One reason for this is that there are 4-amino acid residue side–chain ligands that coordinate the metal ion in the GH38 active site, the greatest number of ligands Mg^{2+} is

predicted to coordinate is 3 (Dudev and Lim, 2006). In addition, 2 of these residues are histidines, which Mg^{2+} will rarely form a stable coordinate bond with (Dokmanić *et al*., 2008; Dudev and Lim, 2014). Furthermore, in the case of GH38, in the absence of substrate in the active site, the metal ion has a 5–coordinate square pyramidal geometry, which Mg^{2+} cannot assume (Van Den Elsen *et al*., 2001). Like MR, replacement of the metal ion in the active site of GH38 has little effect on the binding affinity of the substrate or the enzymatic efficiency (Hansen *et al*. 2014).

The common trend amongst cambialistic enzymes is that they appear to have unique geometric requirements that a metal–ion cofactor must fulfill in order for them to obtain functionality and their activity remains relatively unchanged regardless of which metal ion is utilized. A recent study has shown that members of the metallo–β–lactamase superfamily of enzymes will adopt different isoforms, which will catalyze different reactions, depending on which of six metals is bound (Cd^{2+}, Co^{2+}, Fe^{2+}, Mn^{2+}, Ni^{2+}, Zn^{2+}) (Bier *et al*., 2015). The metallo–β–lactamase superfamily are not what one would consider cambialistic enzymes, since replacement of the metal cofactor will create a new isoform of the enzyme with an increased repetoire of reactions it can catalyze (Bier *et al*., 2015). A cambialistic enzyme is one that will retain its inherent activity and structure, regardless of metal ion used. Identification and characterization of different metal ions that can activate a cambialistic enzyme could afford insight into the nature of the entatic state of an enzyme, and allow us to study the effect that the metal ion has on the enzyme and vice versa.

2.4.1 Criteria for Selection of Metal Ion Cofactors by MR

Analysis of PDB crystal structures of MR (PDB = 1MDR, 1MNS, 2MNR,

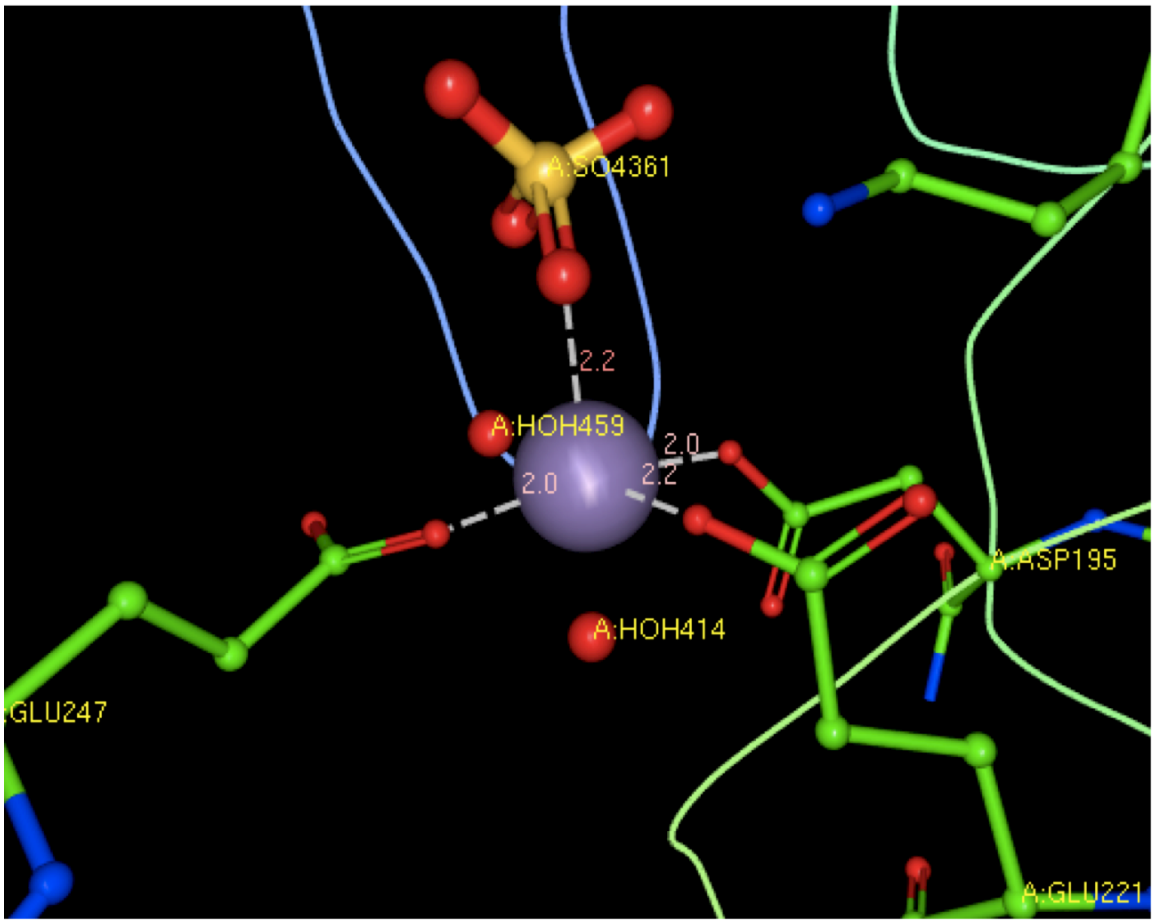

Figure 2.5 X–ray crystal structure of MR highlighting active site Mn^{2+} bound with octahedral molecular geometry at the active site of MR [PDB = 1MDR (Neidhart *et al*., 1991)]. Mn^{2+} is shown coordinated to active site residues Glu 247, Glu 221, and Asp 195, two water molecules, and a sulfate ion. The distances shown are in Å.

4FP1, 1MRA, 4HNC, 4M6U, 3UXL, and 3UXK) from *P. putida* reveals an average coordinate bond length between Mg^{2+} and coordinating ligands of 2.14 ± 0.17 Å and an average octahedral bond angle of 90.1 ± 8.5° (Landro *et al.,* 1994; Lietzan *et al*. 2012; Nagar *et al.,* 2014; Neidhart *et al*., 1991; Schafer *et al*., 1996). This indicates that the hexacoordinate Mg^{2+} found in the active site of MR is at the center of a near perfect octahedron. While no crystal structures exist for either the apo–MR or variants of MR with Ni^{2+}, Co^{2+}, or Fe^{2+} bound, there is one crystal structure of Mn^{2+}–bound MR with an octahedral geometry that is nearly identical to that of the Mg^{2+}–bound MR (**Figure 2.5)** (Neidhart *et al*., 1991). Based on a compilation of data from the Protein Data Bank and the Cambridge Structural Database conducted by both Rulíšek and Vondrášek (1998) and Dokmanić *et al*. (2008), the preferred geometry of Ni^{2+}, Co^{2+}, and Mn^{2+} in both aqueous solution and when protein bound, is octahedral and coordinated to six ligands (Rulíšek and Vondrášek, 1998; Dokmanić *et al*., 2008).

In a six-ligand, octahedral coordination-state, Ni^{2+} will have a high-spin d^8 electron configuration (**Figure 2.6**) (Frausto da Silva and Williams, 1991). Mn^{2+} and Co^{2+} have d^5 and d^7 electron configurations, respectively, and, as is the case with all transition metals in the d^4 to d^7 range, can assume either a high- or low- spin configuration (**Figure 2.6**) (Frausto da Silva and Williams, 1991). The energy difference between the two sets of 3d orbitals (the axial $dx^2–y^2$ and dz^2 orbitals and the diagonal dxz, dyz, and dxy orbitals; designated e_g and $t2_g$, respectively) is called the ligand field stabilization energy (LFSE, represented by Δ_O) and will determine whether Co^{2+} and Mn^{2+} will adopt a high– or low–spin configuration. The Δ_O is determined by the type of ligands coordinated, length of the coordinate bond, and the angles between coordinated ligands, and is unique to each

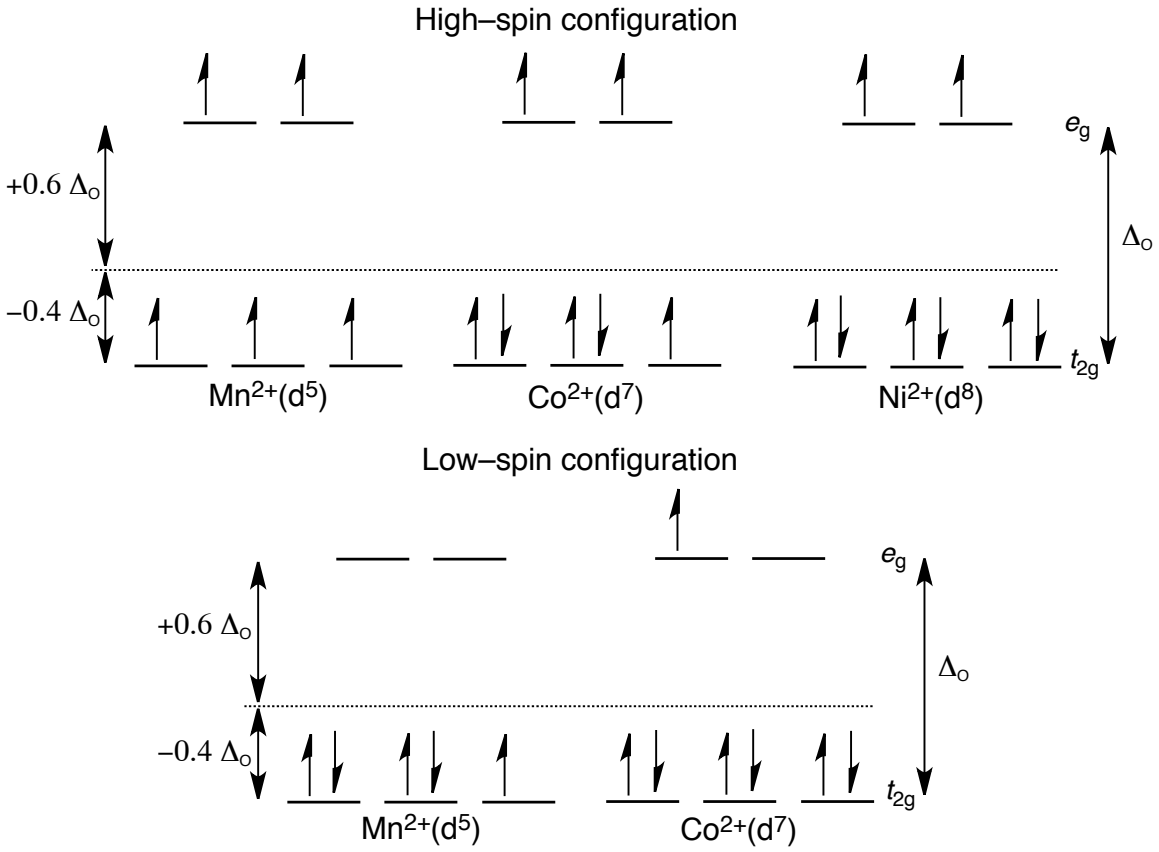

Figure 2.6 Possible electron configurations for transition metals $Mn^{2+}(d^5)$, $Co^{2+}(d^7)$, and $Ni^{2+}(d^8)$. Mn^{2+} and Co^{2+} can adopt either a high–spin or low–spin configuration. The probability of which spin the metal ion will have depends on which is lower in energy, the ligand field stabilization energy (Δ_O), or the energy of electron pairing (Frausto da Silva and Williams, 1991).

system (Griffith and Orgel, 1957). If the ligand field is weak, then the value of Δ_O will be small and a high–spin configuration will be favoured (Griffith and Orgel, 1957). With respect to MR, the three transition metal ions have similar catalytic constants (K_m and k_{cat}) and binding affinities (K_A); hence, it is reasonable to assume that when coordinated to the active site of MR both Mn^{2+} and Co^{2+} will adopt an electron configuration resembling that of Ni^{2+} and, therefore, adopt a high-spin configuration for the majority of the time that they are bound to MR.

The inability of Cr^{2+} (d^4) and Cu^{2+}(d^9) to activate MR is a further testament to the high-spin weak ligand field arrangement in the active site of MR. A high–spin configuration of Cr^{2+} would have only one electron in the e_g orbitals and three in the t_{2g}, which in a weak ligand field, would be an un–stable octahedral configuration (Griffith and Orgel, 1957). Octahedrally coordinated Cu^{2+} on the other hand, would have 3 electrons in the e_g orbital which involves pairing of an electron, a process which may be energetically unfavorable amongst the e_g orbitals in a weak ligand field. In a weak ligand field, Cu^{2+} therefore prefers a tetrahedral configuration, which is not possible in the active site of MR. Due to the relative binding affinities (K_A) of metal ions for MR being around 0.01-0.09 mM, active site coordination requires a relatively high concentration of both free Co^{2+} and Mn^{2+} ($\approx$ 1 mM) in the assay buffer to facilitate binding to MR, and as a result, experimental techniques to elucidate their spin states when bound to MR would be extremely difficult using currently available techniques. Furthermore, this argument does

not apply to Mg^{2+} since there is only one possible electron configuration, which does not rely on LFSE.

An alternative explanation for which metal ion is used by MR may be based on evolutionary pressure rather than the inherent properties of the metal ions that activate it. **Table 2.4** lists some properties of the metal ions Co^{2+}, Mn^{2+}, Mg^{2+}, and Ni^{2+}. One observation of note is that Mg^{2+}, which has the weakest binding affinity (K_A), also has the highest cytosolic concentration of the three metal ions (~ 10^{-3} M) (Romani, 2011). There is little selective pressure for an enzyme, such as MR from *Pseudomonas putida*, to have a tight binding affinity for Mg^{2+} since the free ion is readily available in the cytosol; therefore, the greater K_A value of Mg^{2+} being within the range of the cytosolic concentration makes sense from a physiological perspective. The tight binding affinity for Mn^{2+}, which has a concentration in the μM range in the cytosol (Schramm, 1986), may indicate that, should cytosolic Mg^{2+} levels become low, MR can utilize Mn^{2+} as an alternative cofactor. The moderate binding affinities of Co^{2+} and Ni^{2+} for MR most likely arise from coincidence and not the need of MR to utilize them in the cellular environment since their cellular concentrations are usually subnanomolar (Odaka *et al*, 2013; Li and Zamble, 2009).

There does not appear to be any correlation between the ionic radii of the free metals and their K_A values, indicating that even though the size of the ion may be a factor in whether or not it will bind (e.g., the inability of Ca^{2+} to bind MR due to its large size, **Table 1.1**), ionic size appears to have little, if any, effect on how tightly a metal ion binds to MR or its ability to activate it. A strong correlation does exist between the absolute electronegativity of a metal ion and its K_A value (**Figure 2.7**). The absolute

Table 2.4 Selected properties of Mg^{2+}, Mn^{2+}, Co^{2+}, and Ni^{2+}.

Property	Mg^{2+}	Mn^{2+}	Co^{2+}	Ni^{2+}
Ionic Radius[a](Å)	0.72	0.83 (H.S.)[h] 0.67 (L.S.)	0.75 (H.S.) 0.65 (L.S.)	0.69
Average cytosolic concentration in (M)	10^{-3}[b]	10^{-6}[c]	10^{-9}[d]	10^{-9}[e]
Electron affinity[f](eV)	15.04	15.64	17.06	18.17
Ionization potential[f](eV)	80.14	33.67	33.5	35.17
Electronegativity[f](eV)	47.59	24.66	25.28	26.67
Absolute hardness[f](eV)	32.55	9.02	8.22	8.5
Calculated Z_{eff} for valence shell[g]	3.2	5.6	6.9	7.5

[a]Shannon, 1976
[b]Romani, 2011
[c]Schramm, 1986
[d]Odaka *et al*., 2013
[e]Li and Zamble, 2009
[f]Pearson, 1988
[g]Effective nulear charge (Z_{eff}) calculated using Slater's rules; Slater, 1930
[h]H.S. and L.S. denote high spin and low spin, respectively

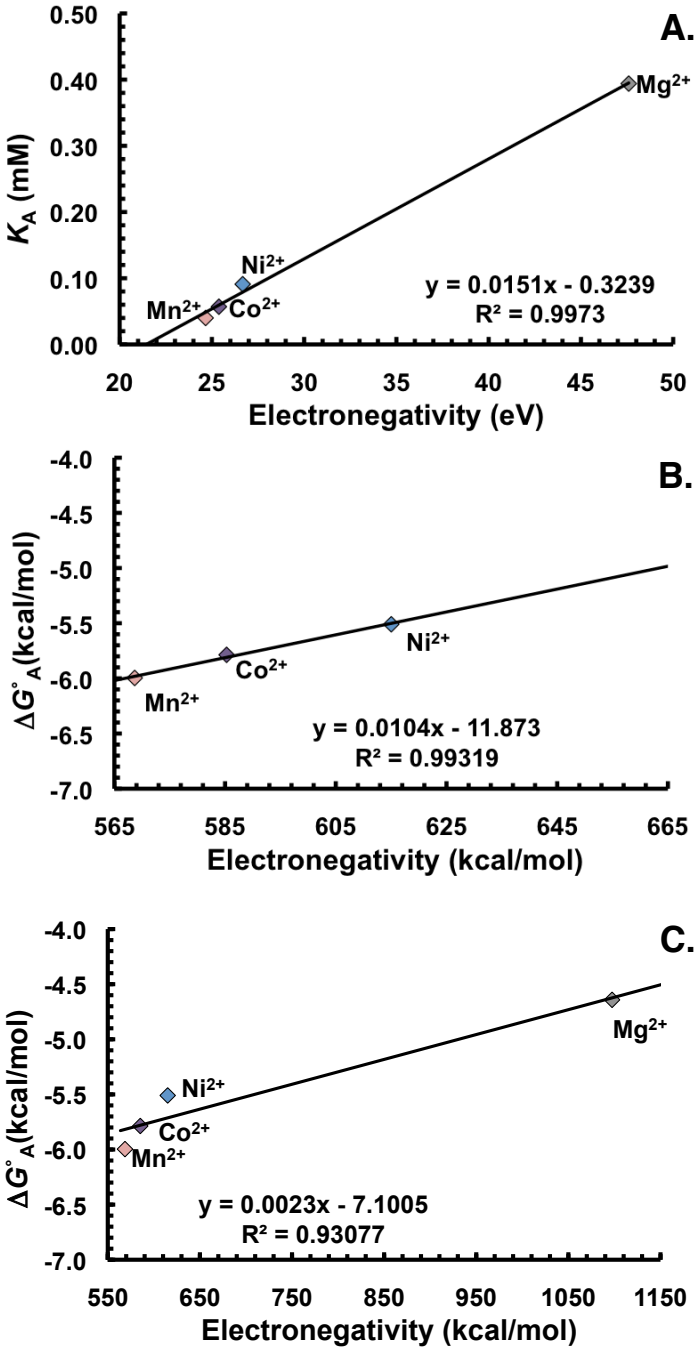

Figure 2.7 The activation constant K_A (mM) versus electronegativity (eV) (A), and the change in free energy of metal ion activation (ΔG°_A) versus electronegativity (kcal/mol) for metal–ion activators of MR both excluding Mg^{2+} (B) and including Mg^{2+} (C). An increase in the activation constant (K_A), which approximates the binding affinity of the metal ion for the active site of MR, correlates with an increase in the absolute electronegativity of the metal ion (A). Plot B includes only transition metals Mn^{2+}, Co^{2+}, and Ni^{2+}, where plot C includes Mg^{2+}. In general, as the electronegativity of the free ion increases the change in binding free energy decreases.

electronegativity (χ) for an atom is defined as its negative of the chemical potential (μ) as shown by equation 2.8 (Parr *et al*., 1978),

$$-\mu = \frac{I + A}{2} = \chi \qquad 2.8$$

where I is the ionization potential of an atom and A is its electron affinity (Parr *et al*., 1978; Mulliken, 1935). Unlike Pauling electronegativity, which applies only to single atoms, the Mulliken, or absolute, electronegativity is constant over an entire molecule or atom. It is the power with which an atom within that molecule draws electrons to itself, and a difference in electronegativity is what drives electron transfer (Mulliken, 1935; Pearson, 1988). If an increase in electronegativity across ions correlates to a decrease in affinity, as it appears to in **Figure 2.7**, then the active site of MR must be fairly electronegative, since it prefers to bind metal ions with low electronegativities. An even better correlation exists between the free energy of metal ion binding ($\Delta G_A°$) and the electronegativity of the transition metals (**Figure 2.7 B**). However, this correlation is diminished when Mg^{2+} is included in the plot (**Figure 2.7 C**). This loss of correlation could be due to an over estimation of the predicted electronegativity of Mg^{2+} (Martin, 1998); or it may be that the activation constant (K_A) for Mg^{2+} underestimates the true binding affinity.

Thus, in order for a metal ion to be an activator of MR it must be an appropriately sized ion with preference for octahedral geometry, both in free solution and when bound to a protein. The transition metals Co^{2+}, Ni^{2+}, and Mn^{2+} will form stable octahedral complexes, most likely due to the ligand field stabilization energy afforded by the MR active site and the electron configuration of the metal ion. The other transition metal ions,

due to their electron configuration, do not have a preference for octahedral configuration, and, therefore are not activators of MR; this is likely the case for Zn^{2+}, Cr^{2+}, and Cu^{2+}. In addition, the affinity of the metal ion for the active site correlates to the electronegativity of the ions; and, this correlation is more pronounced in the case of the transition metals than it is for Mg^{2+}; suggesting, not surprisingly, that the metal ion-binding site of MR is moderately electronegative.

2.4.2 The Energetic Differences of Metal Ion Activation of MR

Using the standard free energy changes calculated in **Table 2.3**, a more detailed free energy profile, which takes into account activation ($\Delta G_A°$) of MR upon binding Mg^{2+}, is shown in **Figure 2.8**. **Figure 2.8** illustrates that the binding of the metal ion is an important step that factors into catalysis. This finding comes from the observance that MR requires pre–incubation with a metal ion activator prior to addition of substrate for catalysis to occur. The activation energy of free enzyme, substrate, and metal ion activator for mandelate racemase ($\Delta G^{‡°}_{E+S+A}$ and $\Delta G^{‡°}_{E+R+A}$) can be determined using equation 2.9 and are listed in **Table 2.3**.

$$\Delta G^{‡°} = RT\ln\left(\frac{k_B T}{h}\right) - RT\ln\left(\frac{k_{cat}/K_m}{K_A}\right) \qquad 2.9$$

The $\Delta G^{‡°}_{E+S+A}$ and $\Delta G^{‡°}_{E+R+A}$ values signify that the metal ion binding to MR lowers the activation barrier allowing for catalysis; however, this value is merely an estimate of the activation energy ($\Delta G_A°$) applying only to the ground state and does not account for a difference in metal ion activation of the transition state. Comparison of both the $\Delta G^{‡°}_{E+S+M^{2+}}$ and $\Delta G^{‡°}_{E+R+M^{2+}}$ values for each metal ion activator relative to the values observed with Mg^{2+} ($\Delta\Delta G^{o} = \Delta G^{‡°}_{E+S+Mg^{2+}} - \Delta G^{‡°}_{E+S+M^{2+}}$ where M^{2+} is either Mn^{2+}, Co^{2+}, or

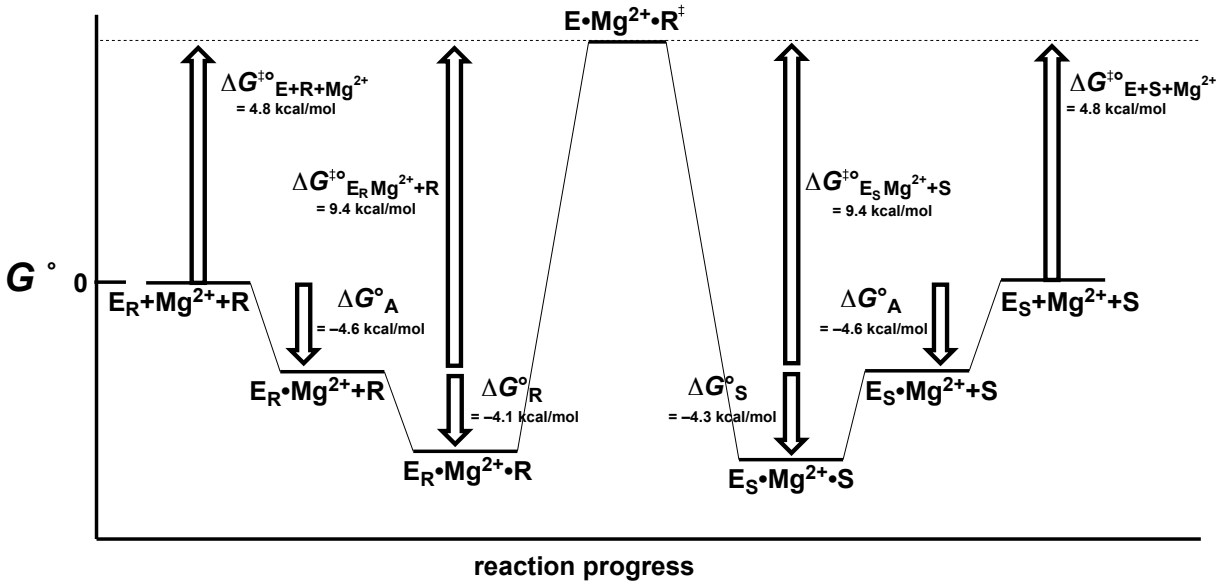

Figure 2.8 Free energy profile for the Mg^{2+}–activated reaction catalyzed by MR. The profile was constructed using the standard state free energies changes from **Table 2.3**, which were calculated using the parameters from **Table 2.2** and equations 2.6, 2.7, and 2.9. R and S represent (*R*)– and (*S*)–mandelate, respectively. In this free energy profile, it is assumed that the K_A is the same for E_R and E_S, although this may not be true, it is unlikely that the value is not altered significantly by the relative protonation states of the free enzyme.

Ni^{2+}) is illustrated in **Figure 2.9,** which illustrates that, relative to Mg^{2+}, the other metal ions provide slightly better activation. This is particularly evident for Co^{2+} and Ni^{2+}. It should be noted that none of the values of $\Delta\Delta G^{o}$ are greater than 1.2 kcal/mol, and are all within experimental error of one another, with p–values when *S*– and *R*–mandelate are the substrates of 0.67 and 0.78 respectively in a Chi–squared test. Because these values are not different at a significance threshold of 0.05, the metal ions do not differ in their ability to activate the reaction catalyzed by MR.

2.4.3 Metal Ion–Dependent Alteration of the Equilibrium for the Free Conformations of MR

There are currently no crystal structures of apo–MR. However, because no alterations to the secondary structure of MR were observed upon binding of any of the metal ion activators, both in previous studies (Fee *et al*. 1974) and in this study (**section 2.3.5**), and because the Mg^{2+}– and Mn^{2+}–bound X–ray crystal structures of MR show no significant differences in tertiary structure (Landro *et al*., 1994; Neidhart *et al*., 1991), it is unlikely that metal–ion binding to MR causes a significant alteration to the global conformation of the enzyme (Fee *et al*. 1974). However, when the metal ion is replaced, there is an increase in the affinity of MR for (*S*)–mandelate relative to (*R*)–mandelate. In fact, comparison of the binding affinities for each enantiomer ($K_m^{R\rightarrow S}$ and $K_m^{S\rightarrow R}$) shows that upon replacement of metal ion cofactor they are inversely correlated (**Figure 2.10**). Such a correlation for $K_{cat}^{R\rightarrow S}$ and $K_{cat}^{S\rightarrow R}$ is not observed. At present, it is not clear how the inverse relationship between K_m values arises.

Altering the metal ion also alters the apparent K_{eq} value for the enzyme-catalyzed reaction as discussed earlier (**section 2.3.1**). Both the altered K_m values and apparent K_e

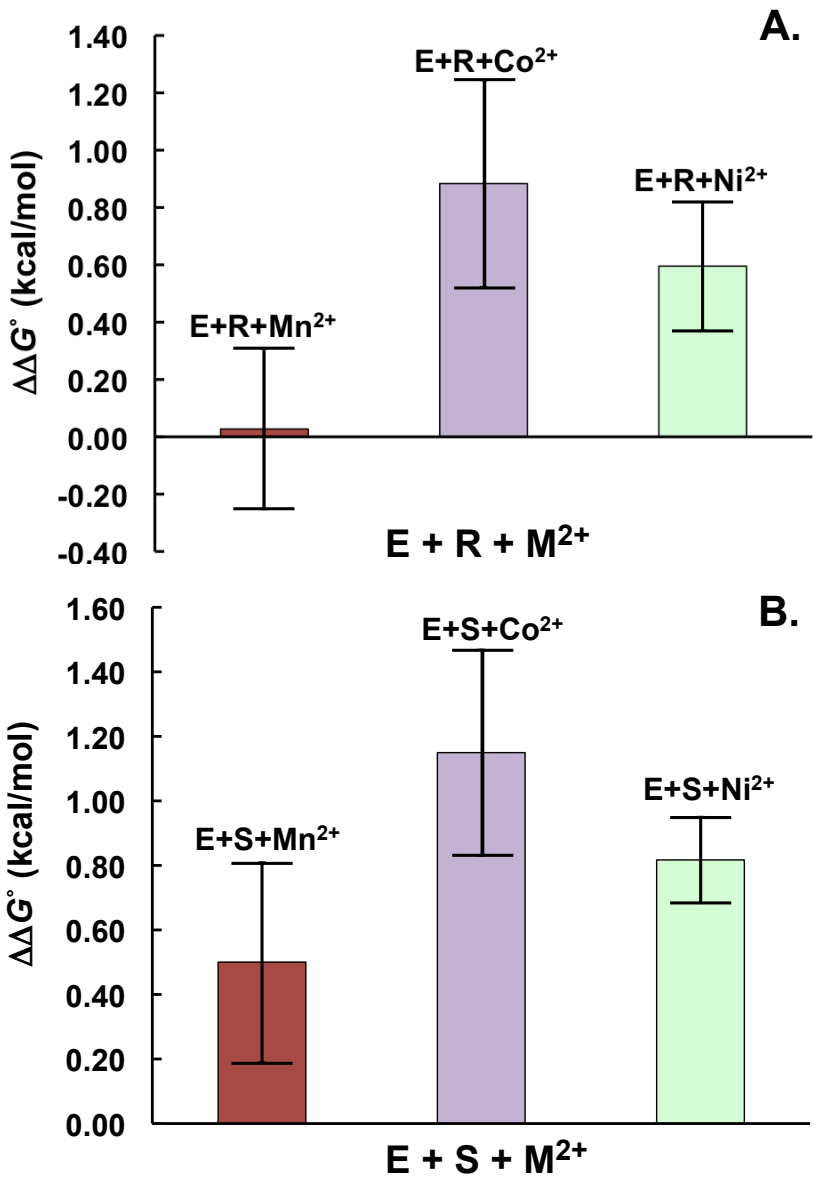

Figure 2.9 $\Delta\Delta G^{o}$ for metal ion–dependent activation in both the *R*→*S* (A) and *S*→*R* (B) reaction directions relative to the Mg^{2+}-dependent reaction. $\Delta\Delta G^{\circ} = \Delta G^{\ddagger\circ}_{E+Substrate+Mg^{2+}} - \Delta G^{\ddagger\circ}_{E+Substrate+M^{2+}}$ where M^{2+} represents Mn^{2+}, Co^{2+}, or Ni^{2+}. Using a chi–square goodness of fit test, the p–values when *S*– and *R*–mandelate are the substrates are both > 0.05 and therefore not significantly different.

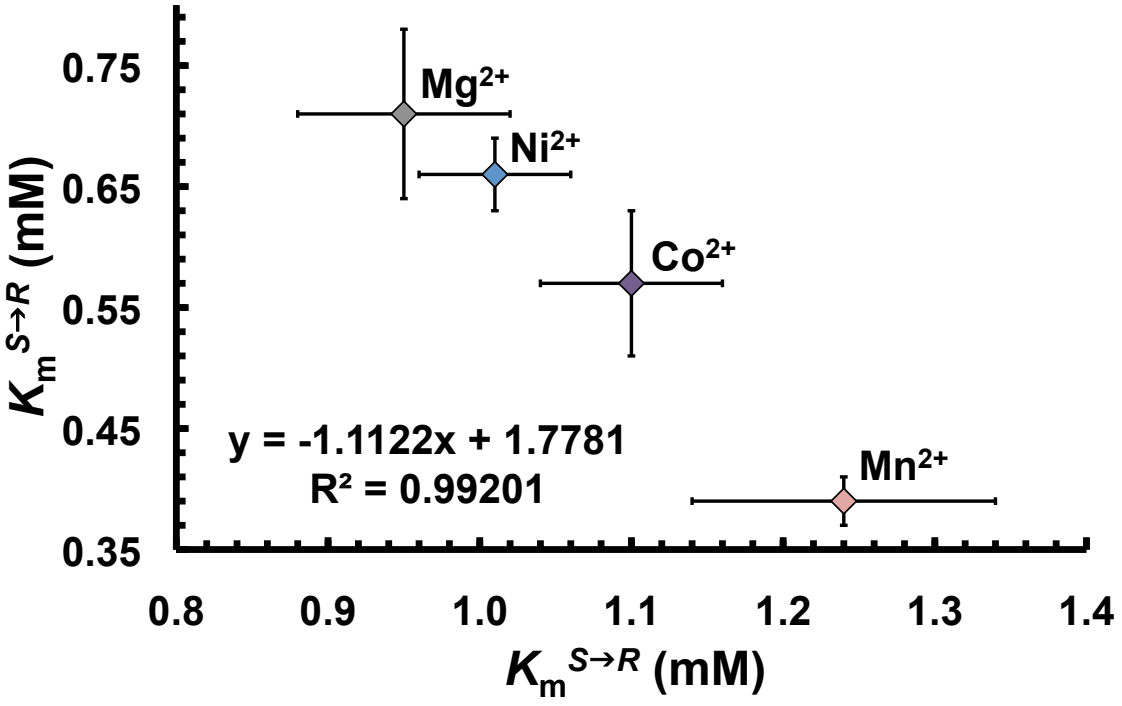

Figure 2.10 Correlation of the binding affinities of the metal–bound variants of MR for the enantiomers of mandelic acid ($K_m^{R\rightarrow S}$ and $K_m^{S\rightarrow R}$).

values that result from switching metal ions suggest that subtle structural differences between the metal–bound enzymes do exist. A likely explanation for the altered K_{eq} values is that MR exists as two forms of free enzyme, E_S and E_R, which are enantiospecific and that the type of metal–ion bound plays a role in altering the equilibrium between these two species. A kinetic mechanism, which includes metal–ion activation, is shown in **Scheme 2.2**. An enzyme with a kinetically significant isomerization of free enzyme can be predicted to have an iso–mechanism (Britton, 1973; Cleland, 1963). In the case of MR, the difference between the two conformers could be as simple as the protonation states of the catalytic residues Lys 166 and His 297. Since the reprotonation of an active site residue is usually a rapid process in water, it is difficult to identify an iso-mechanism for an enzyme where the two conformations are different protonation states. However, through the use of kinetic isotope experiments, tracer perturbation methods, and by following the reaction at different time courses, Knowles and co-workers were able to show an iso-mechanism involving the protonation states of the two active site cystine residues of proline racemase (Fisher *et al*., 1986a; Fisher *et al*., 1986b; Fisher *et al*., 1986c).

It may be that an iso–mechanism exists for MR and that changing the metal ion activator causes a perturbation of the p*K*a values of the catalytic residues allowing us to observe this mechanism. The case may exist that the equilibrium between the two conformations of apo-enzyme in free solution and the equilibrium between the two metal–bound conformations is not the same (hence the α coefficient in **Scheme 2.2**). Another possibility may be that there is only one form of apo–enzyme and binding of a

Scheme 2.2 A possible kinetic mechanism for the interconversion of two conformations of MR where the value of α may or may not be unity (Note: α is unity when $K_A^S = K_A^R$). M^{2+} depicts any metal activator and the coefficient α may vary depending on which metal ion is bound. This mechanism does not include an enzyme bound intermediate.

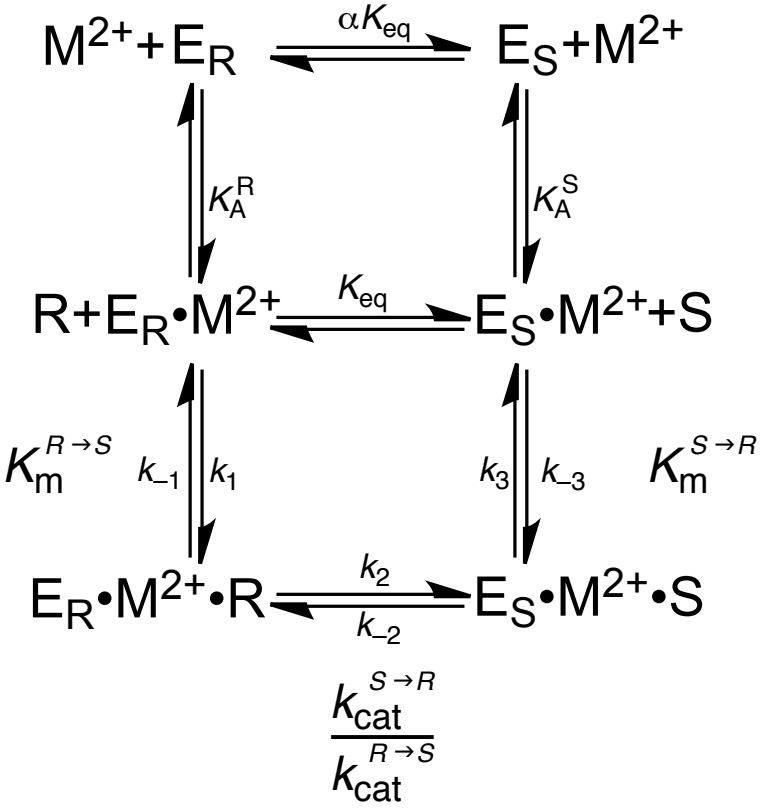

metal is what causes it to adopt one of the two conformations. In either case, the different metal ions affect the equilibrium to different degrees, with Mg^{2+} having the least, if any, affect on this equilibrium. Future studies including pH characterization of the different metalloenzymes, kinetic isotope effects, and NMR spectroscopy experiments to determine the p*K*a values of the catalytic residues, may provide insight into nature of this mechanism.

2.4.4 Conclusions

The kinetic results presented in this chapter shed light on the divalent metal cation requirement of MR for catalytic activity. In lieu of Mg^{2+}, the metal cations Mn^{2+}, Co^{2+} or Ni^{2+} can activate MR with similar efficiency. This choice of metal ion appears to depend on both the inherent electronegativity of the metal ion and its ability to form a stable octahedral complex when bound in the active site of MR. Binding of the metal ion does not change the secondary structure of MR, but alteration of metal ion activator does slightly alter the efficiency of MR to racemize the enantiomers of mandelate. There is a change in the ratio of the efficiencies, which may arise from a perturbation of the equilibrium between two possible iso–forms of MR. Although this chapter explores the effect of the metal ion on MR catalysis, it does not provide information on whether MR alters the inherent properties of the metal ions upon binding.

Chapter 3

Inhibition of MR by Intermediate Analogues Benzohydroxamate and Benzoylphosphonate

3.1 Introduction

Benzohydroxamate (BzH) and benzoylphosphonate (BzP) (**Scheme 1.4**) are known competitive inhibitors of MR with reported K_i values of 9.3 ± 2.5 μM and 300 ± 60 μM respectively (St. Maurice and Bearne, 2000). The X–ray crystal structure of BzH–bound to wild–type MR shows BzH coordinating the MR bound Mg^{2+} ion in a bi-dentate fashion, completing the octahedral coordination of the Mg^{2+} (**Figure 3.1**) (Lietzan *et al*., 2012). The five–member metal–chelate ring that BzH forms is planar with the phenyl ring of BzH, has little distortion, and is predicted to mimic the interaction of the enolate intermediate with the Mg^{2+} ion (Bourque *et al*. 2007; Lietzan *et al*., 2012). The linear free energy relationship between the log K_m/k_{cat} values for MR variants versus the corresponding log K_i values for inhibition of these variants by BzH is linear, with a slope of 1 (Lietzan *et al*, 2012), suggesting that BzH is a good mimic of the transition state or high–energy intermediate (Mader and Bartlett, 1997; Snider *et al*., 2004). Because BzH is a good mimic of the intermediate, a linear free energy relationship between the log K_m/k_{cat} values for each metal ion–bound variant of MR and its corresponding log K_i value for BzH is expected to provide insight into the role of the metal ion in MR stabilization of the transition state formed during mandelate racemase catalysis.

To date, there are no crystal structures of BzP (or any phosphonate containing compound) bound to MR; however, BzP is also a presumed analogue of the enolate intermediate, albeit a less effective one (St. Maurice and Bearne, 2000). Inhibition (IC_{50}) studies of the metal-bound variants of MR by BzP were conducted to determine if the

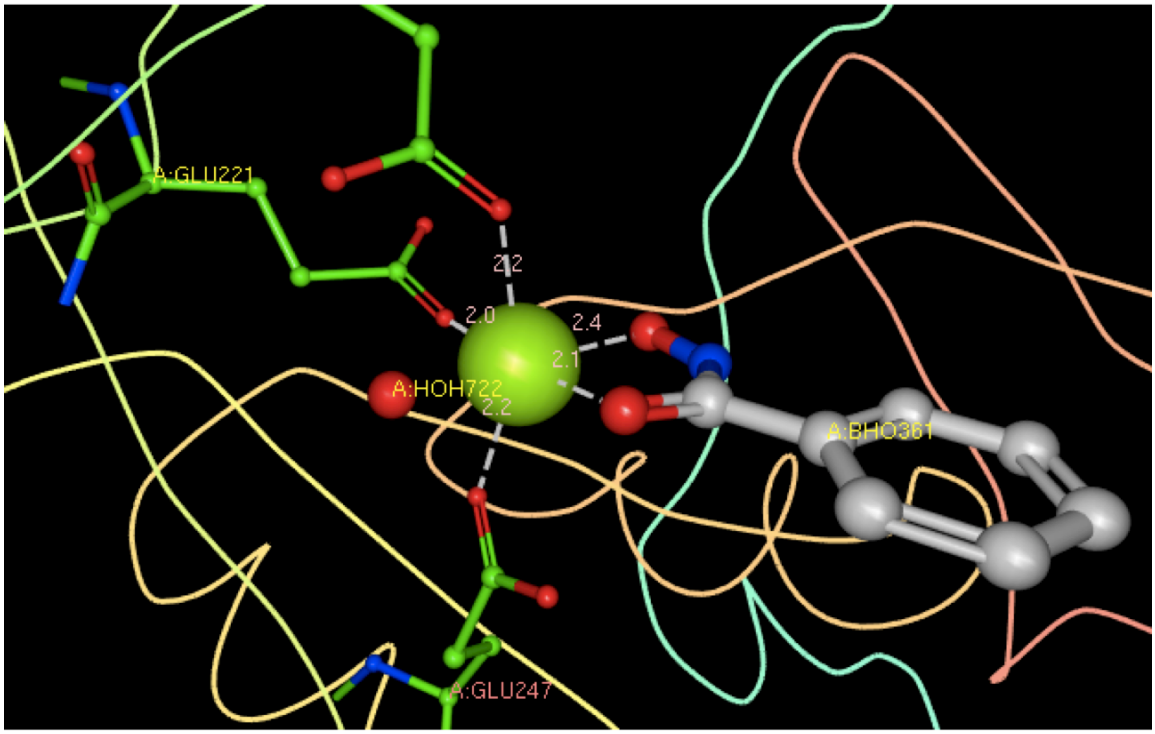

Figure 3.1 X–ray crystal structure of BzH chelating Mg^{2+} at the active site of WTMR [PDB = 3UXK (Leitzan *et al*., 2012)]. Mg^{2+} is shown octahedrally coordinated to the active site residues Glu 247, Glu 221, and Asp 195, one water molecule, and chelated in a bidentate orientation with the intermediate analogue BzH. The 5–member ring formed between BzH and the metal ion is undistorted and planar with the phenyl ring. Distances shown are in Å.

interaction between the ligand and metal ion in the active site of MR is predominantly charge related. Unlike BzH, BzP is a di–anionic compound at the assay pH (pK_{a1} = 0.77, pK_{a2} = 5.42; St. Maurice *et al*, 2003); therefore, if the role of the metal ion is merely to provide a positive charge, for either transition state stabilization or substrate orientation, then the variance in binding affinity for BzP among the different metalloenzymes will be more pronounced in the case of BzP than for BzH. If the binding affinity for BzP remains unchanged amongst the metal–bound variants of MR, then we could presume that either the inherent charge of the metal ions plays little role in ligand binding or the enzyme has altered the inherent properties of the metal ions, imparting on the metal ions so that they are insensitive to the enhanced charge on ligands.

In addition to reporting inhibition by BzH and BzP, this chapter also describes isothermal titration calorimetry (ITC) experiments designed to measure the stability constants (K_1 and K_2) associated with complex formation between the metals Mg^{2+}, Mn^{2+}, Co^{2+}, Ni^{2+} and BzH, and between BzP and Ni^{2+}. Although the stability constants for BzH chelation have been determined previously by a number of research groups using potentiometry (Garcia *et al*., 2005; Agrawal and Tandon, 1972; Parekh *et al*., 1989; Farkas *et al*., 2000), the stability constants from the literature all vary significantly from one another and none were directly applicable to our assay conditions (100 mM HEPES, pH 7.5, 25 ˚C). For this reason, ITC was conducted to determine more accurate stability constants under assay conditions, which could than be used to correct the free concentration of BzH and BzP during inhibition studies with MR.

In the previous chapter, we have seen that altering the metal ion has only a slight, but still significant, effect on k_{cat}/K_m. In this chapter, one of the main focal points will be determining the affinity of each metalloenzyme for BzH to help delineate the role of the metal ion in catalysis. In addition to outlining the inhibition and ITC studies, this chapter will also provide novel insight into the apparent effect that MR has on the bound metal ion. By drawing comparisons from the BzH inhibition and the ITC studies in this chapter, I will introduce the concept of 'the Hephaestus effect' (named after the Greek god of metalworking and blacksmithing), describing the ability of a protein to alter the properties of a metal ion.

3.2 Materials and Methods

3.2.1 General

AG 50W–X8 cation–exchange resin was purchased from BioRad Laboratories (Mississauga, ON). (*R*)– and (*S*)–mandelic acid, benzohydroxamic acid, $MgCl_2$, $MnCl_2 \bullet 4H_2O$, $CoCl_2 \bullet 6H_2O$, $NiCl_2$ and all other chemicals, unless otherwise stated, were reagent grade or better and purchased from Sigma–Aldrich Canada, Ltd. (Oakville, ON). Circular dichroism (CD) assays were conducted using a JASCO J–810 spectropolarimeter. Isothermal titration calorimetry (ITC) studies were conducted on a VP–ITC MicroCalorimeter from GE Healthcare (Formerly MicroCal, LLC, Northhampton, MA). ITC data analysis was conducted using Origin® software v. 7.0 from the Origin Lab (Northhampton, MA). Nuclear magnetic resonance (NMR) spectroscopy experiments were conducted using the Bruker AV 500 MHz spectrometer at the Nuclear Magnetic Resonance Research Resource Center (NMR^3) at Dalhousie University (Halifax, NS).

3.2.2 Synthesis of Benzoylphosphonate

Dimethyl benzoylphosphonate was prepared by reaction of trimethyl phosphite with benzoyl chloride as described previously (Kluger and Chin, 1978; St. Maurice and Bearne, 2000). Dimethyl benzoylphosphonate (1.5 mL, 6.9 mmol) was then dissolved in dry dichloromethane (5 mL) and demethylated by treatment with trimethylsilybromide (7,7 mL, 55.2 mmol, 8 equiv.) as previously described by Tulsi *et al*. (2010). The reaction was stirred for 20 h at room temperature under argon. The solvent was then evaporated, MeOH (5 mL) was added, and the solution stirred for 1 h. The MeOH was then evaporated and the crude product was dissolved in water, filtered, and the free acid was converted to the sodium salt by passing it through an AG 50W-X8 (Na^+ form) column. Fractions containing phosphonate were collected and lyophilized yielding an off–white powder: mp >300 °C; ^{1}H NMR δ (500 MHz; D_2O, ppm) 7.45 (Aryl H, M); ^{31}P NMR δ (202 MHz; D_2O) 0.37 (s, 1H decoupled) (St. Maurice and Bearne, 2000). The ^{31}P NMR spectrum is referenced to the deuterium lock signal calibrated to H_3PO_4 (85 %)as an external standard.

3.2.3 MR Assays

MR activity was assayed using the CD–based assay described earlier (Sharp *et al*., 1979). All inhibition assays with BzH and BzP were conducted at 25 ˚C in HEPES buffer (0.1 M, pH 7.5) containing one of the following metal ions: $MgCl_2$ (3.9 mM), $MnCl_2$•$4H_2O$ (0.4 mM), $CoCl_2$•$6H_2O$ (0.5 mM), or $NiCl_2$ (0.9 mM). Apo–enzyme was either incubated with metal ion for 30 min, or dialyzed against the respective assay buffer prior to inhibition studies to ensure active site saturation of the activating metal ion prior to activity assay. All reactions were initiated by addition of the enzyme to the solution.

Both IC_{50} studies for BzP, and inhibition assays for BzH, were conducted with final enzyme concentrations of 0.15, 0.20, 0.20, and 1.05 μg/mL for Mg^{2+}–, Co^{2+}–, Ni^{2+}–, and Mn^{2+}–bound MR, respectively, and contained BSA (0.05%).

The concentrations of free BzH ($[I]_{free}$, uncorrected) used for inhibition assays were 10, 20, and 30 μM, for Mg^{2+}–bound MR, 15, 30, and 45 μM, for Co^{2+}– and Mn^{2+}–bound MR, and 60, 120, and 180 μM for Ni^{2+}–bound MR. Concentrations of (*R*)–mandelate used for BzH inhibition studies were between 0.5 and 12 mM. The concentrations of (*R*)–mandelate used in the IC_{50} assays for inhibition by BzP were 1 mM, 1.24 mM, 1.1 mM, and 1 mM for Mg^{2+}–, Mn^{2+}–, Co^{2+}–, and Ni^{2+}–bound MR, respectively. The concentrations of free BzP used were 50–400 μM and the path–length was changed to 5 mm to increase the signal–to–noise ratio.

3.2.4 MR Assay Data Analysis

For inhibition studies with BzH, the values of V_{max} and K_m were determined by fitting equation 2.5 to the initial velocity (v_i) data as a function of substrate concentration [S] using nonlinear regression analysis and the program *KaleidaGraph* v. 4.0 from Synergy Software (Reading, PA). Values of $1/v_i$ and 1/[S] were plotted using a double–reciprocal plot (Lineweaver–Burk) to qualitatively determine the mechanism of inhibition of the metal ion variants of MR by BzH. Upon determination that BzH was a competitive inhibitor, equation 3.1 was used to fit initial velocity data from inhibition experiments to obtain K_i values.

$$v_i = \frac{V_{max}[S]}{K_m\left(1 + \frac{[I]}{K_i}\right) + [S]} \qquad 3.1$$

The IC_{50} values for inhibition by BzP were determined by fitting equation 3.2 to

the ratio v_i/v_0 as a function of [I] where the IC_{50} is the concentration of BzP ([I]) that yields $v_i/v_0 = 0.5$.

$$\frac{v_i}{v_o} = \frac{IC_{50}^n}{IC_{50}^n + [I]^n} \qquad 3.2$$

All kinetic parameters were determined in triplicate and average values are reported, with the reported errors being standard deviations. Protein concentrations were determined by measuring the absorbance at 280 nm using the molar extinction coefficient of 53, 400 $M^{-1}cm^{-1}$ (calculated using ProtParam tool available on the ExPASy server: http://web.expasy.org/protparam (Gasteiger *et al*., 2005)). The k_{cat} values were calculated by dividing V_{max} values by total enzyme concentrations ($[E]_t$) using an MW value of 41, 264.

3.2.5 Isothermal Titration Calorimetry

Isothermal titration calorimetry (ITC) experiments were conducted on a VP–ITC MicroCalorimeter at 25 °C in HEPES buffer (0.1 M, pH 7.5). All samples were vacuum degassed (10 min) and filtered prior to commencing ITC experiements. For the titration of BzH with metal ion, the sample cell (initial volume of 1.4166 mL) containing BzH (0.5 mM) was titrated with metal ion (20 mM for Ni^{2+}, Co^{2+}, and Mn^{2+}, and 40 mM for Mg^{2+}) with either 60 × 5 μL injections, or, 30 × 10 μL injections, over a period of 20 s per injection, 240 s apart, with a stir speed of 300 s^{-1}, and feedback mode set to high. The reference cell was filled with degassed, filtered, distilled, de–ionized water with the differential power set to 25 μcal/s.

For the titration of the metal ion with BzH, the sample cell containing metal ion (1 mM, initial volume of 1.4166 mL) was titrated with BzH (20 mM, 30 × 10 μL injections,

over a period of 20 s per injection, with 240 s between injections); all other parameters remained the same as mentioned above. For the titration of BzP with Ni^{2+}, the sample cell containing BzP (5 mM) was titrated with Ni^{2+} (80 mM, 20 × 10 μL injections over 20 s, 240 s apart). For all ITC experiments, the initial injection of 2 μL was discarded from the data set prior to analysis. The heat of dilution was determined by replicating the experiment with only buffer in either the sample cell, or syringe, and metal ion or ligand in the other; and was subtracted from the data prior to analysis. All ITC experiments were conducted in at least triplicate.

3.2.6 Isothermal Titration Calorimetry Data Analysis

Raw calorimetric data were analyzed using Origin® scientific plotting software v. 7.0. Equation 3.3 was used to fit the ITC data for complex formation of both BzP and Ni^{2+}, and BzH and Mg^{2+} to the single site model,

$$K_1 = \frac{[ML]}{[M^{2+}][L]} \tag{3.3}$$

where [L] is BzH or BzP and $[M^{2+}]$ is the metal ion. The value of K was determined using equation 3.4,

$$K = \frac{\Theta}{(1 - \Theta)[X]} \tag{3.4}$$

where Θ is the fraction of the sites of the molecule in the sample cell that are occupied by ligand X, and [X] is concentration of free molecule titrated into the cell (either BzP, BzH, or metal ion), which is determined using equation 3.5.

$$[X]_t = [X] + n\Theta[M]_t \tag{3.5}$$

In equation 3.5, $[X]_t$ is the total concentration of titrating ligand, $[M]_t$ is the bulk concentration of the molecule in the cell and n is the number of sites, also known as the stoichiometry. $[M]_t$ and n are determined using equation 3.6,

$$Q = n\Theta[M]_t\Delta H V_o \tag{3.6}$$

where Q is the total heat content of the solution, V_o is the active cell volume, and ΔH is the molar heat of the molecules interacting (enthalpy). Q is calculated at the end of every i^{th} injection and designated $Q(i)$. The change in heat $\Delta Q(i)$ for each injection (i) is found by fitting equation 3.7 to the experimental data,

$$\Delta Q(i) = Q(i) + \frac{dV_i}{V_o}\left[\frac{Q(i) + Q(i-1)}{2}\right] - Q(i-1) \tag{3.7}$$

where V_i is the volume of the injection.

The ITC data for complex formation of BzH with either Mn^{2+}, Ni^{2+}, or Co^{2+} were fit to the sequential binding model, which, in addition to equation 3.3, includes equation 3.8.

$$K_2 = \frac{[ML_2]}{[ML][L]} \tag{3.8}$$

Equation 3.7 was fit to the experimental data, using the sequential model, where Q is determined by equation 3.9,

$$Q = [M]_t V_o(F_1\Delta H_1 + F_2[\Delta H_1 + \Delta H_2]) \tag{3.9}$$

where F_1 and F_2 are determined by equations 3.10 and 3.11, respectively.

$$F_1 = \frac{K_1[X]}{1 + K_1[X] + K_1K_2[X]^2} \tag{3.10}$$

$$F_2 = \frac{K_1 K_2 [X]^2}{1 + K_1[X] + K_1 K_2 [X]^2} \qquad 3.11$$

3.2.7 Correcting the Free Inhibitor Concentration

To account for the reduction in the free inhibitor concentration due to complex formation with metal ion, the concentrations of free BzH and BzP used in inhibition assays were corrected using equation 3.12.

$$[I]_{total} = [I]_{free} + [MI] + [MI_2] + [EI] \qquad 3.12$$

The term [EI] can be neglected since $[I]_{total}$ >>[E]. Using equations 3.3, 3.8, and 3.12 equation 3.13 can be derived.

$$0 = -[I]_{total} + [I]_{free}\left(1 + \frac{[M^{2+}]}{K_{-1}}\right) + [I]^2_{free}\left(\frac{[M^{2+}]}{K_{-1}K_{-2}}\right) \qquad 3.13$$

Using the quadratic equation, and equation 3.13, we can solve for $[I]_{free}$. The corrected concentrations of $[I]_{free}$ were used to plot the data for BzH–dependent inhibition of Mg^{2+}–, Mn^{2+}–, Co^{2+}–, and Ni^{2+}–bound MR, as well as the IC_{50} plots for BzP–dependent inhibition of Ni^{2+}–bound MR.

3.3 Results

3.3.1 ITC Studies

For both titration of the metal ion with BzH and BzH with the metal ion, the stoichiometry was always found to be 2:1 (BzH to metal ion). The exception to this was complex formation between BzH and Mg^{2+}, where a second binding event could not be detected. The titration of the metal ion with BzH had a much larger heat of dilution, and therefore a lower signal–to–noise ratio, than the titration of the BzH with metal ion. As a result of this observation, the titration of BzH with metal ion was determined to have

higher precision and the parameter, ΔH_1, ΔH_2, K_1, and K_2 were determined in triplicate using those titrations (**Table 3.1**). The first association constants (K_1) closely follows the Irving–Williams series for complex stability, where the stability of the complex formed by the metal ion and the ligand increases in the order $Mg^{2+} < Mn^{2+} < Co^{2+} < Ni^{2+}$ (Irving and Williams, 1953). The second association constant (K_2) does not follow the same trend; instead Co^{2+} has the greatest K_2 followed by Ni^{2+} and then Mn^{2+}; a second association constant was not observed for Mg^{2+}. Representative plots for complex formation between BzH and each of the metal ions are included in **Figure 3.2**.

The result of the ITC studies involving Ni^{2+} and BzP is included with the BzH data in **Table 3.1**. The representative plot for BzP and Ni^{2+} complex formation is shown in **Figure 3.3**. The K_1 for BzP and Ni^{2+} association was small, but measurable, and only one binding event was observed with a stoichiometry of 1:1. One notable observation is that the ΔH of binding was endothermic for BzP–Ni^{2+} complex formation, as was the enthalpy change for BzH–Mg^{2+} complex formation. All other metal–ion/BzH interactions were exothermic.

Because the enthalpy (ΔH) measured during ITC experiments corresponds to the change in heat of the system as a whole, it is an amalgamation of many events accompanying metal ion BzH complex formation, including, but not limited to, the dehydration of the metal ion, the possible deprotonation of BzH upon coordination to metal ion, and HEPES buffer scavenging protons that dissociate from BzH (Khalil and Fazary, 2004; Quinn, 2010). As a result, the entropy (ΔS) calculated for the interaction also reflects many processes, occurring simultaneously, that accompany chelation of metal ion by BzH.

Table 3.1 Thermodynamic parameters determined using ITC for complex formation between BzH and metal ions and BzP and Ni^{2+} (0.1 M HEPES, pH 7.5, 25 ˚C).[a]

benzohydroxamate (BzH)						
Metal–ion	K_1 **(M^{-1})**	K_2 **(M^{-1})**	ΔH_1 **(cal/mol)**	ΔS_1 **(cal/mol/K)**	ΔH_2 **(cal/mol)**	ΔS_2 **(cal/mol/K)**
Ni^{2+}	1.5 (± 0.4) × 10^4	842 (± 101)	–1.3 (± 0.1) × 10^3	14.8 (± 0.6)	–1.8 (± 0.2) × 10^3	7.2 (± 0.8)
Co^{2+}	2.1 (± 0.6) × 10^3	5.9 (± 0.5) × 10^3	–790 (± 90)	12.5 (± 0.4)	–1.46 (± 0.08) × 10^3	12.3 (± 0.1)
Mn^{2+}	206 (± 35)	68 (± 13)	–186 (± 2)	9.9 (± 0.3)	–150 (± 46)	7.8 (± 0.6)
Mg^{2+}	83 (± 6)	–	296 (± 5)	9.7 (± 0.1)	–	–
benzoylphosphonate (BzP)						
Metal–ion	K_1 **(M^{-1})**	K_2 **(M^{-1})**	ΔH_1 **(cal/mol)**	ΔS_1 **(cal/mol/K)**	ΔH_2 **(kcal/mol)**	ΔS_2 **(cal/mol/K)**
Ni^{2+}	515 (± 10)	–	1.75 (± 0.06) × 10^3	18.3 (± 0.3)	–	–

[a]Values are means of at least 3 trials and reported errors are standard deviations.

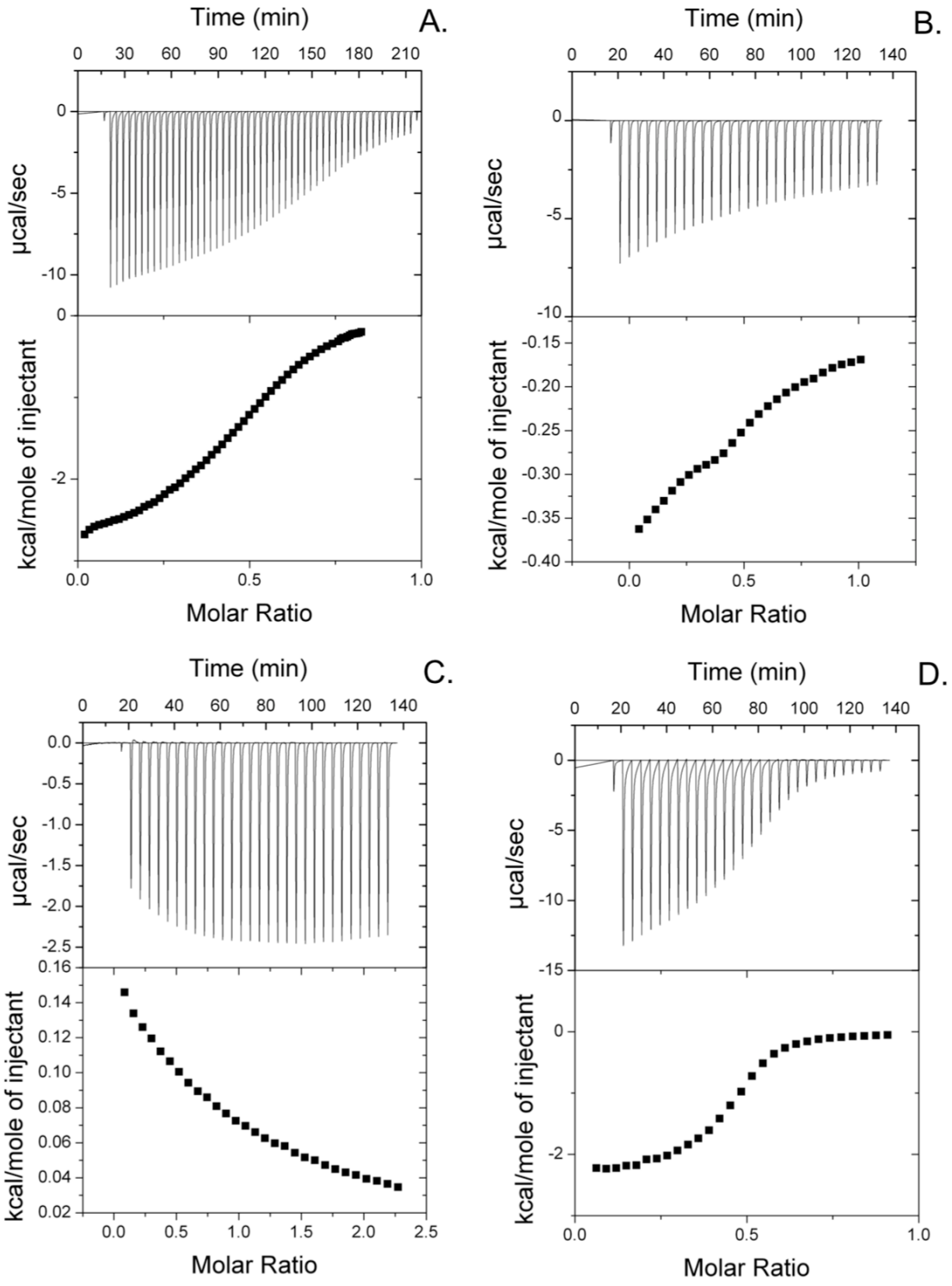

Figure 3.2 Representative plots of raw ITC data for titration of BzH with Ni^{2+}(A), Mn^{2+}(B), Mg^{2+}(C), and Co^{2+}(D). Titrations were carried out at 25 °C in HEPES buffer (0.1M, pH 7.5) with 5 mM BzH in the sample cell and 20 mM of Ni^{2+} (A), Mn^{2+} (B), and Co^{2+} (D), or 40 mM Mg^{2+} (C) in the syringe.

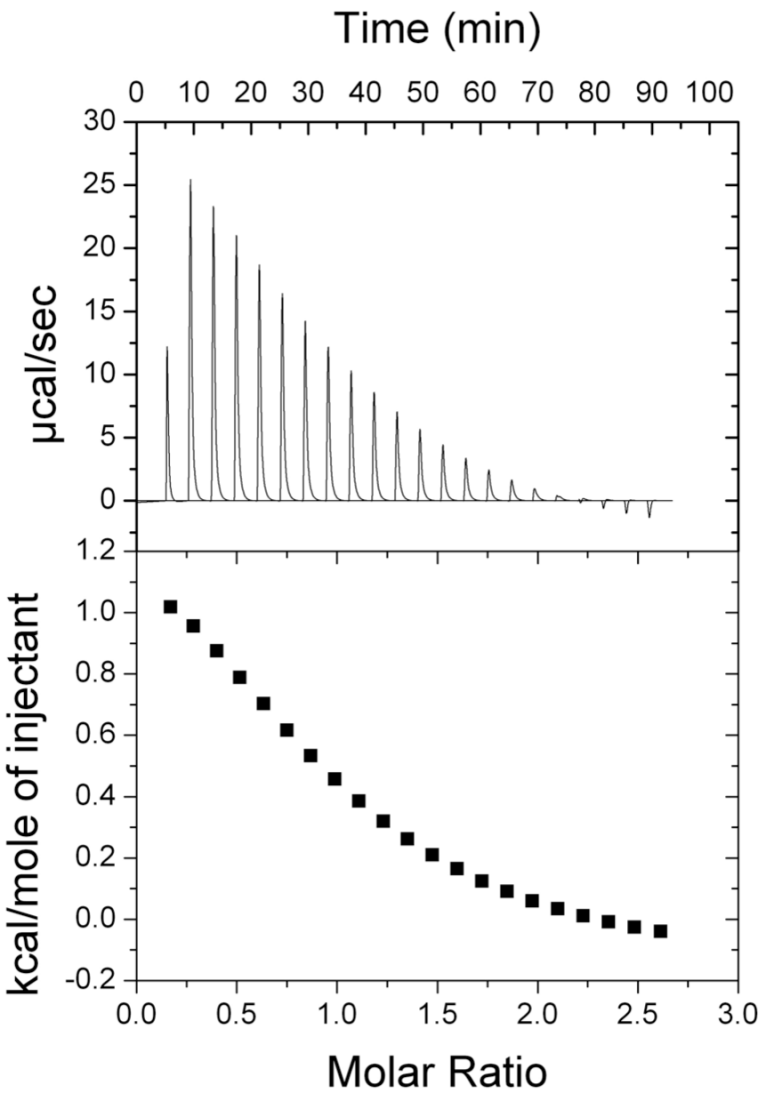

Figure 3.3 Representative plot of raw ITC data for titration of BzP with Ni^{2+}. Titrations were carried out at 25 ˚C in HEPES buffer (0.1M, pH 7.5) with 5 mM BzH in the sample cell and 80 mM Ni^{2+} in the syringe.

3.3.2 Competitive Inhibition of Metal–Bound Variants of MR by BzH

BzH was determined to be a classical competitive inhibitor for each metal ion–bound MR. Values of K_i were determined by taking the negative x–intercept from the replot of the K_m/V_{max} (determined from nonlinear regression analysis) versus concentration of inhibitor (**Figures 3.4–3.7**). The corrected (determined from plots using $[I]_{free}$, **section 3.2.6**) and uncorrected (determined using $[I]_{total}$) inhibition constants (K_i) for BzH and each metal ion–bound variant of MR are shown in **Table 3.2**. The uncorrected K_i values of BzH were relatively the same (~15 μM) for Mg^{2+}–, Mn^{2+}–, and Co^{2+}–bound MR. The uncorrected K_i value of BzH for Ni^{2+}–bound MR was nearly 3–fold higher (40 μM).

The corrected K_i values for metal–bound variants of MR had a greater variance and followed the order $Mg^{2+} \approx Mn^{2+} > Co^{2+} > Ni^{2+}$, indicating that Ni^{2+}–bound MR had a greater affinity for BzH than did the other metal ion variants. Although the difference between the binding affinities is slight (< 1 order of magnitude), the order of their stabilities follows the Irving–Williams series (Irving and Williams, 1953).

3.3.3 Inhibition of Metal Ion–Bound Variants of MR by BzP

The IC_{50} values for inhibition of the metal ion–bound variants of MR by BzP followed the pattern $Mg^{2+} \approx Mn^{2+} < Co^{2+} < Ni^{2+}$, and are listed in **Table 3.2**. The observed trend is essentially the opposite of that observed for BzH binding to the metal ion–variants. BzP is a weaker inhibitor of Ni^{2+}–bound MR, relative to other metal–bound MR variants, although the difference is slight (< 3–fold). Representative IC_{50} plots are shown in **Figure 3.8**. Since only free Ni^{2+} and BzH were observed to from a complex (**section**

Table 3.2 Corrected and uncorrected inhibition constants (K_i) and IC_{50} values for the inhibitors BzH and BzP with each of the metal ion–bound variants of MR.[a]

	benzohydroxamate		benzoylphosphonate
MR variant	**uncorrected K_i (μM)**	**corrected K_i (μM)**	**IC_{50} (μM)**
Ni^{2+}	40 (± 2)	2.7 (± 0.1)	428 (± 16)[b]
Co^{2+}	15.7 (± 0.7)	7.1 (± 0.3)	308 (± 24)
Mn^{2+}	15 (± 1)	13 (± 2)	193 (± 13)
Mg^{2+}	15.0 (± 0.3)	11.3 ± (0.2)	202 (± 7)

[a]Values are means of at least 3 trials and reported errors are standard deviations.
[b]Estimated by extrapolation.

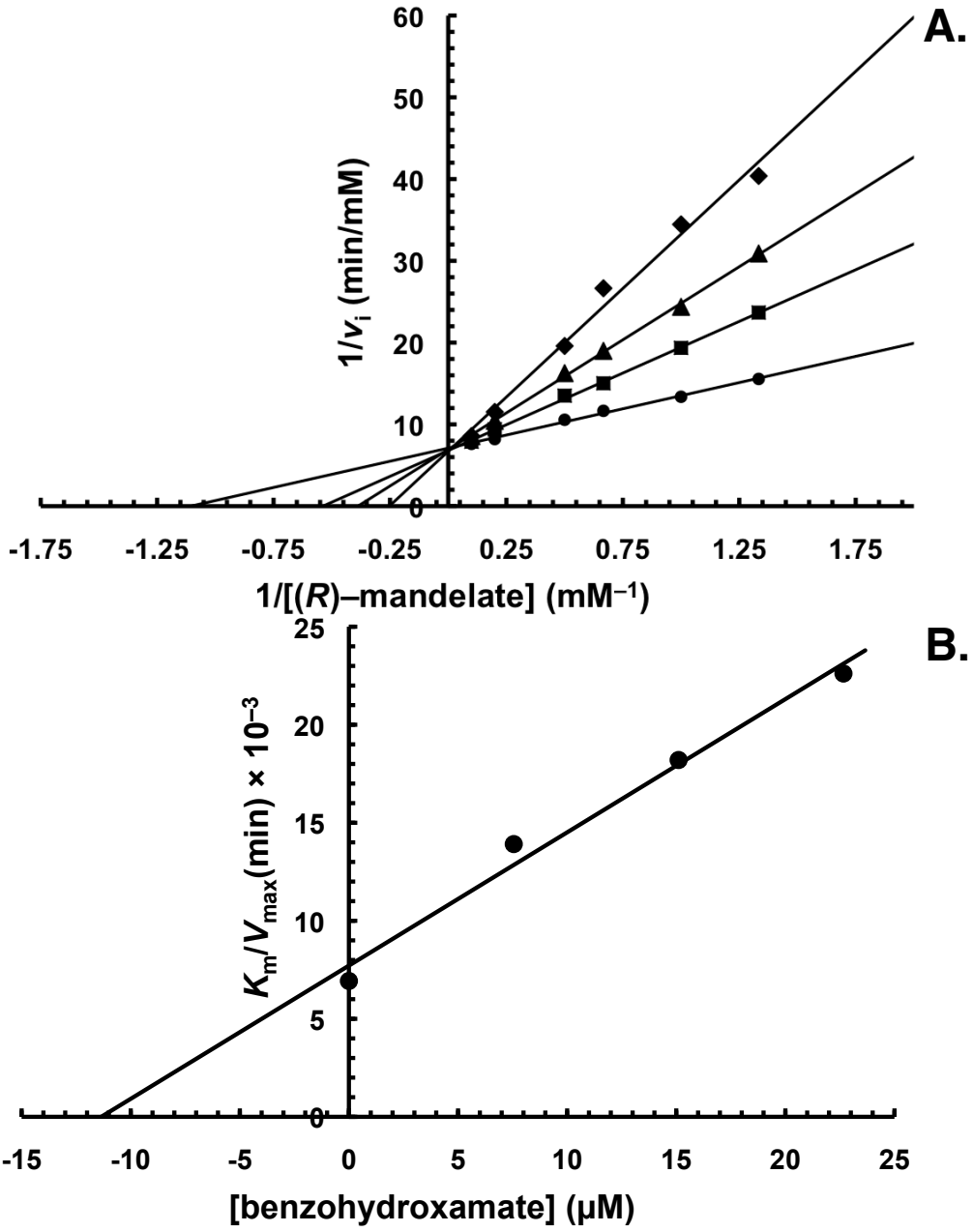

Figure 3.4 A representative double reciprocal plot for the competitive inhibition of Mg^{2+}–bound MR by BzH (A) and replot of $(K_m/V_{max})^{app}$ as a function of free benzohydroxamate concentrations (B). (**A**) Initial concentrations of (*R*)–mandelate ranged between values of 0.75 mM and 10 mM. Concentrations of total BzH used were 0 μM (●), 10 μM (■) , 20 μM (▲), and 30 μM(◆). Assay conditions were as described in section 3.2.3. **(B)** Plot of $(K_m/V_{max})^{app}$ (determined from nonlinear regression analysis) as a function of free benzohydroxamate concentrations ($[I]_{free}$ = 7.5, 15.1, 22.6 μM determined by the method described in **section 3.2.6.** The K_i value determined from these plots is 11.3 ± (0.2) μM.

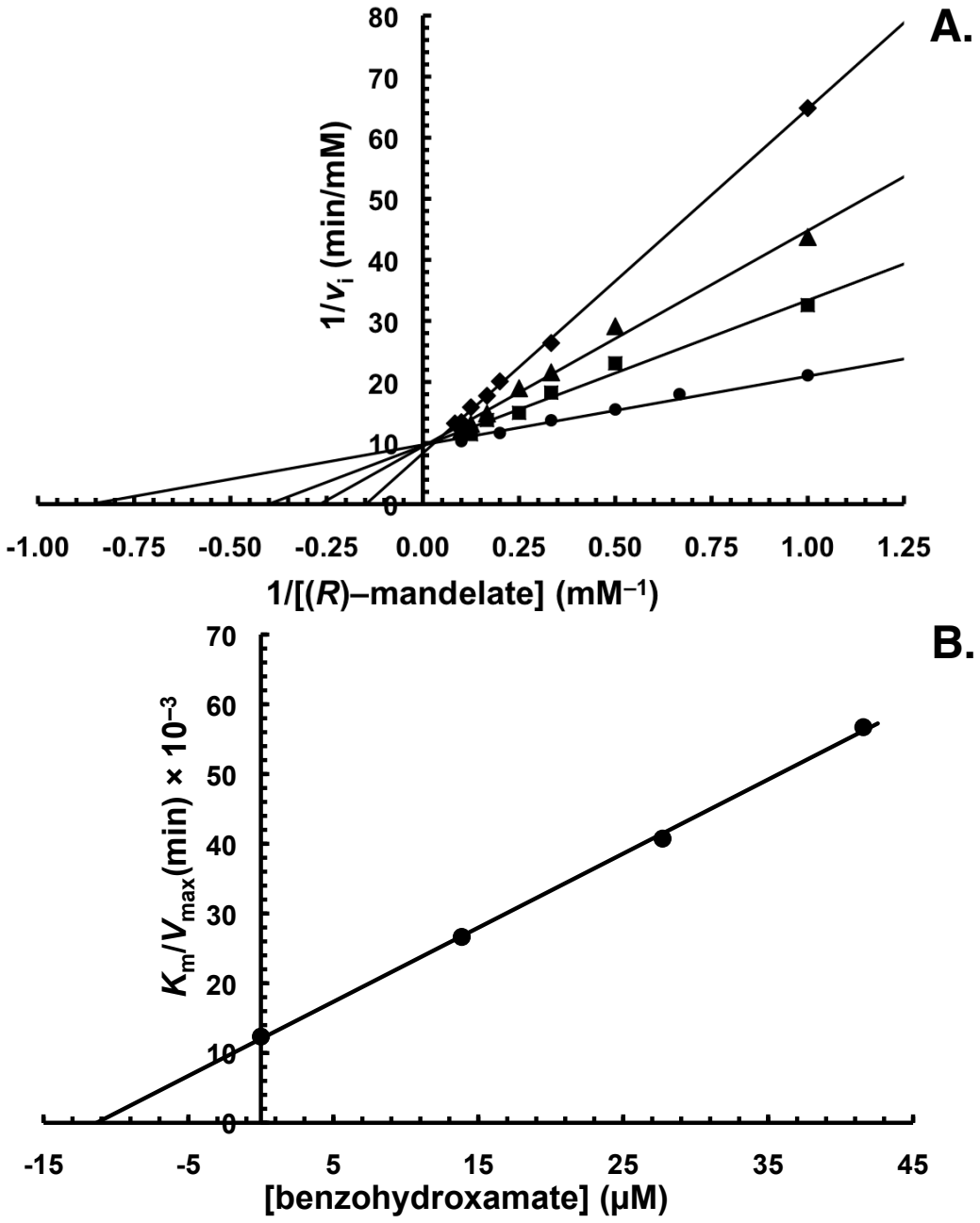

Figure 3.5 A representative double reciprocal plot for the competitive inhibition of Mn^{2+}–bound MR by BzH and replot of $(K_m/V_{max})^{app}$ as a function of free benzohydroxamate concentrations (B). (A) Initial concentrations of (*R*)–mandelate ranged between values of 1 mM and 10 mM. Concentrations of total BzH used were 0 μM (●), 15 μM (■) , 30 μM (▲), and 45 μM(◆). Assay conditions were as described in section 3.2.3. **(B)** Plot of $(K_m/V_{max})^{app}$ (determined from nonlinear regression analysis) as a function of free benzohydroxamate concentrations ($[I]_{free}$ = 13.8, 27.7, 41.5 μM determined by the method described in **section 3.2.6**. The K_i value determined from these plot is 13 (± 2) μM.

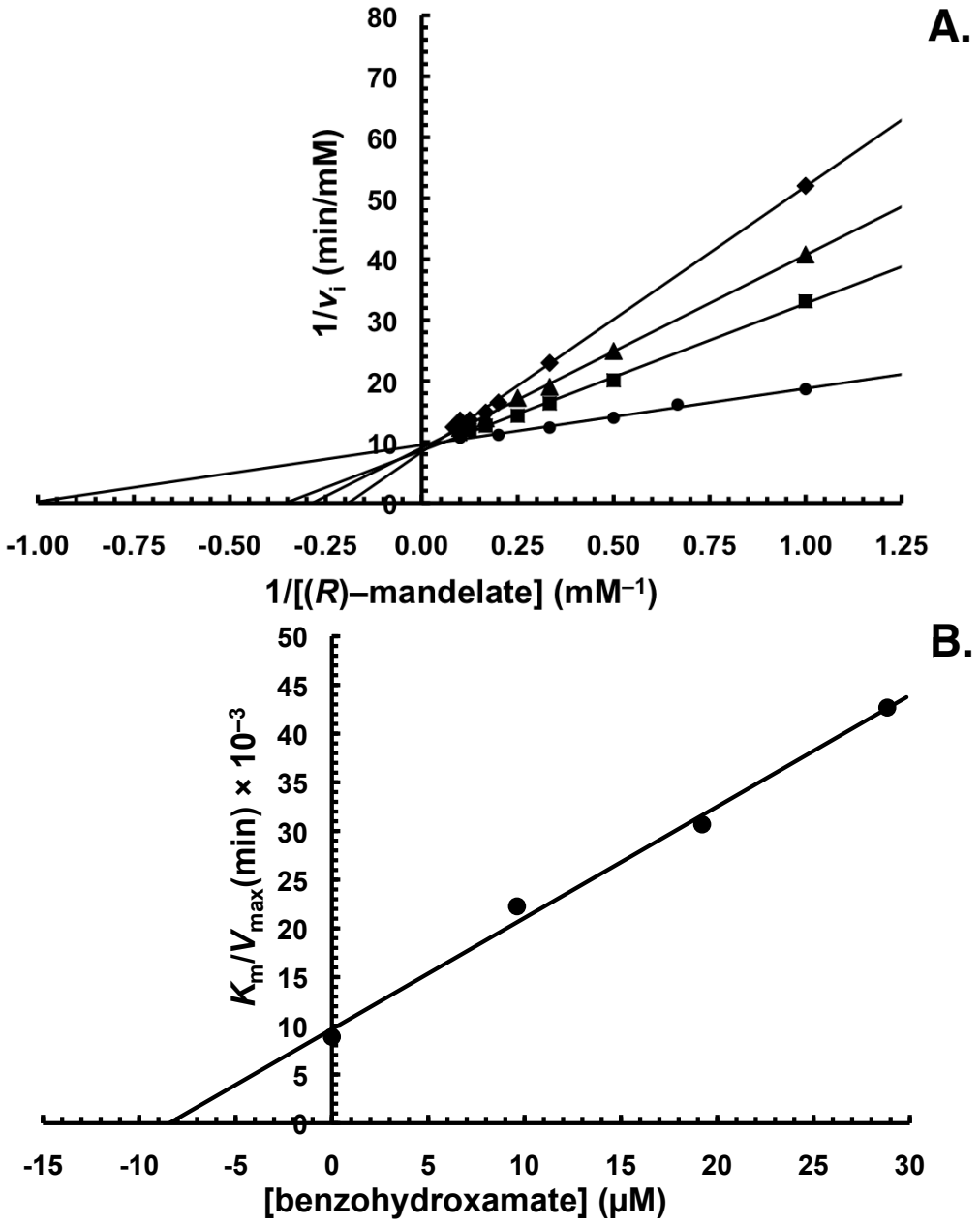

Figure 3.6 A representative double reciprocal plot for the competitive inhibition of Co^{2+}–bound MR by BzH and replot of $(K_m/V_{max})^{app}$ as a function of free benzohydroxamate concentrations. (A) Initial concentrations of (*R*)–mandelate ranged between values of 1 mM and 10 mM. Concentrations of total BzH used were 0 μM (●), 15 μM (■), 30 μM (▲), and 45 μM(◆). Assay conditions were as described in section 3.2.3. **(B)** Plot of $(K_m/V_{max})^{app}$ (determined from nonlinear regression analysis) as a function of free benzohydroxamate concentrations ($[I]_{free}$ = 9.6, 19.2, 28.8 μM determined by the method described in **section 3.2.6**. The K_i value determined from these plots is 7.1 (± 0.3) μM.

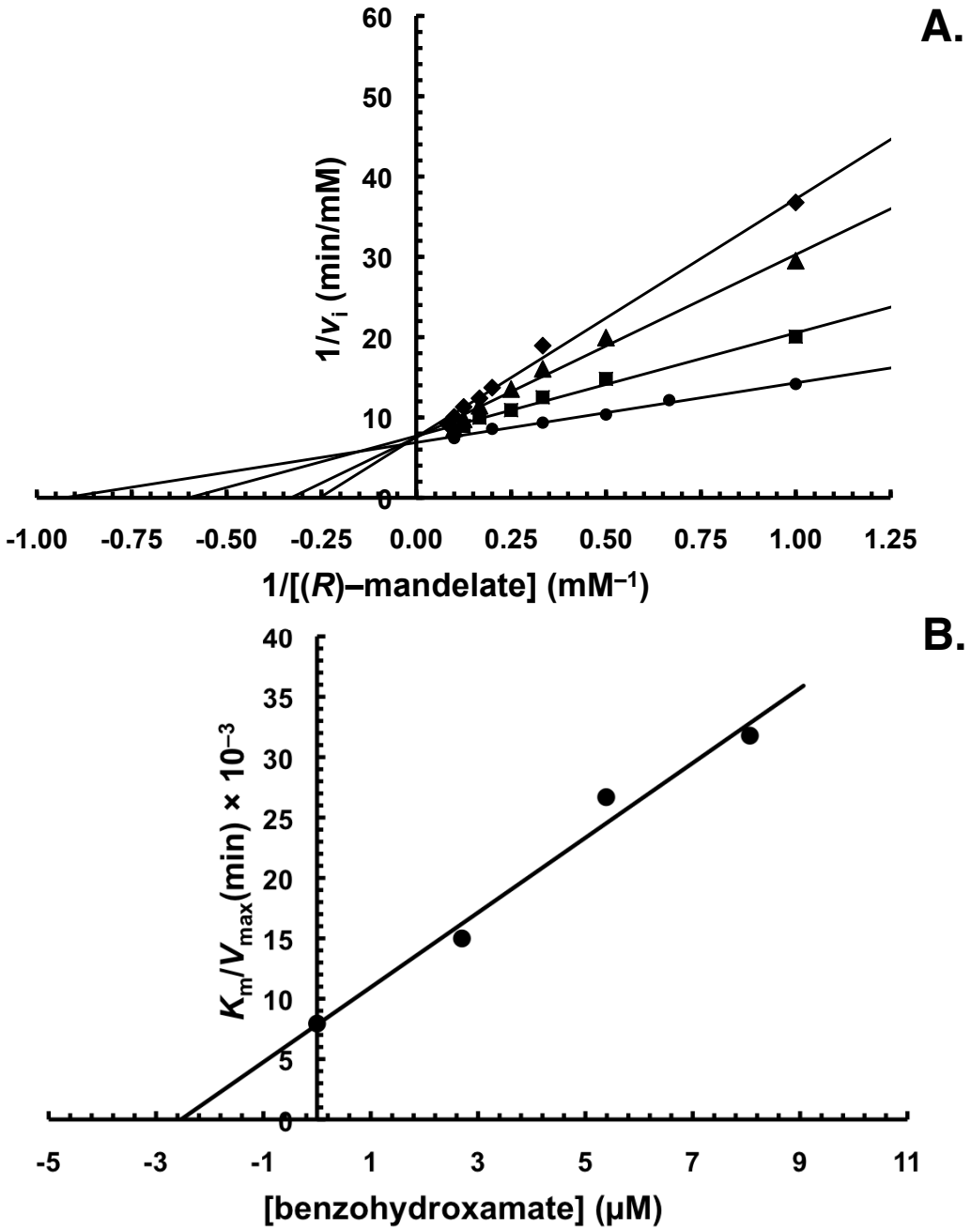

Figure 3.7 A representative double reciprocal plot for the competitive inhibition of Ni^{2+}–bound MR by BzH and replot of $(K_m/V_{max})^{app}$ as a function of free benzohydroxamate concentrations. (A) Initial concentrations of (*R*)–mandelate ranged between values of 1 mM and 12 mM. Concentrations of total BzH used were 0 μM (●), 40 μM (■), 80 μM (▲), and 120 μM(◆). Assay conditions were as described in section 3.2.3. **(B)** Plot of $(K_m/V_{max})^{app}$ (determined from nonlinear regression analysis) as a function of free benzohydroxamate concentrations ($[I]_{free}$ = 2.7, 5.4, and 8.1 μM) determined by the method described in **section 3.2.6**. The K_i value determined from these plots is 2.7 (± 0.1) μM.

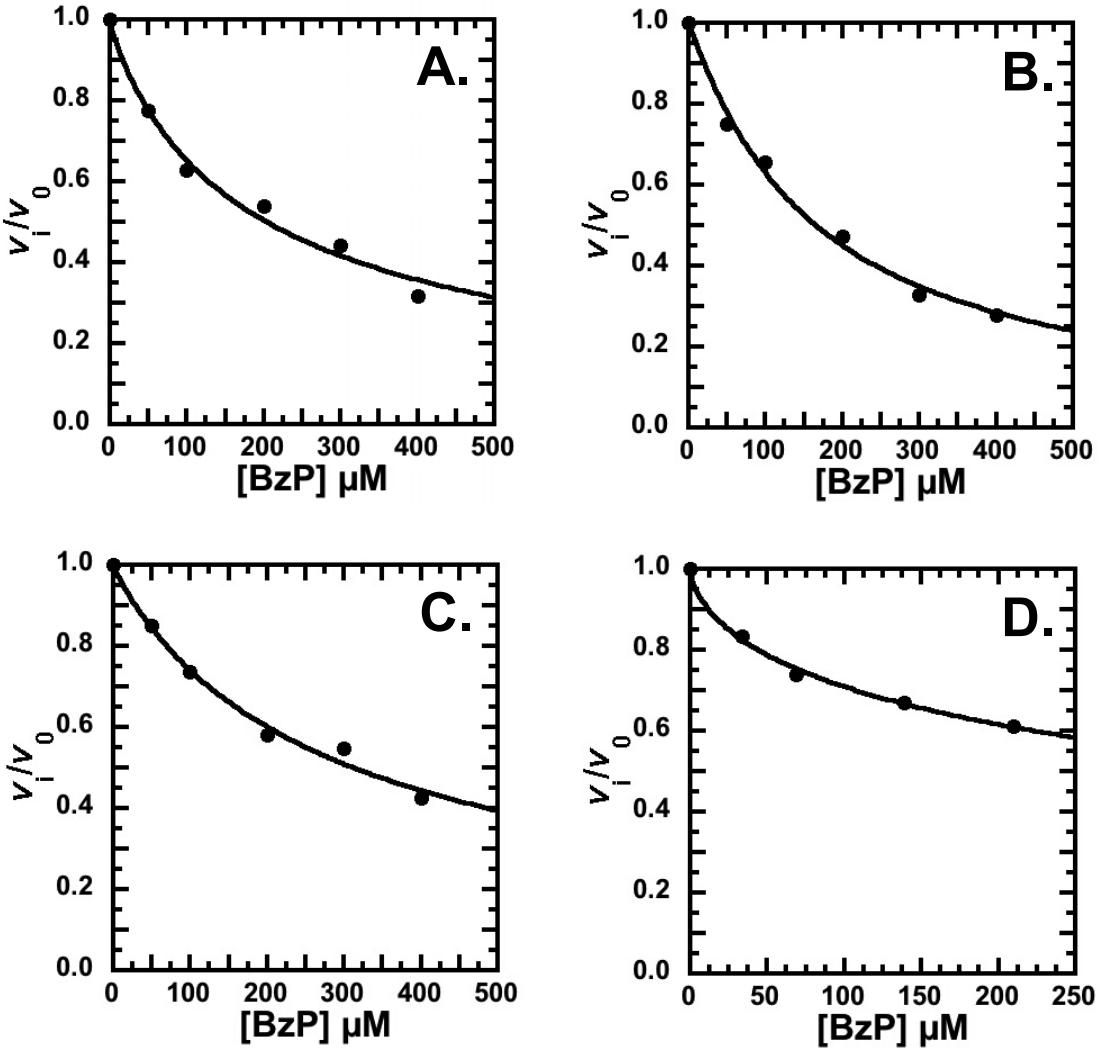

Figure 3.8 Representative IC_{50} plots for the inhibition of Mg^{2+}– (A), Mn^{2+}– (B), Co^{2+}– (C), and Ni^{2+}–bound (D) MR by BzP. Initial concentrations of (*R*)–mandelate were 1 mM, 1.24 mM, 1.1 mM, and 1 mM for Mg^{2+}– (A), Mn^{2+}– (B), Co^{2+}– (C), and Ni^{2+}–bound (D) MR, respectively. Concentrations of BzP used were 50–400 μM for Mg^{2+}–, Mn^{2+}– and Co^{2+}– bound MR. The concentrations of free BzH ($[I]_{free}$) used for the Ni^{2+}–bound MR IC_{50} were 34, 69, 139 and 210 μM which were determined by the method described (**section 3.2.6**) and the measured ITC values (**section 3.3.1**). From the plots, the IC_{50} values were determined to be 202 (± 7), 193 (± 13), 308 (± 24), and 428 (± 16) μM for Mg^{2+}–, Mn^{2+}–, Co^{2+}–, and Ni^{2+}–bound MR, respectively.

3.3.1) only the IC_{50} data for Ni^{2+} were re–plotted using corrected concentrations of free BzP (**section 3.2.6**).

Since BzP is a reported competitive inhibitor of MR (St. Maurice and Bearne, 2000), the K_i value can be estimated using the IC_{50} value and equation 3.14,

$$IC_{50} = K_i\left(1 + \frac{[S]}{K_s}\right) \qquad 3.14$$

assuming that BzP–dependent inhibition is competitive for all metal ion–bound variants of MR.

The highest concentration of BzP assayed was 400 μM due to the fact that at concentrations higher than this, even with a reduced path–length (0.5 mm), the voltage of the photomultiplier tube of the CD–spectropolarimeter was too high for accurate readings due to a low signal. The result is that the data points on the IC_{50} plot with greater concentrations of BzP are less accurate than the rest of the data, resulting in IC_{50} values with lower accuracy. This is especially noticeable in the case of Ni^{2+}, where the highest concentration of free BzP used was 300 μM, due to the increased voltage from the presence of Ni^{2+}. As a result, the inhibition of Ni^{2+}–bound MR never attains 50% and therefore the IC_{50} value must be obtained by extrapolation.

3.4 Discussion

One of my goals in this study was to determine if the binding of BzH to the metal ion variants of MR paralleled the change in the k_{cat}/K_m values of MR that was observed upon replacement of the metal ion activator. As the previous chapter shows, only four metal ions were found to activate MR and changing the metal ion activator does not significantly change the efficiency (k_{cat}/K_m) of MR. With only four activators, and very

little change to the efficiency of MR, construction of a linear free energy relationship between the log (K_m/k_{cat}) and log (K_i) values would not be particularly informative. This is in contrast to the more informative linear free energy relationship constructed previously using BzH and mutations of MR (Lietzan *et al*., 2012). A more useful analysis would be to compare the stability constant for complex formation of free BzH and metal ion in solution to the binding affinity of BzH for metal ions in the active site of MR. Such an analysis might reveal how MR alters the properties of bound metal ions.

3.4.1 BzH–Metal Ion Complex Formation in Aqueous Solution

According to the results of my ITC studies, and other studies, two molecules of BzH will chelate one molecule of Mn^{2+}, Co^{2+}, or Ni^{2+} in aqueous solution (Garcia *et al*., 2005; Agrawal and Tandon, 1972; Parekh *et al*., 1989; Farkas *et al*., 2000). In the case of Mg^{2+}, only a single weak binding event with BzH was observed. This finding is not surprising, since there are no other reports of a second binding constant for Mg^{2+} in the literature.

Density functional theory calculations, NMR spectroscopy, and stopped–flow kinetic experiments show that, in aqueous solution, BzH may assume a number of possible geometric isomers and protonation states (**Scheme 3.1**) (Exner *et al*., 1993; García *et al*. 2005), the most stable of which is predicted to be the *Z*–amide (García *et al*. 2005). In the present assay system (pH = 7.5), BzH is mostly in the protonated form, since the pK_a value is 8.8 (Exner *et al*., 1993; Farkas *et al*., 2000). It is not known whether the pK_a of 8.8 applies to either the N^- or the O^- acid of BzH; however, most studies conclude that the deprotonation of either group can occur to a similar extent and it has been proposed that a buffer–assisted proton migration from the O to N can occur,

especially in the *Z*–form (**Scheme 3.1)** (Exner *et al*., 1993; Farkas *et al*., 2000; García *et al*. 2005).

Even though the structures of the metal ion–BzH complexes formed are not discernable from the ITC data, a suggested model for complex formation is proposed in **Scheme 3.2**. This scheme suggests that the predicted conformation of BzH in aqueous solution, the *Z*–amide, will chelate the metal ion in a bidentate fashion. A ligand possessing two or more non–adjacent atoms that can co–ordinate a metal atom, is referred to as a chelate–ligand (Morgan and Drew, 1920). Complexes of this nature exhibit an enhanced thermodynamic and kinetic stability referred to as the chelate effect. The thermodynamic stability of any chelate–complex arises from an enthalpy gain due to coordinate bond formation, and a favourable increase in entropy resulting from the number of free ligands, in this case water, increasing due to displacement from the metal ion (Martel *et al*. 1995). The kinetic stabilization of a chelate–complex is a reflection of the low probability of complete dissociation, which is attributed to the formation of a metallacycle ring structure (Vallet *et al*., 2003). It stands to reason then that BzH will, most likely, form a 5–member, bidentate chelate with any metal ion as it will be thermodynamically and kinetically favourable.

The proposed second binding event is based on the finding that the ITC data fit best to a sequential binding model. It stands to reason that coordinating one BzH molecule would alter the affinity of the other four–ligand binding sites of an octahedrally coordinated metal ion in aqueous solution. An altered binding affinity at these sites results in a loss of degeneracy amongst them, which comes from a dependence on the first binding event. It is likely that the second binding event of BzH once again, forms a

Scheme 3.1 Structures of BzH in solution (Note: the *Z*–amide is predicted to be the more favourable structure) (García *et al*. 2005).

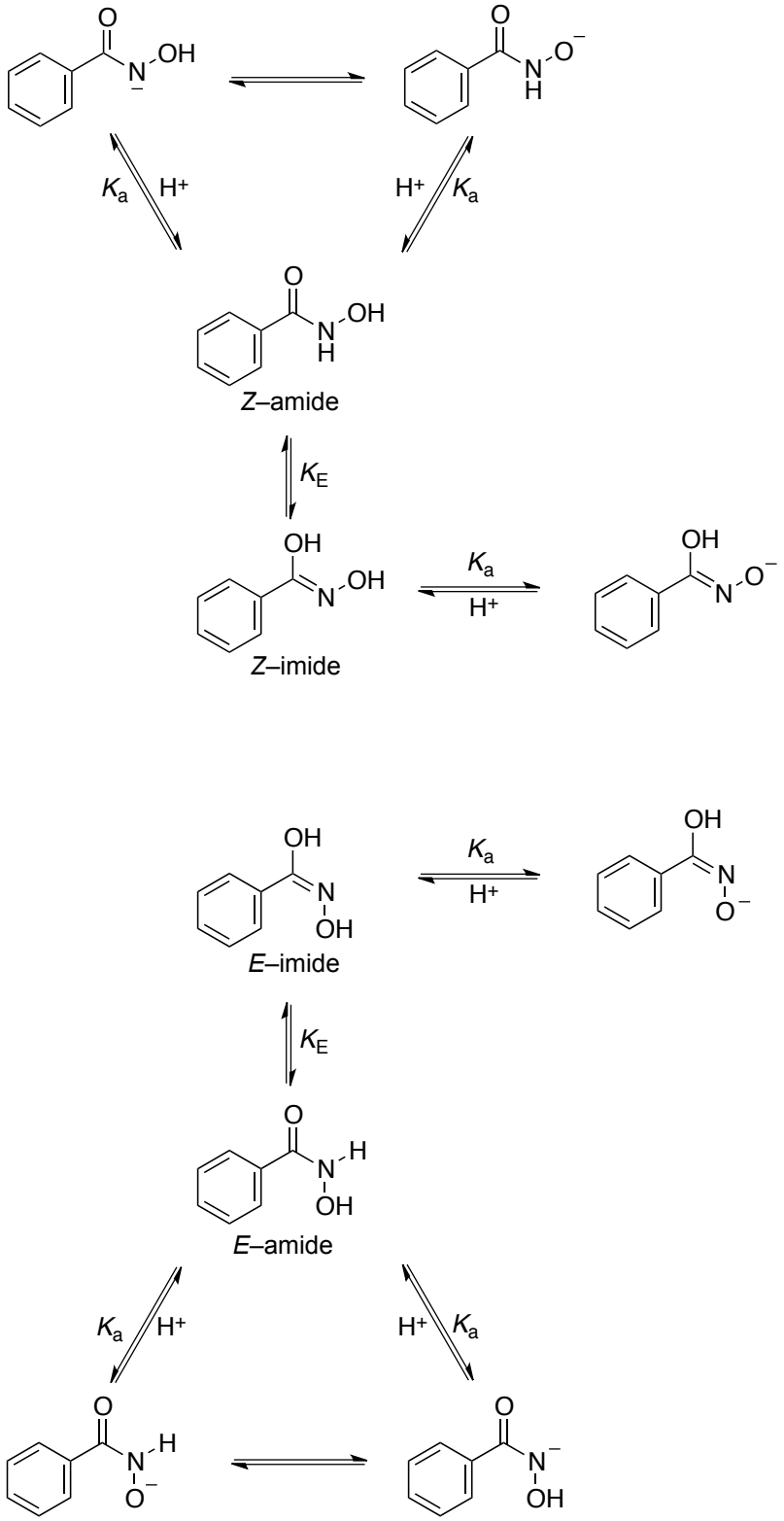

Scheme 3.2 Proposed binding model of *Z*–amide BzH to Ni^{2+} (Note: for simplicity it is shown that proton dissociation occurs upon metal ion coordination; however, a scenario where BzH remains protonated upon complex formation is possible).

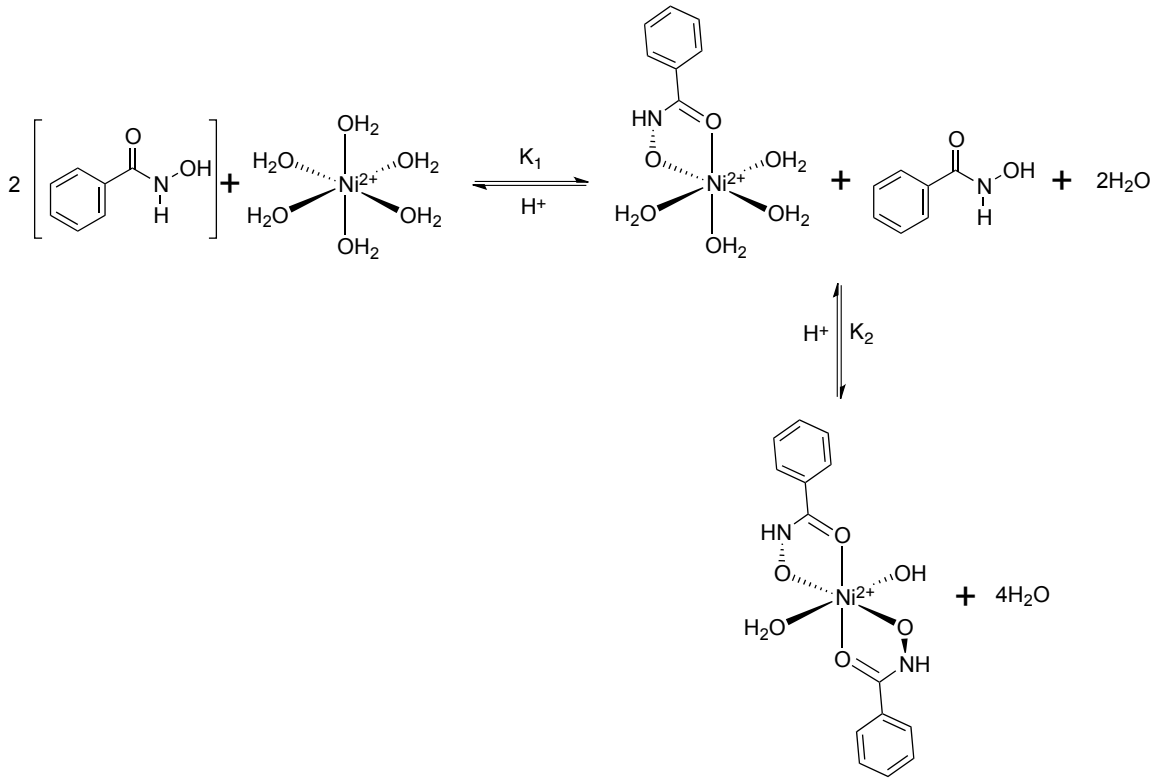

second 5–member cyclic structure with the metal ion–BzH complex since a metallacyclic ring is enthalpically favourable (**Scheme 3.2**) (Martel *et al*. 1995).

The choice of binding site shown in the proposed model (**Scheme 3.2**) is predicted to be the mirror image site of the first binding site. The binding of a second BzH at this site would restore symmetry to the complex and bring the orbitals into degeneracy according to the Jahn–Teller effect (Jahn and Teller, 1937). If the second BzH molecule were to bind at any site other than the proposed one, then it would create an even greater distortion to the octahedral geometry, which would be energetically unfavourable. The Jahn–Teller effect may also explain why the second binding affinity (K_2) of Co^{2+} observed in the present system is greater than the first one (K_1). In the case of Co^{2+}, the formation of a complex that restores symmetry (K_2), and therefore degeneracy, is more favorable than formation of a new complex (K_1). By contrast, in the case of Mg^{2+}, the lack of a second binding event between BzH and Mg^{2+} may indicate that the initial weak interaction (K_1) does not create the same level of distortion as it does for the other metal ions, and as a result there is no significant change to the affinity of the other possible binding sites and therefore the second binding event is very weak and essentially undetectable.

3.4.2 BzP–Ni^{2+} Complex Formation in Aqueous Solution

Observation of a weak–binding interaction between Ni^{2+} and BzP in aqueous solution is not surprising since it lacks the ability to chelate the metal ion in a bidentate fashion with a stable 5–, or 6–membered ring. It is likely that the complex formed is the result of a weak electrostatic interaction between the positively charged Ni^{2+} and the di–

anionic BzP; an event which we can observe using ITC. No other binding events were observed for any of the other metal ions and BzP.

3.4.3 Inhibition of Metal Ion–Bound Variants of MR by BzP

BzP was found to be a relatively good inhibitor of all metal ion–variants of MR, with IC_{50} values between 200 and 400 μM (**Table 3.2**). The amount of BzP required to inhibit the metal ion–bound variants of MR followed the order $Mg^{2+} \approx Mn^{2+} < Co^{2+} < Ni^{2+}$, meaning that the binding of BzP to the Ni^{2+}–bound MR was weaker than its binding to the other metal ion–bound variants. The difference between the IC_{50} values was slight (< 2–fold) and no trend emerged based on the inherent properties of the metal ions (**Table 2.4**). The two metal ions with the greatest variance in both substrate binding affinity and efficiency (k_{cat}/K_m), Mn^{2+} and Mg^{2+}, had roughly equal IC_{50} values (≈ 200 μM) for BzP. With such little variance in BzP binding amongst Mn^{2+}–and Mg^{2+}–bound MR, it would appear that either BzP is not an intermediate analogue or it is an intermediate analogue and the metal ion activator of MR plays only a minor role in the ability of MR to stabilize the intermediate that BzP resembles. This study does not examine the type of inhibition by BzP with each of the metal ion–bound variants of MR. Since there are no crystal structures of MR bound to any phosphonate compounds, I cannot say definitively that BzP interacts with the metal ion in the active site of MR. Overall, the various metal ion–MR variants do not exhibit different affinities for the dianionic ligand.

3.4.4 Inhibition of Metal–ion Bound Variants of MR by BzH

BzH was shown to be a competitive inhibitor of each of the metal ion–bound variants of MR, binding ~ 2 orders of magnitude tighter than the substrate. The lowest K_i

value, i.e, the tightest binding affinity observed, was for the Ni^{2+}–bound MR (2.7 ± 0.1 μM). The weakest binding affinity was observed for Mn^{2+}–bound MR (13 ± 2 μM). The stability of the metal ion–bound MR–BzH complexes formed follows the order of $Mn^{2+} \approx Mg^{2+} < Co^{2+} < Ni^{2+}$, which is approximately the Irving–Williams series. This trend is similar to what was observed for the K_1 values of BzH–metal ion complex formation in aqoueous solution (**section 3.4.1**), but much less pronounced. It would appear that each of the metal ions, when bound to the active site of MR, has its ability to bind BzH increased. However, because additional binding affinity also arises as a result of numerous other interactions within the active site, it is difficult to say how much of the BzH binding energy results from the metal ion alone.

3.4.5 The Hephaestus Effect

Previous studies have shown that metal ion–complex stabilities following the Irving–Williams series correlate with the electron affinities of the metal ions (Martin, 1998). In this study, there is also a strong correlation between the electron affinity of the metal ions (**Table 2.4**) and the standard free energy for metal ion and BzH complex formation in solution (ΔG_d^o) determined using the inverse of the first stability constant ($K_d = 1/K_1$, **Table 3.1**) and equation 3.14.

$$\Delta G_d^o = RT\ln(K_d) \qquad 3.14$$

This correlation is shown in **Figure 3.9**, where the standard free energy of binding (ΔG_i^o) of BzH for each metal ion–bound variant of MR, calculated using equation 3.15, also correlates to the electron affinities of the metal ions (**Figure 3.9**).

$$\Delta G_i^o = RT\ln(K_i) \qquad 3.15$$

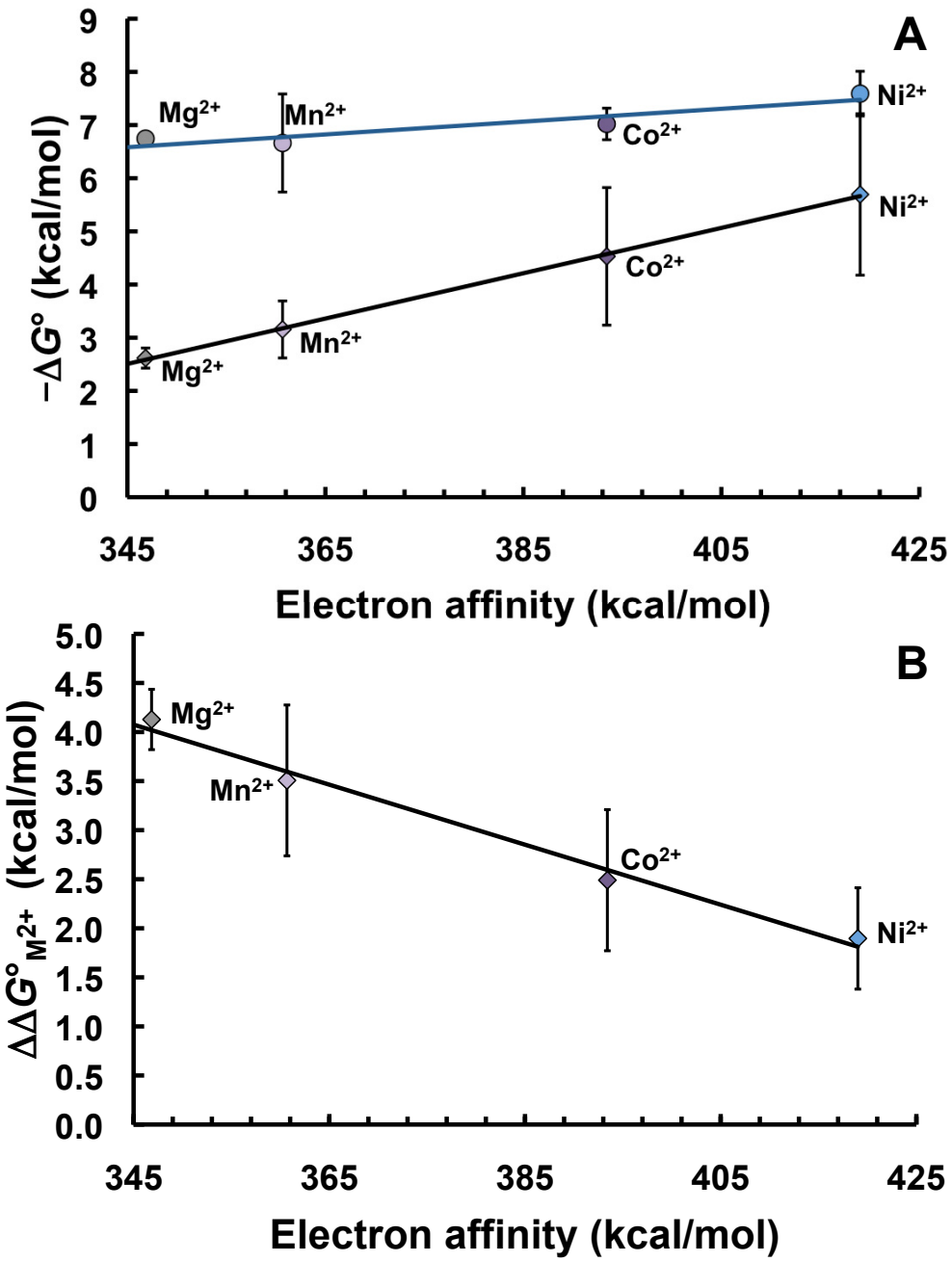

Figure 3.9 The change in standard free energy for the binding of metal ion and BzH in the active site of MR ($\Delta G_i°$, blue) and in aqueous solution ($\Delta G_d°$, black) versus metal ion electron affinity (A), and the difference between those free energy changes ($\Delta\Delta G°_{M^{2+}}$) versus the electron affinities of the metal ions (B). Plot A shows that an increase in change in standard free energy of binding BzH correlates well with an increase in electron affinity of the metal ion both in the active site of MR (blue) and in solution (black). Plot B shows that as the electron affinity increases, the difference between the standard free energy changes ($\Delta\Delta G°_{M^{2+}} = \Delta G_d° - \Delta G_i°$) of metal ion bound–MR and solution metal ion for BzH is less pronounced.

From **Figure 3.9,** we can see that as the electron affinity of the metal ion increases, so does the standard free energy change for formation of the metal ion–BzH complexes in aqueous solution and when bound to the active site of MR. The free energy change accompanying binding for metal ion with BzH appears to be enhanced in the active site of MR; an effect that is most pronounced for Mg^{2+}. This enhanced binding results from the added interactions present at the active site, but also appears to be metal ion–dependent. A plot of the $\Delta\Delta G^{o}_{M^{2+}}$ versus electron affinity (**Figure 3.9 panel B**), where $\Delta\Delta G^{o}_{M^{2+}} = G_d^{\circ} - \Delta G_i^{\circ}$, indicates that as the inherent electron affinity of the metal ion increases, the apparent enhancement of the ability of the metal ion to bind BzH, afforded by MR, decreases given that all other interactions between the enzyme and BzH are similar for each metal ion–MR variant. The $\Delta\Delta G^{o}_{M^{2+}}$ values also correlate well with the effective nuclear charge (Z_{eff}, calculated using Slater's rules) experienced by the outer shell electrons of the metal ions (**Figure 3.10**) (Slater, 1930). This correlation suggests that the greater the Z_{eff} value of the metal ion, the more resistant it is to the enhancement ($\Delta\Delta G^{o}_{M^{2+}}$) of its ability to bind BzH afforded by MR, resulting in a leveling of the apparent binding affinity of the metal ion–MR variants for BzH. This observation is consistent with the additional nuclear charge (Z_{eff}) being effectively shielded by the metal ion–binding ligands of the enzyme.

Another informative exercise may be to use a thermodynamic cycle to predict the binding affinity of each BzH–metal ion complex to apo–MR (**Scheme 3.3**). By using the affinity of metal ion for apo–MR (K_A) from chapter 2, the binding affinity of BzH for MR–metal ion complex (K_i), and the inverse of the stability constant for the metal–ion

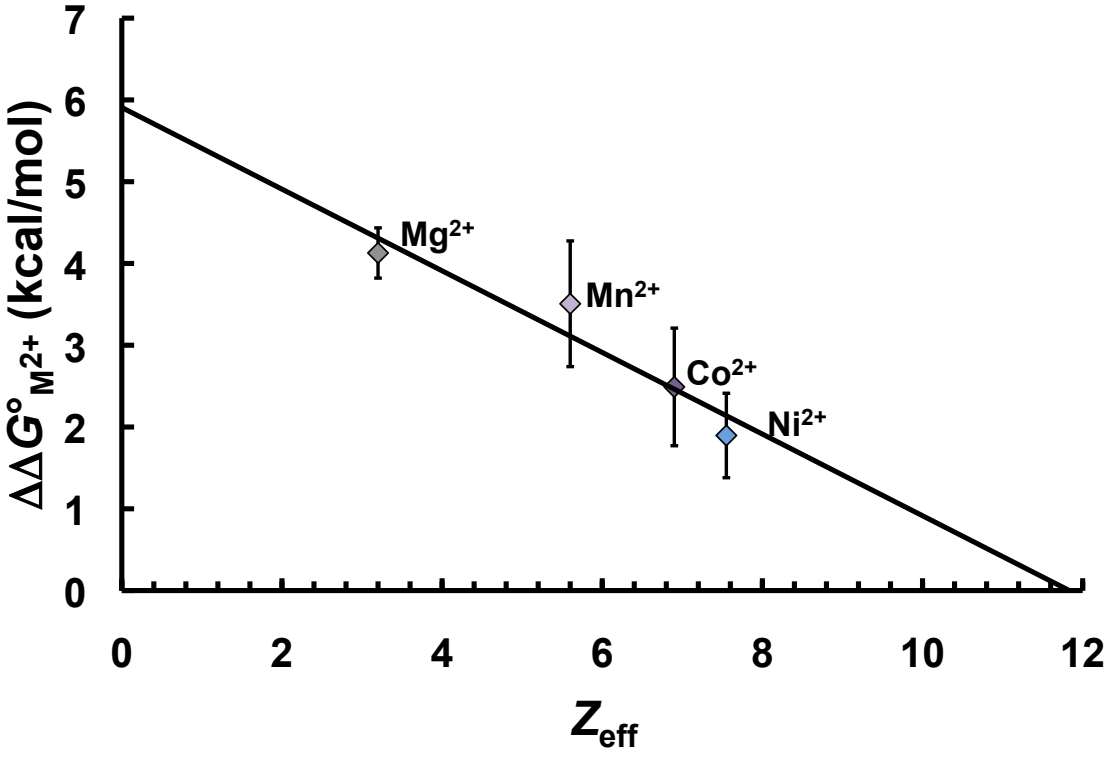

Figure 3.10 Plot of the difference in binding free energy changes ($\Delta\Delta G°_{M^{2+}}$) for metal ions and BzH in solution and in the active site of MR versus the effective nuclear charge (Z_{eff}) of those metal ions. There is a good correlation of the decrease in the $\Delta\Delta G°_{M^{2+}}$ values with increasing Z_{eff} values of the metal ions as calculated using Slater's rules (Slater, 1930).

Scheme 3.3 Thermodynamic cycle describing MR binding the BzH–metal ion complex ($K_{E+BzH•M^{2+}}$) and the MR–metal ion species binding BzH (K_i).

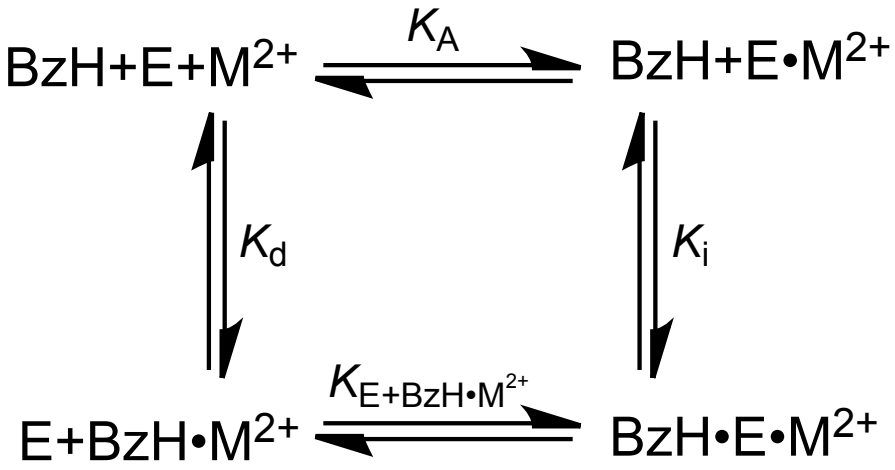

BzH complex determined by ITC ($K_d = 1/K_1$), we can estimate the binding affinity of apo–MR for the metal ion–BzH complex ($K_{E+BzH•M^{2+}}$) using equation 3.16.

$$K_{E+BzH•M^{2+}} = \frac{K_A K_i}{K_d} \qquad 3.16$$

This estimation of the affinity of apo–MR for a metal ion–BzH complex can be used to approximate a binding energy using equation 2.6 where *K* corresponds to the appropriate dissociation constant. For illustrative purposes, the free energy profile for MR–BzH–metal ion complex formation for both Mg^{2+} and Ni^{2+} are shown in **Figure 3.11** (panels **A** and **B**, respectively). The free energies of complex formation used to construct these profiles, as well as those for Co^{2+} and Mn^{2+} are listed in **Table 3.3**.

A comparison of the free energy profiles shows that in the case of Ni^{2+}, where the binding energy of Ni^{2+} and enzyme (ΔG_A^o) is roughly equal to the binding energy of Ni^{2+} and BzH (ΔG_d^o) in solution, the free energy for the binding of apo–MR and the BzH–Ni^{2+} complex ($\Delta G^o_{E+BzH•Ni^{2+}}$) is roughly equivalent to standard free energy determined by the BzH inhibition study (ΔG_i^o). However, when Mg^{2+} is the metal ion, there is a difference in the free energies for the binding of apo–MR to the BzH–Mg^{2+} complex ($\Delta G^o_{E+BzH•Mg^{2+}}$) and the binding of MR–$Mg^{2+}$ with BzH (ΔG_i^o) of 2 kcal/mol, which indicates that the enzyme's ability to bind the BzH–metal complex is enhanced relative to MR–Mg^{2+} binding free BzH. This enhancement can arise from the distortion of BzH by metal ion to enhance its binding; however, this is unlikely since there is no distortion to the structure of BzH in the crystal structure of BzH–bound WTMR (**Figure 3.1**) (Leitzan *et al.,* 2012) and a similar phenomenon would be expected for the Ni^{2+}–BzH complex. It is possible that only one of the multiple solution forms of BzH (**Scheme 3.1**) will form a stable

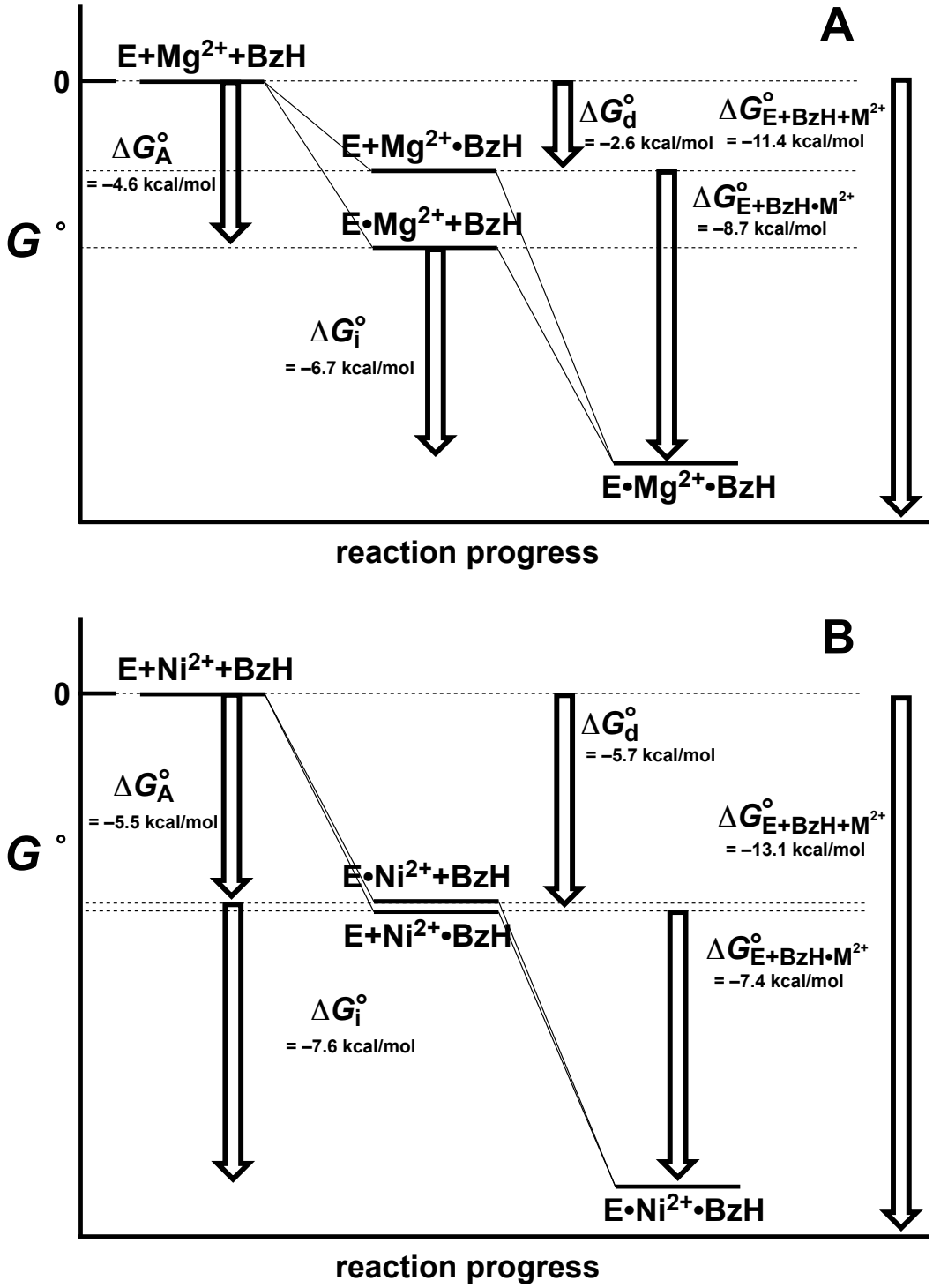

Figure 3.11 Free energy profile for binding of MR, BzH, and either Mg^{2+} (A), or Ni^{2+} (B) to form the MR–BzH–metal ion complex. The profile was constructed using the standard free energy changes from **Table 3.3**, which were calculated using equation 2.6 and the parameters from **Tables 2.3**, **3.1**, and **3.2**.

Table 3.3 Standard free energy changes for the binding of BzH, MR, and metal ion to form the MR–BzH–metal ion complex.

Metal ion	Mg^{2+}	Mn^{2+}	Co^{2+}	Ni^{2+}
$\Delta G°_{A}$ (kcal/mol)[a]	–4.64 (± 0.01)	–6.0 (± 0.3)	–5.8 (± 0.4)	–5.5 (± 0.6)
$\Delta G°_{d}$ (kcal/mol)[b]	–2.6 (± 0.2)	–3.2 (± 0.5)	–4.5 (± 1.3)	–5.7 (± 1.5)
$\Delta G°_{i}$ (kcal/mol)[c]	–6.7 (± 0.1)	–6.7 (± 0.9)	–7.0 (± 0.3)	–7.6 (± 0.4)
$\Delta G^{o}_{E+BzH•M^{2+}}$ (kcal/mol)	–8.7 (± 0.6)	–9.5 (± 2.1)	–8.3 (± 2.5)	–7.4 (± 2.2)
$\Delta G^{o}_{E+BzH+M^{2+}}$ (kcal/mol)	–11.4 (± 0.2)	–12.7 (± 1.9)	–12.8 (± 1.0)	–13.1 (± 1.6)
$\Delta\Delta G^{o}_{M^{2+}}$ (kcal/mol)	4.1 (± 0.3)	3.5 (± 0.8)	2.5 (± 0.7)	1.9 (± 0.5)

[a]Values from **table 2.3**.
[b]Values from equation 2.6 and $1/K_1$ from **Table 3.1**
[c]Values from equation 2.6 and K_i values from **Table 3.2**

complex with Mg^{2+}, and that conformation is already set for binding in the active site of MR therefore overcoming the entropic cost of coordination. This alteration in binding is not to be confused with the $\Delta\Delta G^{o}_{M^{2+}}$ (i.e., the difference in energy between metal ion and BzH in solution and MR–bound metal ion and BzH) mentioned earlier, which pertains only to the metal ion.

A very useful experiment would be to measure the extent to which MR binds BzH in the absence of the metal ion. Normally it would be possible to estimate this using an ITC binding study of apoMR with BzH; however, I was unable to observe this phenomenon with ITC, for a number of possible reasons. One reason is that the heat signature and/or affinity of an apoMR–BzH binding event is too low for an accurate determination of K_i. A second possible reason is that the active site could be significantly different in the absence of a bound–metal ion. Since there are no crystal structures of apoMR, we do not know the structure of the enzyme when the metal ion is absent. Metal ion binding may alter the tertiary and/or quaternary structure significantly upon binding. However, the apo– and Mg^{2+}–bound crystal structures for two other members of the enolase superfamily of enzymes, *o*–succinylbenzoate synthase from *E. coli* and muconate lactonizing enzyme from *P. putida*, have been solved and for each of these enzymes, the absence of a metal ion was not shown to alter the tertiary or quaternary structure, or perturb the structure of their active sites (Hasson *et al*., 1998; Helin *et al*., 1995; Thompson *et al*., 2000). Moreover, since superimposition of muconate lactonizing enzyme with MR indicates that the active sites are well conserved, there is little reason to suspect that the structures of apo–MR and metal ion–bound MR differ (Hasson *et al*., 1998).

In Chapter 2, MR was shown to catalyze the racemization of mandelate with approximately the same efficiency regardless of the identity of the bound metal ion. In this chapter, all the metal ion variants exhibited similar binding affinity for BzH, despite a more pronounced difference in binding affinities observed in solution (i.e., following the Irving–Williams series and correlating with the electron affinity or effective nuclear charge, Z_{eff}). This ability of MR to 'forge' the properties of the metal ions such that similar catalytic and binding properties arise I termed the 'Hephaestus effect'; named after the Greek god of blacksmithing and metallurgy. The 'Hephaestus effect' refers to the ability of a protein to alter the inherent properties of a metal ion. In the case of MR, either MR has enhanced the ability of Mg^{2+} to bind BzH or it has impeded the ability of metal ions with high Z_{eff} values (e.g., Ni^{2+}) to bind BzH. The greater effective nuclear charge on Ni^{2+} likely causes less positive charge to be available for binding BzH when it is coordinated at the active site of MR compared to what is available based on its behaviour in solution. On the other hand, Mg^{2+} does not coordinate MR residues as tightly (K_A = 0.394 mM for Mg^{2+} versus 0.091 mM for Ni^{2+}) with its lower effective nuclear charge, making more positive charge available for binding BzH. Hence, it appears that the 'Hephaestus effect' of MR indeed 'forges' the properties of Mg^{2+} to enhance its ability to bind BzH, and hence its catalytic properties when bound to MR.

3.4.6 Conclusions

From the present study it appears that there is a leveling effect for the binding of BzH by the metal ion–MR variants that suggests either the binding affinity of Mg^{2+}–MR for BzH is enhanced or the binding affinity of Ni^{2+}–MR for BzH is attenuated. A comparison of the Z_{eff} versus the change in the ability of metal ions to bind BzH in the

active site of MR versus solution ($\Delta\Delta G°_{M^{2+}}$) would lead one to believe that the latter scenario is more plausible and that metals with greater Z_{eff} values (i.e., Ni^{2+}) will have their Lewis acidity decreased due to more electron transfer from the coordinating residues of the enzyme. However, a comparison of the binding affinity of MR–Ni^{2+} for BzH ($\Delta G°_{i}$) and the binding affinity of MR for the BzH–Ni^{2+} complex ($\Delta G°_{E+BzH•M^{2+}}$) shows very little energetic difference between them ($\Delta\Delta G° \approx 0$); indicating that a MR–$Ni^{2+}$ interaction does not enhance the formation of a MR–Ni^{2+}–BzH complex. This does not preclude an alteration, by either enhancement or attenuation, of the ability of MR to alter the binding of BzH by Ni^{2+}.

It is possible that the Hephaestus effect may be present in other cambialistic enzymes, such as glyoxalase I (Clugston *et al*., 1998; Han *et al*., 1977), α–mannosidase (Hansen *et al*., 2014), superoxide dismutase (Martin *et al*., 1986), and/or carbonic anhydrase II (Price and Morel, 1990), all of which can utilize different enzymes for catalysis while still retaining catalytic efficiency. However, since these other cambialistic enzymes have not been studied to the extent that MR has, we cannot say that there has been any alteration to the properties of their metal ion–activators. A more detailed compilation and review of all cambialistic enzymes in the literature may be a worthwhile endeavour that could further develop the existence of the Hephaestus effect.

The similar binding affinities observed for BzP and each of the metal ion–bound variants of MR are consistent with the theory of a leveling effect in Lewis acidity; although the precise binding mode of BzP is not presently known. Future studies should be conducted on the binding of apoMR and BzH to determine the binding energy in

absence of metal ion, allowing us to verify the contribution of metal ion to BzH binding, and perhaps catalysis.

Chapter 4

The Effect of Metal Ion Replacement on the Racemization of the Alternative Substrate (*S*)–Trifluorolactate and the Kinetics of Mn^{2+}–Bound MR

4.1 Introduction

Mandelate racemase from *Pseudomonas putida* catalyzes the interconversion of the enantiomers of trifluorolactic acid (TFLA) (**Scheme 4.1**), stabilizing the altered TFLA in the transition state (ΔG_{tx}) by 20 kcal/mol (Nagar *et al*., 2011). The MR–catalyzed racemization of (*S*)–TFLA is independent of solvent microviscosity, indicating that when TFLA is the substrate, the chemical step on the enzyme (k_2, **Scheme 1.5**) is solely rate–determining (Nagar *et al*., 2011). By comparing the kinetic parameters (K_m, k_{cat}, and (k_{cat}/K_m)) for the conversion of (*S*)–TFLA to (*R*)–TFLA catalyzed by the different metal ion–bound variants of MR we can observe the effect varying the metal ion has on the chemical step (k_2, **Scheme 1.5**) of MR catalysis, and as a result, the ability of MR to stabilize the transition state of TFLA. This experiment may give an indication of whether the change in efficiency (k_{cat}/K_m) that results from metal ion replacement (**Chapter 2**) when mandelate is a substrate comes solely from an alteration of the interconversion of MR–bound enanatiomers of mandelate (k_2), or if the metal ion cofactor also plays a role in substrate association (k_1, **Scheme 1.5**) and product release (k_3, **Scheme 1.5**).

The affinity of MR for TFLA is similar to that of mandelate (1.74 mM for (*S*)–TFLA and 1.25 mM for (*R*)–TFLA; Nagar *et al*, 2011), with MR having the same enantioselectivity for TFLA as it does for mandelate (cf. 0.95 mM for (*R*)–mandelate and 0.71 mM for (*S*)–mandelate when Mg^{2+} is the co–factor; **Chapter 2**). (*S*)–TFLA was used in this study and compared to the racemization of (*R*)–mandelate (where the absolute

Scheme 4.1 Interconversion of the enatiomers of (*R*)– and (*S*)–trifluorolactate catalyzed by MR (note: (*S*)– and (*R*)–trifluorolactate have the same absolute stereoconfiguration as (*R*)– and (*S*)–mandelate, respectively)

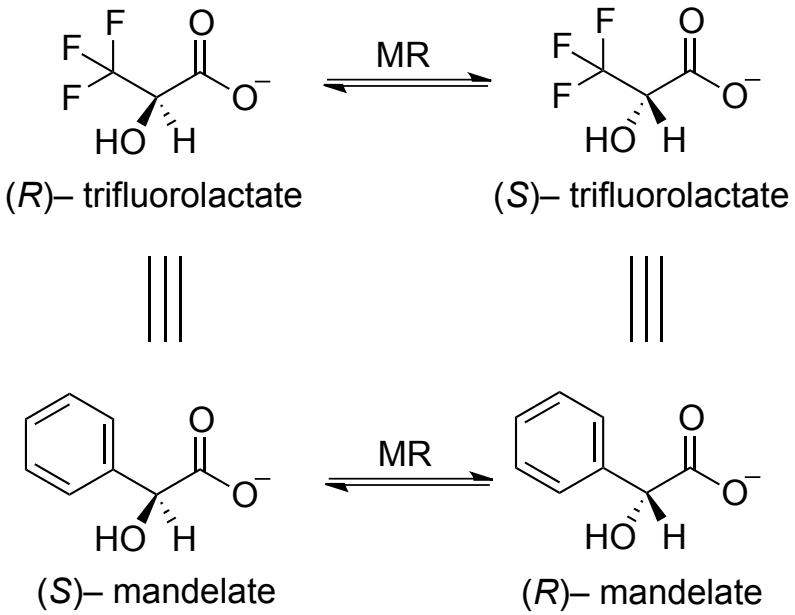

configuration about the α–carbon of (*S*)–TFLA corresponds to that of (*R*)–mandelate, placing the phenyl and CF_3 groups in the same spatial orientation (**Scheme 4.1**)). The CF_3 group of TFLA also binds with an affinity exceeding that which is predicted based on hydrophobic effects alone and it is suspected that the CF_3 group is held in the hydrophobic pocket of MR by weak dipolar interactions (Bégué, and Bonnet–Delpon., 2008; Nagar *et al*., 2012). This similar binding affinity, but low rate of catalysis (k_{cat} is ~400–fold lower than when mandelate is the substrate), provides a MR–catalyzed reaction in which the slow step is the abstraction of the proton. When the chemistry is rate–limiting, the effects of stabilization of the transition state relative to the ground state may be more pronounced and easier to observe. In this chapter, I will explore the effect that altering the metal ion has on the rate of MR–catalyzed racemization of TFLA to further delineate the role of the metal ion in transition state stabilization.

In addition to exploring the role of the metal ion in transition state stabilization, I will also look at the role of the metal ion in product association and substrate dissociation. One way to accomplish this is by varying the viscosity of the solvent during MR catalysis in order to measure the individual rate constants in **Scheme 1.5**. An estimation of the individual rate constants can be determined by measuring the effect varying solvent viscosity has on the kinetic parameters k_{cat} and (k_{cat}/K_m) (Brouwer and Kirsch, 1982). Theoretically, the limit for a diffusion–limited enzyme–catalyzed reaction is 10^8–10^{10} M^{-1} s^{-1} (Alberty and Hammes, 1958). Because the k_{cat}/K_m value of the reaction catalyzed by MR is on the order of 10^6 M^{-1} s^{-1}, it is only partially diffusion controlled (St. Maurice and Bearne, 2002). A viscosity variation experiment has been previously conducted on WTMR when Mg^{2+} is the metal ion activator and has shown that the

apparent $k_{cat}^{R \rightarrow S}$ (654 ± 58 s^{-1}) underestimates the rate constant for the conversion of bound (*R*)–mandelate to bound (*S*)–mandelate (cf. k_2 = 880 ± 40 s^{-1}) by nearly 30%, confirming that, when mandelate is the substrate, the rate of MR catalysis is at least partially dependent on substrate binding and product dissociation steps (St. Maurice and Bearne, 2002). Since Mg^{2+}– and Mn^{2+}–bound MR have the greatest variance in efficiency (**Chapter 2**), conducting a viscosity variance study using Mn^{2+}–bound MR and both (*R*)– and (*S*)–mandelate as substrates will allow for the estimatation of the kinetic constants, k_1, k_2, k_3, k_{-1}, k_{-2}, and k_{-3}. By comparing these constants for the two metal ion–bound variants (Mg^{2+} and Mn^{2+}) of MR, we can determine the extent to which altering the metal ion affects the rates of substrate binding and product release.

4.2 Materials and Methods

4.2.1 General

(*R*)– and (*S*)–Mandelic acid, (*S*)–trifluorolactate, and all other chemicals, unless otherwise stated, were of reagent grade or better and purchased from Sigma–Aldrich Canada, Ltd. (Oakville, ON). Circular dichroism (CD) assays were conducted using a JASCO J–810 spectropolarimeter.

4.2.2 CD–Based Assay Using the Alternative Substrate (*S*)–TFLA

MR activity was assayed using a similar CD–based assay as described by Sharp *et al*. and detailed in previous chapters (Sharp *et al*. 1979). Assays with (*S*)–TFLA were determined by following the change in ellipticity at 228 nm using a quartz cuvette with a 0.5–cm light path. Concentrations of TFLA used ranged between 0.5–10 mM. The final concentrations of enzyme used were, 47 μg/mL for Mn^{2+}–bound, 33 μg/mL for Mg^{2+}–, Ni^{2+}–, and Co^{2+}–bound MR (with 0.01% BSA in all assays). The molar ellipticity of

TFLA at 228 nm was $[\theta]_{228}$ = 4404 deg mol^{-1} cm^2 (– for (*S*)–TFLA and + for (*R*)–TFLA) (Nagar *et al*., 2011).

4.2.3 Viscosity Effects

Stock solutions of the monomeric viscogen sucrose were prepared at twice the desired final concentration in HEPES buffer (0.1 M, pH 7.5) containing $MnCl_2 \bullet 4H_2O$ (1 mM). The relative solvent viscosities ($\eta_{rel} = \eta/\eta^{\circ}$, where the superscript refers to the viscosity of HEPES buffer in the absence of added viscogen) of the sucrose–containing buffer solutions were calculated from the product of the solution densities (ρ) and their kinematic viscosities (η/ρ) at 25 ˚C which were measured previously by St. Maurice and Bearne (2002). The relative viscosities (η_{rel}) were 1.32, 1.88, 2.48, 3.06 and 3.42 for 10, 20, 27.5, 32.5 and 35 % (w/v) sucrose solutions, respectively (St. Maurice and Bearne, 2002).

Kinetic measurements were conducted using the CD–based assay described earlier (Sharp *et al*., 1979). Reaction mixtures were prepared in a rectangular quartz cuvette with a 1–cm light path. Reactions were initiated by addition of 100 μL of Mn^{2+}–bound MR (final enzyme concentration of 105–145 μg/mL) to a solution containing 900 μL of (*R*)– or (*S*)–mandelate (0.5–20 mM) in HEPES buffer (0.1 mM, pH 7.5) containing $MnCl_2 \bullet 4H_2O$ (1 mM) and BSA (0.01%) and 1000 μL of sucrose–containing buffer (prepared as stated above at twice the final concentration) (St. Maruice and Bearne, 2002).

4.2.4 Data Analysis

V_{max} and K_m were determined by fitting equation 2.5 to the initial velocity (v_i) data versus substrate concentration ([S]) using nonlinear regression analysis and the program

KaleidaGraph v. 4.0 from Synergy Software (Reading, PA). Protein concentrations were determined by measuring the absorbance at 280 nm using the molar extinction coefficient of 53, 400 $M^{-1}cm^{-1}$ (calculated using ProtParam tool available on the ExPASy server: http://web.expasy.org/protparam (Gasteiger *et al*., 2005)). The k_{cat} values were calculated by dividing V_{max} values by total enzyme concentrations ($[E]_t$) using an MW value of 41, 264 Da. Kinetic constants were determined in triplicate for all experiments.

4.3 Results

4.3.1 Kinetic Characterization of Metal Ion–Bound Variants of MR with the Alternative Substrate (*S*)–TFLA

The kinetic parameters of the metal ion–bound variants of MR for the alternative substrate (*S*)–TFLA are shown in **Table 4.1**. The turnover numbers ($k_{cat}^{(S)\text{–TFLA}}$) for Mn^{2+} and Mg^{2+}–bound MR are roughly the same (≈ 1.7 s^{-1}) and only slightly less than those of the Co^{2+}– and Ni^{2+}–containing metalloenzymes, which are the same ($k_{cat}^{(S)\text{–TFLA}} \approx 2.8\ s^{-1}$). Mn^{2+}–MR has the highest $K_m^{(S)\text{–TFLA}}$ (2.6 (± 0.4) mM) while the values of $K_m^{(S)\text{–TFLA}}$ for the other metal ion–bound variants of MR are all roughly equivalent (1.5 –1.9 mM) (**Table 4.1**). The efficiencies ($k_{cat}/K_m^{(S)\text{–TFLA}}$) follow the order $Co^{2+} \approx Ni^{2+} > Mg^{2+} > Mn^{2+}$, Since Ni^{2+} and Co^{2+} are within experimental error of each other they can be considered relatively the same.

4.3.2 Free Energy Profiles of the Reaction Catalyzed by the Metalloenzyme Variants of MR using the Alternative Substrate (*S*)–TFLA

Using equation 2.6 (**Section 2.3.3**) and the apparent dissociation constants (i.e., letting $K_s^{(S)\text{–TFLA}} \approx K_m^{(S)\text{–TFLA}}$) listed in **Table 4.1**, the standard free energy changes accompanying the ground state binding ($\Delta G°_T$) of (*S*)–TFLA under standard conditions

Table 4.1 Kinetic constants for the racemization of (*S*)–TFLA catalyzed by the metallo–variants of MR[a].

Metal ion	$K_m^{(S)\text{–TFLA}}$ (mM)	$k_{cat}^{(S)\text{–TFLA}}$ (s^{-1})	$k_{cat}/K_m^{(S)\text{–TFLA}}$ ($M^{-1}s^{-1}$)
Mg^{2+}	1.54 (± 0.02)	1.8 (± 0.1)	1.15 (± 0.07) × 10^3
Mn^{2+}	2.6 (± 0.4)	1.7 (± 0.1)	0.6 (± 0.1) × 10^3
Co^{2+}	1.5 (± 0.2)	2.8 (± 0.4)	1.9 (± 0.3) × 10^3
Ni^{2+}	1.8 (± 0.1)	2.8 (± 0.1)	1.5 (± 0.1) × 10^3

[a]Values are means of triplicate trials and reported errors are standard deviations.

were calculated and are listed in **Table 4.2**. The free energy of activation for conversion for both MR–bound (*S*)–TFLA in the ground state ($\Delta G^{\ddagger\circ}_{ET}$), and for free MR and free (*S*)–TFLA ($\Delta G^{\ddagger\circ}_{E+T}$), to the MR–bound altered substrate complex in the transition state under standard conditions, were calculated using equation 2.7 (**Section 2.3.3**) and the rate constants $k_{cat}^{(S)\text{–TFLA}}$ and $(k_{cat}/K_m^{(S)\text{–TFLA}})$ (**Table 4.1**) are listed in **Table 4.2** for each metal ion–bound variant of MR. The values for the free energy changes for each metal ion–bound variant of MR are all within 1 kcal of each other indicating that MR will racemize (*S*)–TFLA with equal efficiency regardless of the metal ion activator bound.

4.3.3 Effect of Viscosity Variation on Mn^{2+}–Bound MR

For enzyme–catalyzed reactions, the rate of the external steps of enzyme catalysis, such as enzyme–substrate association and enzyme–product dissociation (for MR, k_1 or k_{-3} and k_{-1} or k_3 respectively, from **Scheme 1.5**) are inversely proportional to relative solvent viscosity, while the rate of the internal steps (k_2 and k_{-2} for MR, **Scheme 1.5**) are independent of solvent microviscosity (Adams and Taylor, 1992; Brouwer, and Kirsch, 1982; Hale *et al*. 1993; Kurz *et al*. 1987; Mattei, *et al*. 1999; Pocker and Janjic, 1987). The values of k_{cat} and (k_{cat}/K_m) for Mg^{2+}–bound MR have been previously shown to have a partial dependence on the solvent microviscosity, suggesting that the product release and substrate association steps are partially rate–determining (St. Maurice and Bearne, 2002). Repeating this study using the alternative metal ion cofactor Mn^{2+} showed that the k_{cat} and k_{cat}/K_m values in both the $R \rightarrow S$ and $S \rightarrow R$ reaction directions for the MR–catalyzed racemization of mandelate also have a partial dependence on microviscosity

Table 4.2 Free energy changes accompanying racemization of (*S*)–TFLA catalyzed by the metallo–variants of MR[a].

Metal ion	ΔG°_{T}(kcal/mol)	$\Delta G^{\ddagger\circ}_{ET}$(kcal/mol)	$\Delta G^{\ddagger\circ}_{E+T}$(kcal/mol)
Mg^{2+}	–3.83 (± 0.05)	17.1 (± 0.4)	13.2 (± 0.4)
Mn^{2+}	–3.5 (± 0.5)	17.1 (± 0.4)	14 (± 1)
Co^{2+}	–3.8 (± 0.5)	17 (± 1)	12.9 (± 0.9)
Ni^{2+}	–3.7 (± 0.2)	16.8 (± 0.3)	13.1 (± 0.4)

[a]Values are means of triplicate trials and reported errors are standard deviations.

(**Table 4.3**). Plots of the viscosity dependence of $1/k_{cat}$ and K_m/k_{cat} are shown in **Figure 4.1**.

Using the viscosity variation method described previously (Brouwer and Kirsch, 1982; Mattei *et al*., 1999; St. Maurice and Bearne, 2002) and knowing that the rate constants k_1, k_{-1}, k_3, and k_{-3}, are inversely proportional to solvent microviscosity (where $k_i = k_i^\circ/\eta_{rel}$, and i = 1, –1, 3, or –3, and $\eta_{rel} = \eta/\eta^\circ$; where k_i° denotes the rate in the absence of viscosity and η° the viscosity of HEPES buffer in absence of viscogen), we can express equations 1.1–1.6 in terms of η/η° as equations 4.1–4.4 (St. Maurice and Bearne, 2002).

$$\frac{1}{k_{cat}^{R\rightarrow S}} = \left(\frac{k_{-2}+k_2}{k_2 k_3^\circ}\right)\frac{\eta}{\eta^\circ} + \frac{1}{k_2} \qquad 4.1$$

$$\frac{K_m^{(R)-man}}{k_{cat}^{R\rightarrow S}} = \frac{1}{k_1^\circ}\left(\frac{k_{-1}^\circ k_{-2}}{k_2 k_3^\circ} + 1\right)\frac{\eta}{\eta^\circ} + \frac{k_{-1}^\circ}{k_1^\circ k_2} \qquad 4.2$$

$$\frac{1}{k_{cat}^{S\rightarrow R}} = \left(\frac{k_{-2}+k_2}{k_{-1}^\circ k_{-2}}\right)\frac{\eta}{\eta^\circ} + \frac{1}{k_{-2}} \qquad 4.3$$

$$\frac{K_m^{(S)-man}}{k_{cat}^{S\rightarrow R}} = \frac{1}{k_{-3}^\circ}\left(\frac{k_2 k_3^\circ}{k_{-1}^\circ k_{-2}} + 1\right)\frac{\eta}{\eta^\circ} + \frac{k_3^\circ}{k_{-2}k_{-3}^\circ} \qquad 4.4$$

The plot of $1/k_{cat}$ versus η/η° for the $R\rightarrow S$ and $S\rightarrow R$ reaction directions (**Figure 4.1 (A)**) have y–intercepts equal to $1/k_2$ and $1/k_{-2}$, respectively. Using the values of k_2 and k_{-2} calculated from these intercepts, and the slope of the plots, the values of k_{-1}° and k_3° can be calculated. Using these rate constants, equations 4.2 and 4.4, and the slopes and y–intercepts from the plot of the K_m/k_{cat} versus η/η° in the $R\rightarrow S$ and $S\rightarrow R$ reaction directions (**Figure 4.1 (B)**), the rate constants k_1° and k_{-3}° can be calculated. **Table 4.4** lists the

Table 4.3 Dependence of k_{cat} and (k_{cat}/K_m) on solvent microviscosity in both the $R \rightarrow S$ and $S \rightarrow R$ reaction directions at 25 °C for the Mn^{2+}–bound MR catalyzed racemization of mandelate[a].

Sucrose [%w/v]	η/η°	$k_{cat}^{R\rightarrow S}$ (s^{-1})	$(k_{cat}/K_m)^{R\rightarrow S}$ ($M^{-1}s^{-1}$)	$k_{cat}^{S\rightarrow R}$	$(k_{cat}/K_m)^{S\rightarrow R}$ ($M^{-1}s^{-1}$)
0.0	1	104 (± 6)	8.4 (± 0.8) × 10^5	70.2 (± 1.4)	1.80 (± 0.99) × 10^6
10.0	1.32	98 (± 3)	7.4 (± 1.1) × 10^5	70.6 (± 4.4)	1.31 (± 0.18) × 10^6
20.0	1.88	85 (± 5)	7.3 (± 0.6) × 10^5	63.7 (± 2.9)	1.45 (± 0.20) × 10^6
27.5	2.48	75 (± 10)	6.4 (± 1.7) × 10^5	57.5 (± 1.7)	1.36 (± 0.14) × 10^6
32.5	3.06	67.7 (± 0.9)	6.7 (± 0.2) × 10^5	51.6 (± 0.9)	1.39 (± 0.23) × 10^6
35	3.42	63 (± 4)	5.0 (± 1.6) × 10^5	48.9 (± 5.2)	1.19 (± 0.24) × 10^6

[a]Values are means of triplicate trials and reported errors are standard deviations.

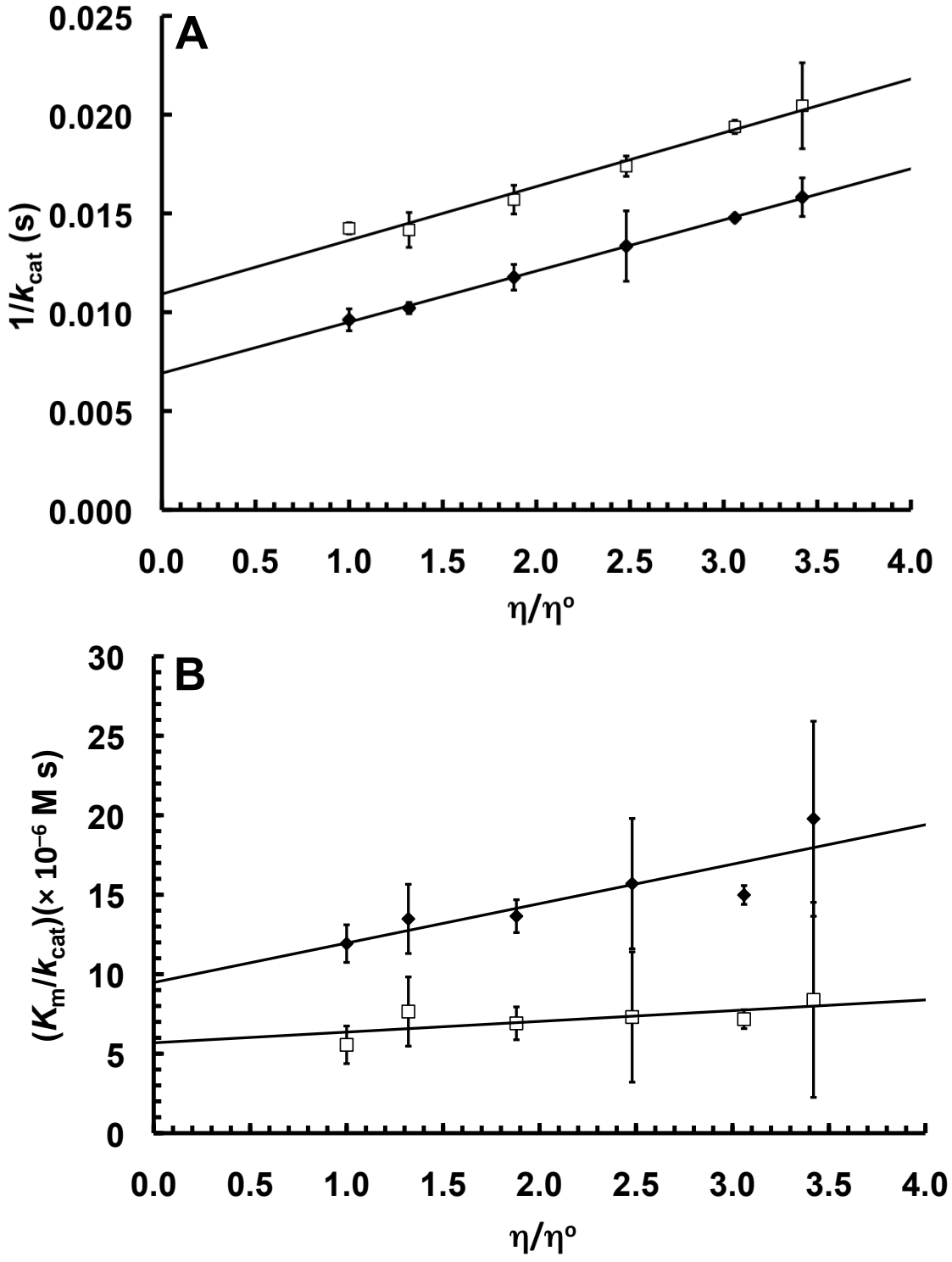

Figure 4.1 Dependence of $1/k_{cat}$ (A) and K_m/k_{cat} (B) on relative solvent viscosity (η/η°) for the racemization of (*R*)–mandelate (◆) and (*S*)–mandelate (□) catalyzed by Mn^{2+}–bound MR in sucrose–containing buffers at 25 °C.

Table 4.4 Rate constants and corresponding free energies of activation for the reaction catalyzed by Mn^{2+}– and Mg^{2+}–bound MR (values for Mg^{2+} from Bearne and St. Maurice, 2002).

Rate constant	Mn^{2+}	$\Delta G^{\ddagger}$ (kcal/mol) at 25 ° C	Mg^{2+}	$\Delta G^{\ddagger}$ (kcal/mol) at 25 ° C
k_1	6.9 (± 1.2) × 10^5 M^{-1} s^{-1}[a] 7.8 (± 2.2) × 10^5 M^{-1} s^{-1}[b]	9.4 (± 1.7)[d] 9.4 (± 2.7)[d]	3.21 (± 0.31) × 10^6 M^{-1} s^{-1}[ac] 6.73 (± 0.80) × 10^6 M^{-1} s^{-1}[bc]	8.6 (± 0.8)[cd] 8.2 (± 1.0)[cd]
k_{-1}	947 (± 59) s^{-1}	13.4 (± 0.8)	3948 (± 199) s^{-1}[c]	12.5 (± 0.6)
k_2	144 (± 2) s^{-1}	14.5 (± 0.2)	889 (± 40) s^{-1}[c]	13.4 (± 0.2)
k_{-2}	92 (± 4) s^{-1}	14.8 (± 0.6)	693 (± 20) s^{-1}[c]	13.6 (± 0.4)
k_3	631(± 30) s^{-1}	13.6 (± 0.7	3896 (± 276) s^{-1}[c]	12.6 (± 0.9)
k_{-3}	1.2 (± 0.2) × 10^6 M^{-1} s^{-1}[a] 3.0 (± 1.6) × 10^6 M^{-1} s^{-1}[b]	9.17 (± 1.5)[d] 8.63 (± 4.57)[d]	4.46 (± 0.45) × 10^6 M^{-1} s^{-1}[ac] 6.87 (± 0.64) × 10^6 M^{-1} s^{-1}[bc]	8.4 (± 0.8)[cd] 8.1 (± 0.8)[cd]

[a]Values calculated from the y–intercepts of (K_m/k_{cat}) versus. η/η° (**Figure 4.1 (B)**).
[b]Values calculated from the slopes of (K_m/k_{cat}) versus. η/η° (**Figure 4.1 (B)**).
[c]Values from St. Maurice and Bearne (2002).
[d]Values calculated for a standard state of 1 M.

values for the rate constants for Mn^{2+}–bound MR, determined in this study, and those previously determined literature values for the rate constants of Mg^{2+}–bound MR (St. Maurice and Bearne, 2002).

The rate constant k_1 for the association of (*R*)–mandelate to enzyme is lower for Mn^{2+} than it is for Mg^{2+} by almost 1 order of magnitude. The rate constant for the association of (*S*)–mandelate, however, is within the same order of magnitude but still nearly 4–fold higher for Mg^{2+}. The rate constant for dissociation of (*R*)–mandelate (k_3) is more than 6–fold lower for Mn^{2+}–bound MR, while the rate constant for dissociation of (*S*)–mandelate (k_{-1}) is only 4–fold lower. The rate constants for the internal steps (k_2 and k_{-2}) for the reaction catalyzed by Mn^{2+}–bound MR are also lower than that of Mg^{2+}–MR, with k_2 and k_{-2} being ~ 6–fold and ~ 7–fold lower, respectively. To illustrate the differences more clearly, the free energies of activation have been plotted for Mn^{2+}– and Mg^{2+}–bound MR (**Figure 4.2)**, under standard state conditions ([(*R*)–mandelate] and [(*S*)–mandelate] = 1M) using equation 2.7 (**section 2.2.3**) and the rate constants determined by the method of viscosity variation (**Table 4.4**). From **Figure 4.2**, it is apparent that when Mn^{2+} replaces Mg^{2+} in the active site of MR, the transition states (both internal and external) increase in energy, while the ground state MR–substrate complex is at the same energy level.

It is noted that the errors associated with the rate constants k_1 and k_{-3} are substantially greater (~30%) than those associated with the other rate constants. This is due to their being determined from the slopes and y–intercepts of the $(K_m/k_{cat})^{app}$ versus $\eta/\eta°$ plots, which has a significantly higher error due to an increased inherent error in the K_m^{app} values determined during the viscosity variation experiment. The increased error in

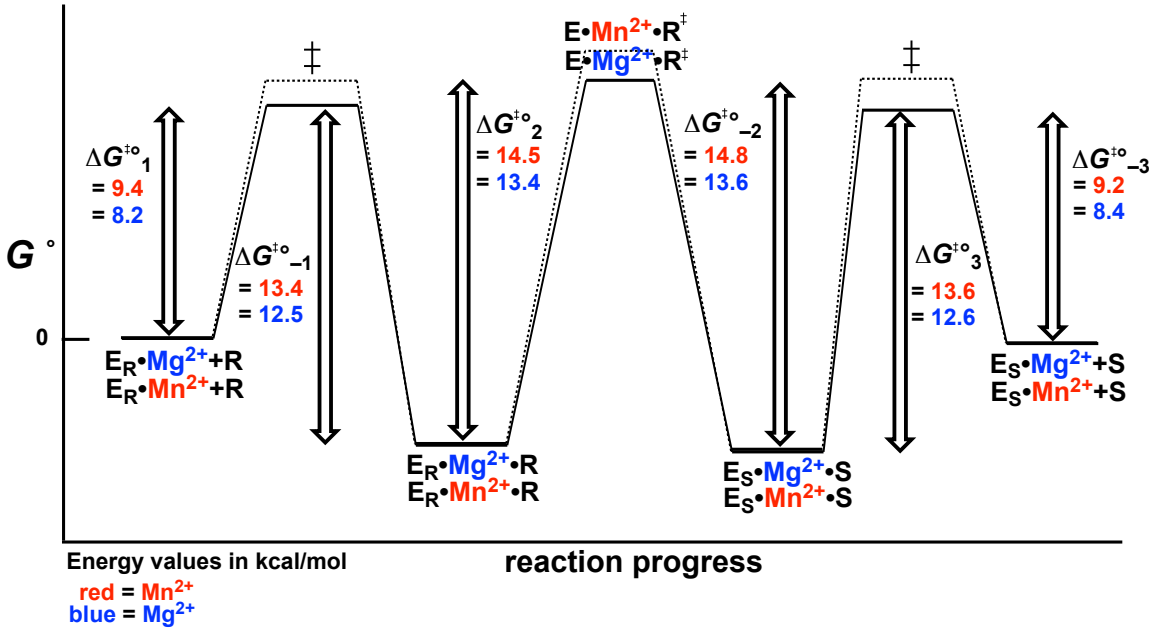

Figure 4.2 Overlay of the free energy profiles for the reactions catalyzed by Mg^{2+} (blue) and Mn^{2+} (red) bound MR at 25 °C. Comparison of the free energies of activation ($\Delta G^{\ddagger o}_i$, determined from the corresponding rate constants k_i , where i = 1, 2, 3, –1, –2, –3) for both Mg^{2+}–bound MR (solid lines) and Mn^{2+}–bound MR (dashed lines) indicates that the free energy of the enzyme–bound species in the ground state remains unchanged regardless of the metal ion activator. This plot also shows that all the transition states (internal and external) are higher in energy when Mn^{2+} is the activator illustrating that the metal ion is involved in stabilization of the transition state of the activated complexes ($Mg^{2+} > Mn^{2+}$). Free energies are in kcal/mol.

K_m^{app} results from a decreased signal–to–noise ratio during the CD–assay at high viscogen concentrations, which can make it difficult to measure the velocity of the reaction when using low concentrations of substrate (i.e., below K_m^{app}). Initial velocity measurements at concentrations below the K_m value are required for accurate determination of K_m. Slight inaccuracies will subsequently be magnified in the slope of the $(K_m/k_{cat})^{app}$ versus $\eta/\eta°$ plot.

4.4 Discussion

Two sets of experiments were described in this chapter to determine if the metal ion cofactor plays a role in the product release and/or substrate association steps of MR catalysis or if it is primarily involved in transition state stabilization. In the first set of experiments, the catalysis of TFLA racemization by the different metal ion–bound variants of MR was examined. It was found that there was little change in enzyme efficiency when the metal ion was replaced. Since the chemical step in TFLA racemization by MR is known to be rate–limiting (Nagar *et al*, 2011), and varying the metal ion activators did not have a significant effect on the efficiency of racemization of TFLA by MR, we can presume that the different metal ions play a similar role in stabilization of altered substrate in the altered transition state, or that there is an insensitivity to the identity of the metal ion as observed in **chapter 2**. It is also possible that the binding orientation of TFLA during catalysis is different than that of mandelate, resulting in very little interaction between TFLA and metal ion. As a result, replacing the metal ion in the active site of MR and observing the ability of the enzyme to racemize TFLA may not provide us with an opportunity to observe the role of the metal ion in the chemical step of the racemization of mandelate by MR.

The second experiment conducted was the method of viscosity variation. The parameters k_{cat} and k_{cat}/K_m for Mg^{2+}–bound MR catalysis of mandelate are known to be dependent on viscosity indicating that product dissociation and substrate association are partially rate–determining (St. Maurice and Bearne, 2002). Conducting a viscosity variation study with Mn^{2+}–bound MR, and comparing the determined rate constants to those accompanying the racemization reaction catalyzed by Mg^{2+}–bound MR, showed product dissociation and substrate association are partially rate–determining. Unlike the TFLA study, the viscosity study provides a deeper understanding of the role of the metal ion, mainly that it is involved predominantly in stabilization of both external and internal transition states.

4.4.1 Kinetic Characterization of Metal Ion–Bound Variants of MR with the Alternative Substrate (*S*)–TFLA

The efficiencies for the enzyme–catalyzed racemization of (*S*)–TFLA by the metal–bound variants of MR can be considered relatively the same (**Table 4.2**). During catalysis, the interaction between MR and the phenyl ring of mandelate provides stabilization of the increased negative charge of the transition state through conjugation (Nagar *et al*., 2011). However, when TFLA is the substrate, the inductive effect afforded by the trifluoromethyl group of TFLA is less effective at stabilizing the transition state resulting in a slower rate of MR–catalyzed racemization of TFLA, despite TFLA having a binding affinity ((*S*)–TFLA K_m = 1.74 mM) similar to that of ground–state mandelate (cf. (*R*)–mandelate K_m = 0.95 mM) (Nagar *et al*., 2011; Nagar *et al*., 2014).

The X–ray crystal structure of WTMR bound to the substrate–product analogue 3,3,3–trifluoro–2–hydroxy–2–(trifluoromethyl)–propanoate (TFHTP) (K_i = 27 μM)

(**Figure 4.3**), where the hydroxyl group of TFLA has been replaced with a second triflouromethyl group, shows that the carboxyl group of the ligand does not chelate the metal ion but forms a salt bridge between the carboxylate group of the ligand and the two catalytic residues Lys 166 and His 297 (Nagar *et al,* 2014). TFHTP is a potent inhibitor, binding MR 25–fold tighter than benzilate (K_i = 0.67 mM), the substrate–product analogue of mandelate (Siddiqi *et al*, 2005; Nagar *et al* 2014). Inhibition studies with the competitive inhibitor α–hydroxyisobutyrate (K_i = 5.5 mM), where the CF_3 groups have been replaced with methyl groups, show that the CF_3 groups of TFHTP do significantly contribute to its binding at the active site of MR, in addition to the salt bridges (Nagar *et al*., 2014).

If the binding orientation of TFLA were analogous to TFHTP, then the metal ion of MR may only interact with TFLA through outer–sphere coordination. As mentioned earlier (**section 1.2.3**), outer–sphere coordination can stabilize increased electronegative charge of a transition state through hydrogen bonding and electrostatic contributions (Black *et al*., 1996; Black *et al*., 1997). A proposed binding model for TFLA to the active site of MR is shown in **Figure 4.4**. If the stabilization of TFLA in the altered transition–state afforded by the metal ion comes only from hydrogen bonding, then there may be less variance in enzyme efficiency when that metal ion is replaced. At the present time, with only kinetic data, I cannot say that the binding orientation of TFLA is the same as that of either TFHTP or mandelate. Although the racemization of mandelate was relatively unaffected by the change of the metal ion activator (with the slight exception of Mn^{2+}–MR, which showed an approximately 10–fold reduction in efficiency relative to Mg^{2+}–MR), the insensitivity of TFLA racemization to the identity of metal ion is even

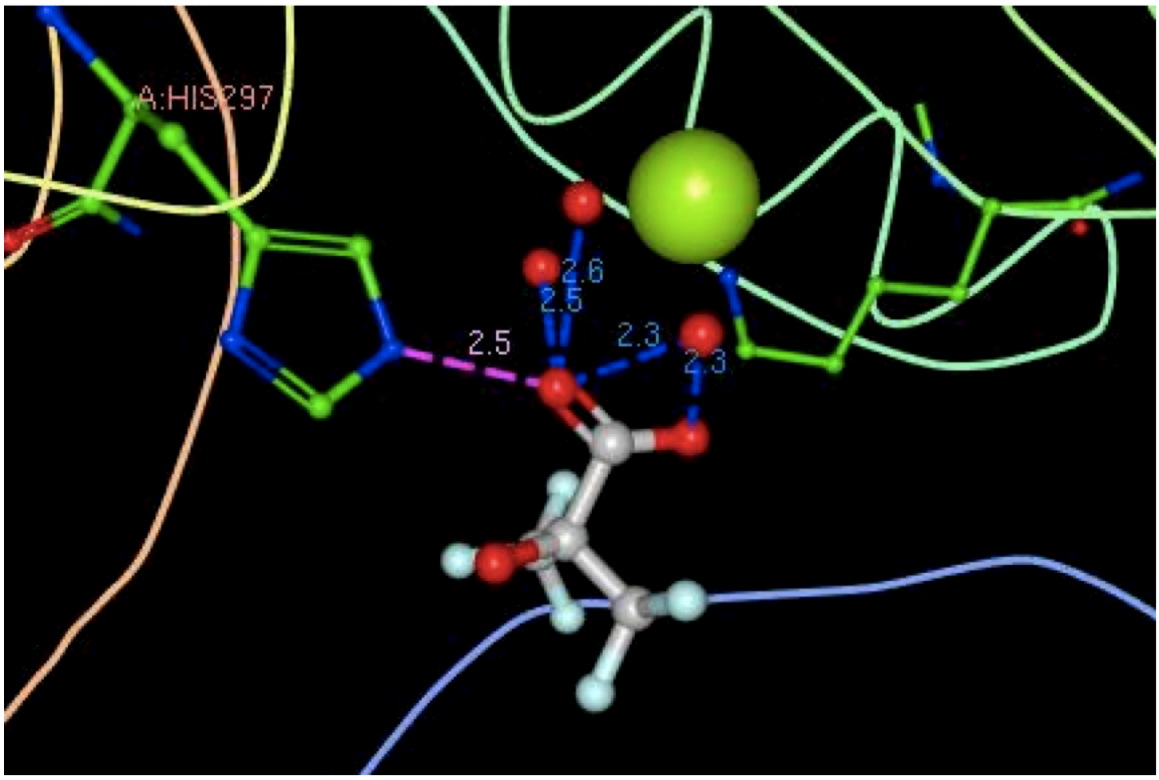

Figure 4.3 X–ray crystal structure of TFHTP bound to WTMR [PDB = 4FP1 (Nagar *et al*., 2014)]. The oxygen atoms of the carboxylate group of the competitive inhibitor TFHTP are shown within hydrogen bonding distance of three water molecules which are octahedrally coordinated to Mg^{2+} in the active site of MR. The residues His 297 and Lys 166 are shown to be within hydrogen bonding distance of the carboxylate moiety of TFHTP. Distances shown are in Å.

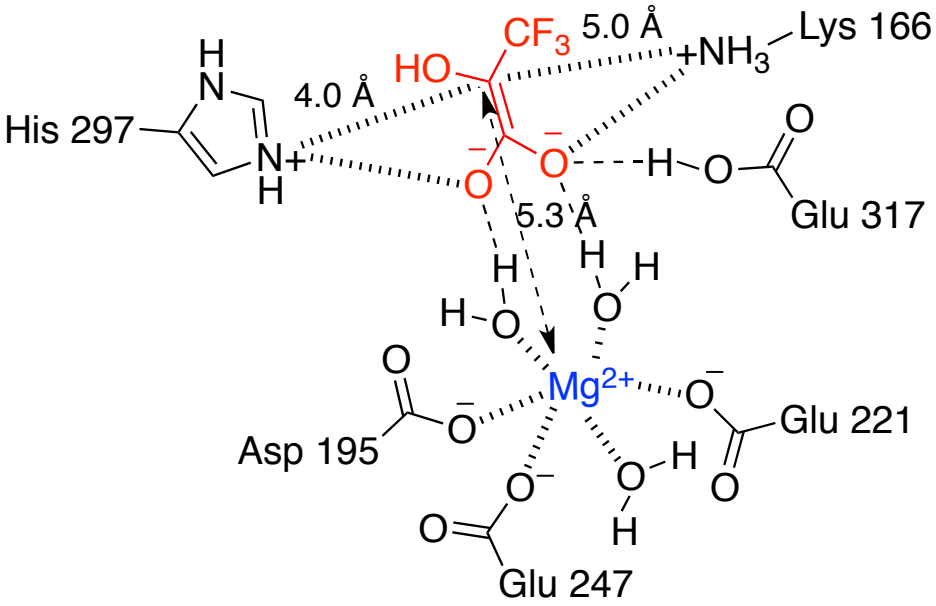

Figure 4.4 Possible model for the stabilization of the enolate intermediate of TFLA in the active site of MR. From crystal structures, the distance between the α–C of both TFHTP and (*S*)–atrolactate and the catalytic residues His 297 and Lys 166 are 4.0 and 5.0 Å (Landro, *et al*., 1994; Nagar *et al*., 2014). The distance between Mg^{2+} and the α–C of (*S*)–atrolactate is 3.1 Å versus 5.3 Å for TFHTP, indicating if TFLA were to bind in a similar fashion to TFHTP it would look like the model above.

more prominent. This marked insensitivity when TFLA is the substrate could arise because of an altered binding orientation and/or the involvement of the metal ion only in the chemical step of TFLA catalysis, as opposed to both the chemical step and the substrate association and product dissociation steps, as is the case for mandelate racemization (vide infra).

4.4.2 Effect of Viscosity Variation on Mn^{2+}–Bound MR

The viscosity dependence of k_{cat}/K_m and k_{cat} for the reaction catalyzed by Mn^{2+}–bound MR was used to measure the degree to which the substrate–association and product–dissociation steps were rate–determining. The dependence of k_{cat} on viscosity in both the $R \rightarrow S$ and $S \rightarrow R$ reaction directions is evidence that the internal chemical step (k_2 or k_{-2}) is not solely rate–limiting and that there is a partial dependence on product release (k_3 or k_{-1}). Likewise, the dependence of k_{cat}/K_m on viscosity in both the $R \rightarrow S$ and $S \rightarrow R$ reaction directions indicates substrate association (k_1 or k_{-3}) is also partially rate–limiting. This is the case for Mg^{2+}–bound MR (St. Maurice and Bearne, 2002) and also for Mn^{2+}–bound MR. The free energy barrier for racemization of bound substrate is ~1 kcal/mol greater than the free energy barrier for both enzyme–substrate association and enzyme–product dissociation when either Mn^{2+} or Mg^{2+} are bound to MR (**Figure 4.2**). This indicates that product dissociation and substrate association are not significantly favored over the proton abstraction step in the MR–catalyzed racemization of mandelate when either Mn^{2+} or Mg^{2+} is the cofactor.

All of the internal and external transition states are proportionately greater in energy when Mn^{2+} is the cofactor relative to when Mg^{2+} is the cofactor (**Figure 4.3**), indicating that Mn^{2+}–bound MR is less efficient at stabilizing each transition state to the

same degree. The energy difference between free enzyme and substrate and enzyme–bound substrate ($K_S = k_{-1}/k_1$) is approximately the same regardless of which metal ion activator is used (**Figure 4.3**). The value of the association and dissociation rate constants for Mn^{2+}–bound MR are lower than they are for Mg^{2+} indicating that the metal ion does affect the rate of product dissociation and substrate association.

The reason for the partial dependence of MR catalysis on substrate association/product dissociation is not known (St. Maurice and Bearne, 2002). The values for the association rate constants (k_1 and k_{-3}) for both Mg^{2+}– and Mn^{2+}–bound MR are several orders of magnitude (1~2 for Mg^{2+}, 2~3 for Mn^{2+}) lower than the theoretical values of diffusive association rate constants for enzymatic reactions of 10^8–10^{10} M^{-1} s^{-1} (Alberty and Hammes, 1958). There are a number of possible explanations, including the requirement for desolvation of the ligand and the active site (Bartlett and Marlowe, 1987; Blacklow *et al*., 1988), a conformational change of the apo–enzyme to a rare form required for ligand binding (Blacklow *et al*., 1988), unproductive binding (Simopolous and Jencks, 1994), or perhaps a partially rate–determining conformational change that must occur after substrate binding but prior to the internal chemical step (Hoggett and Kellet, 1976; Kurz *et al*., 1987*; Wang* et al. 1999). In the context of MR, the case may be that the displacement of the water molecules coordinated the metal ion when the ligand binds may be limiting the apparent rate of association of substrate. If this is the case then the displacement of the two water molecules by mandelate is faster for Mg^{2+} than it is for Mn^{2+}. However, this is contrary to what has been observed in solution, where the rate constant for the exchange of inner–sphere water molecules with other bulk solvent water molecules and ligands has always been shown to be faster when Mn^{2+} ($k \approx 10^6$ s^{-1}) is the

metal ion versus Mg^{2+} ($k \approx 10^5\ s^{-1}$) (Frey and Stuerhr, 1974; Fraústo da Silva and Williams, 2001; Helm and Merbach, 1999; Ducommun *et al*., 1982). These rates depend largely on the symmetry of the complex formed and the type of ligand involved; even so, in all aqueous solutions Mn^{2+} will have a faster water exchange rate than Mg^{2+} (Frey and Stuerhr, 1974; Helm and Merbach, 1999).

4.4.3 Conclusions

From the viscosity variation experiments it is evident that the metal ions play a role in uniform binding (Albery and Knowles, 1976) of the transition states for substrate association, product dissociation, and the chemical step. However, no apparent change in binding of the ground state species is observed. Consequently, replacement of Mg^{2+} by Mn^{2+} in MR furnishes an example of differential binding (Albery and Knowles, 1976). By contrast, the racemization of TFLA catalyzed by the different metal ion variants of MR did not provide much information on the role of the metal ion. X–ray crystal structural information delineating how TFLA, or an appropriate analogue, binds in the active site would be helpful to understand the insensitivity of TFLA racemization to the identity of the metal ion cofactor.

Chapter 5

Conclusions and Recommendations for Future Work

MR, a highly proficient, cambialistic enzyme, serves as a model enzyme to study how a metalloenzyme can alter the properties of a metal ion for use in catalysis. Using four different metal ions, Mg^{2+}, Mn^{2+}, Co^{2+}, and Ni^{2+}, as activators of MR affords the chance to compare and explore the relationship between each metal ion and MR.

From the work presented in this thesis, we can see that MR has a preference for metal ion activators that can form stable octahedral complexes and that the affinity of these metal ions for the active site of MR correlates to their electronegativity. Once the metal ion is bound to MR, MR will catalyze the racemization of substrate mandelate with relatively equal efficiency regardless of metal ion activator used. A comparison of BzH–metal ion complex formation in free solution, determined by ITC, and BzH affinity for metal–bound MR, determined by inhibition studies, shows either an enhancement to the metal ion–BzH interaction of metal ions with low effective nuclear charge Z_{eff} (i.e., Mg^{2+}) or an attenuation in the interaction of metals with a high Z_{eff} (i.e., Ni^{2+}) when bound to MR to produce a leveling effect. This effect is also observed in the inhibition studies with BzP, where each metal ion–bound variant of MR bound BzP with a similar affinity. The data from chapters 2 and 3 led to the introduction of the 'Hephaestus effect,' a term I have used to describe the ability of a protein to alter the properties of a metal ion.

Comparison of the rate constants (k_1, k_{-1}, k_2, k_{-2}, k_3, k_{-3},) for Mn^{2+}–bound MR, determined using the viscosity variation method, with those of Mg^{2+}–bound MR determined previously (St. Maurice and Bearne, 2002) demonstrate that the metal ion has a slight effect on stabilizing all the transition states accompanying MR catalysis, both internal and external, but not the equilibria for substrate association and product

dissociation. As well, catalysis of the racemization of the alternative substrate TFLA by the metal–bound variants of MR shows that the enzyme is markedly insensitive again to the identity of the metal ion cofactor.

Future experiments should be conducted to determine the binding affinity of BzH for apoMR, this would give an estimate of the binding energy in the absence of metal ion, to help determine the energetic contribution of the metal ion in BzH binding compared to all the other residues in the active site of MR. It would also be worthwhile to obtain a crystal structure of apoMR, to see if it differs significantly from the structure of Mg^{2+}–MR. X–ray absorption spectroscopy could also be conducted on the various metal ion–bound variants of MR to determine the geometric and/or electronic properties of the metal ions when bound to MR. Because the MR activators Co^{2+} and Mn^{2+} are both NMR and EPR active (spins of 7/2 and 5/2, respectively), these techniques may be useful in helping to elucidate whether TFLA binds with outer or inner–sphere coordination to the metal ion.

Site–directed mutagenesis of residues in the active site of MR that coordinate the metal ion to change them to residues that are known to be compatible with other metal ions might further delineate the geometric requirements for metal ion–dependent activation of MR. For example, substitution of the glutamate residues 221 and 247, by histidine residues may create a MR mutant that could utilize Zn^{2+} as a metal ion cofactor. Or, replacement of the metal ion–coordinating residues with positively charged amino acids may produce a 'metal ion–independent' enzyme, as it has been shown in the case of the active site of magnesium–dependent ribonuclease–H (Casereno *et al*., 1995).

Another area worth investigating would be developing a method for observing

Fe^{2+} as an activator of MR. Of course even if this were possible, through introduction of a new buffer system, use of a different pH, or use of a reducing agent that doesn't interfere with the assay, the problem remains that BzH and Fe^{2+} complexes form at a 1:1 ratio and precipitate out of solution. I believe, that with only slight modification, the system and techniques employed in this thesis could be adapted for use on a wide variety of metalloenzymes in order to elucidate the Hephaestus effect in other systems.

References

Adams, J. A., and Taylor, S. S. (1992) Energetic limits of phosphotransfer in the catalytic subunit of cAMP–dependent protein kinase as measured by viscosity experiments, *Biochemistry 31*, 8516–8522.

Agrawal, Y. K., and Tandon, S. G. (1972) Solution stability constants of complexes of benzohydroxamic acid with some divalent metal ions, *J. Inorg. Nucl. Chem. 34*, 1291–1295.

Alberty, R. A., and Hammes, G. G. (1958) Application of the theory of diffusion–controlled reactions to enzyme kinetics, *J. Am. Chem. Soc. 62*, 154–159.

Albery, W. J., and Knowles, J. R. (1976) Evolution of enzyme function and the development of catalytic efficiency, *Biochemistry 15*, 5631–5640.

Babbitt, P. C., Hasson, M.S., Wedekid, J. E., Palmer, D. R., Barret, W. C., Reed, G. H., Rayment, I., Ringe, D., Kenyon, G.L., and Gerlt, J.A. (1996) The enolase superfamily: a general strategy for enzyme-catalyzed abstraction of the α–protons of carboxylic acids, *Biochemistry 35*, 16489-16501.

Baier, F., Chen, J., Solomonson, M., Strynadka, N. C. J., and Tokuriki, N. (2015) Distinct metal isoforms underlie promiscuous activity profiles of metalloenzymes, *ACS Chem. Biol.* ASAP.

Bartlett, P. A., and Marlowe, C. K. (1987) Possible role for water dissociation in the slow binding of phosphorous–containing transition–state–analogue inhibitors of thermolysin, *Biochemistry 26*, 8553–8561.

Bearne, S. L., St. Maurice, M., and Vaughn, M.D. (1999) An assay for mandelate racemase using high–performance liquid chromatography, *Anal. Biochem. 269*, 332-336.

Bearne, S. L., Wolfenden, R. (1997) Mandelate racemase in pieces: effective concentrations of enzyme functional groups in the transition state, *Biochemistry 36*, 1646-1656.

Bégué, J.–P., and Bonnet–Delpon, D. (2008) *Bioorganic and Medicinal Chemistry of Fluorine*, John Wiley and Sons, Inc., Hoboken, NJ.

Bethe, H. A., (1929) Splitting of terms of crystals, *Ann. Physik. 3*, 133-206.

Black, C. B., and Cowan, J. A. (1997) Inert chromium and cobalt complexes as probes of magnesium–dependent enzymes, *Eur. J. Biochem. 243*, 684-689.

Black, C.B., Foster, M., and Cowan, J. A., (1996) Mechanism of metal-promoted catalysis of nucleic acid hydrolysis by *Escherichia coli* ribonuclease H, *J, Biol. Inorg. Chem. 1*, 500-506.

Black, C. B., Huang, H. W., and Cowan, J. A., (1994) Biological coordination chemistry of magnesium, sodium, and potassium ions. Protein and nucleotide binding domains, *Coordn. Chem. Rev. 135/136*, 165-202.

Blacklow, S. C., Raines, R. T., Lim, W. A., Zamore, P.D., and Knowles, J. R. (1988) Triosephosphate isomerase catalysis is diffusion controlled. Appendix: Analysis of triose phosphate equilibria in aqueous solution by 31P NMR, *Biochemistry 27*, 1158–1167.

Bourque, J. R., and Bearne, S. L. (2008) Mutational analysis of the active site flap (20sLoop) of mandelate racemase, *Biochemistry 47*, 566-578.

Bourque, J. R., Burley, R. K., and Bearne, S. L. (2007) Intermediate analogue inhibitors of mandelate racemase: *N*–hydroxyformanilide and cupferron. *Bioorg. Med. Chem. Lett. 17*, 105-108.

Briggs, G. E., and Haldane, J. B. S. (1925) A note on the kinetics of enzyme action, *Biochem. J. 19*, 338.

Britton, H. G. (1973) Methods of determining rate constants in single–substrate–single–product enzyme reactions, *Biochem. J. 133*, 255–261.

Britton, K. L., Langridge, S. J., Baker, P. J., Weeradechapon, K., Sedeinkova, S. E., De Lucas, J. R., Rice, D. W., and Turner, G. (2000) The crystal structure and active site location of isocitrate lyase fom the fungus *Aspergillus nidulans*. *Structure 8*, 349-362.

Brouwer, A. C., and Kirsch, J. F. (1982) Investigation of diffusion–limited rates of chymotrypsin reactions by viscosity variation, *Biochemistry 21*, 1302–1307.

Burley, R. K., and Bearne, S. L. (2005) Inhibition of mandelate racemase by the substrate –intermediate–product analogue 1,1–diphenyl–1–hydroxymethylphosphonate. *Bioorg. Med. Chem. Lett. 15*, 4342-4344.

Casareno, R., Li, D., and Cowan, J. A. (1995) Rational redesign of a metal–dependent nuclease. Engineering the active site of magnesium–dependent ribonuclease–H to form an active "metal–independent' enzyme. *J. Am. Chem. Soc. 117*, 11011–11012.

Cleland, W. W. (1963) The kinetics of enzyme–catalyzed reactions with two or more substrates or products: I. Nomenclature and rate equations, *Biochim. Biophy. Acta 67*, 104-137.

Clugston, S. L., Barnard, J. F. J., Kinach, R., Miedema, D., Ruman, R., Daub, E., and Honek, J. F. (1998) Overproduction and characterization of a dimeric non–zinc glyoxalase I from *Escherichia* coli: Evidence for optimal activation by nickel, Biochemistry *37*, 8754–8763.

Cowan, J. A., (1997) Metal-mediated hydrolysis of biological phosphate esters A critical analysis of the essential metal ion stoichiometry for magnesium-dependent nuclease activation, *J. Biol. Inorg. Chem. 2*, 168-176.

Cowan, J. A., (1998) Metal activation of enzymes in nucleic acid biochemistry, *Chem. Rev. 89*, 1067-1087.

Diebler, H., Eigen, M., Ilgenfritz, G., Maas, G., and Winkler, R. (1969) Kinetics and mechanism of reactions of main group metal ions with biological carriers, *Pure Appl. Chem. 20*, 93-115.

Ducommun, Y., Zbinden, D., and Merbach, A. E. (1982) *Helv. Chim. Acta*. 65, 1385.

Dudev, T., Cowan, J. A., and Lim, C. (1999) Competitive binding in magnesium coordination chemistry: water versus ligands of biological interest, *J. Am. Chem. Soc. 121*, 7665-7673.

Dudev, T., and Lim, C. (2006) A DFT/CDM study of metal–carboxylate interactions in metalloproteins: factors governing the maximum number of metal–bound carboxylates, *J. Am. Chem. Soc. 128*, 1553–1561.

Dudev, T., and Lim, C. (2014) Competition among metal ions for protein binding sites: determinants of metal ion selectivity in proteins, *Chem. Rev. 114*, 538–556.

Dokmanić, I., Šikić, M., and Tomić, S. (2008) Metals in proteins: correlation between the metal–ion type, coordination number and the amino–acid residues involved in the coordination, *Acta. Cryst. D64*, 257–263.

Eigen, M. (1963) Fast elementary steps in chemical reaction mechanisms, *Pure Appl. Chem. 6*, 97-115.

Einsphar, H., and Bugg, C. E. (1984) Crystal structure studies of calcium complexes and implications for biological systems, *Met. Ions Biol. Syst, 17*, 51-97.

Exner, O., Hradil, M., and Mollin, J (1993) Dissociation constants of hydroxamic acids: solvent effects, *Collect. Czech. Chem. Commun. 58*, 1109–1121.

Farkas, E., Enyedy, É. A., and Csóka, H. (2000) Some factors affecting metal ion–monohyroxamate interactions in aqueous solution, *J. Inorg. Biochem, 79*, 205–211.

Fee, J. A., Hegeman, G. D., and Keyon, G. L. (1974) Mandelate racemase from *Pseudomonas putida*. Subunit composition and absolute divalent metal ion requirement, *Biochemistry 13*, 2528-2532.

Felfer, U., Goriup, M., Koegl, M. F., Wagner, U., Larissegger–Scnell, B., Faber, K., and Kroutil, W., (2005) The substrate spectrum of mandelate racemase: minimum structural requirements for substrates and substrate model, *Adv. Synth. Catal. 347*, 951-961.

Felfer, U., Strauss, U. T., Kroutil, W., Fabian, W. M. F., and Faber, K. (2001) Substrate spectrum of mandelate racemase – part 1: variation of the alpha–hydroxy acid moiety, *J. Mol. Catal. B: Enzym. 15*, 213-222.

Fisher, M. L., Albrey, W. J., and Knowles, J. R. (1986) Energetics of proline racemase; racemization of unlabelled proline in the unsaturated, saturated, and oversaturated regimes, *Biochemistry 25*, 2529–2537.

Fisher, M. L., Albrey, W. J., and Knowles, J. R. (1986) Energetics of proline racemase; tracer perturbation experiments using 14C proline that measure the interconversion rate of the two forms of free enzyme, *Biochemistry 25*, 2538–2542.

Fisher, M. L., Belasco, J. G., Bruice, T. W., Albrey, W. J., and Knowles, J. R. (1986) Energetics of proline racemase; transition–state fractionation factors for the two protons involved in the catalytic steps, *Biochemistry 25*, 2543–2551.

Frausto da Silva, J. J. R., and Williams, R. J. P. (1991) *The Biological Chemistry of the Elements. The Inorganic Chemistry of Life*, Clarendon Press: Oxford, pp 244-245.

Frey, C. M., and Stuehr, J. E. (1972) Interactions of divalent metal ions with inorganic and nucleotide phosphates. I. Thermodynaimcs, *J. Am. Chem. Soc. 94*, 8898–8904.

García, B., Ibeas, S., Leal, J. M., Secco, F., Venturini, M., Senent, M. L., Niño, A., and Munõz, C. (2005) Conformations, protonation sites, and metal complexation of benzohydroxamic acid. A theoretical and experimental study, *Inorg. Chem. 44*, 2908–2919.

Gasteiger, E., Hoogland, C., Gattiker, A., Duvaud, S., Wilkins, M. R., Appel, R. D., and Bairoch, A. (2005) Protein identification and analysis tools on the ExPASy server, *The proteomics protocols handbook,* Humana press. John M. Walker (ed). Pp. 571–607.

Gansalus, C. F., Gunsalus, I. C., and Stanier, R. Y. (1953b) The enzymatic conversion of mandelic acid to benzoic acid III: Fractionation and properties of the soluble enzymes, *J. Bacteriol. 66*, 548-553.

Gerlt, J. A., and Gassman, P. G. (1993) Understanding the rates of certain enzyme-catalyzed reactions: proton abstraction from carbon acids, acyl-transfer reactions, and displacement reactions of phosphodiesters, *Biochemistry 32*, 11943-11952.

Grady, J. K., Chasteen, N. D., and Harris, D. C. (1988) Radicals from "Good's" buffers, *Anal. Biochem. 173*, 111–115.

Griffith, J. S., and Orgel, L. E. (1957) Ligand field theory, *Q. Rev. Chem. Soc. 11*, 381–383.

Gunsalus, I. C., Gansalus, C. F., and Stanier, R. Y. (1953a) The enzymatic conversion of mandelic acid to benzoic acid I: gross Fractionation of the system into soluble and particulate components, *J. Bacteriol. 66*, 538-542.

Guthrie, J. P., and Kluger, R. (1993) Electrostatic stablization can explain the unexpected acidity of carbon acids in enzyme–catalyzed reactions, *J. Am. Chem. Soc. 115*, 11569–11572.

Hale, S. P., Poole, L. B., and Gerlt, J. A. (1993) Mechanism of the reaction catalyzed by staphylococcal nuclease: identification of the rate–determing step, *Biochemistry 32*, 7479–7487.

Han, L. B., Schimandle, C. M., Davison, L. M., and Jagt, D. L. V. (1977) Comparative kinetics on Mg^{2+}, Mn^{2+}, Co^{2+}, and Ni^{2+}–activated glyoxalase I. Evaluation of the role of the metal ion, *Biochemistry 16*, 5478–5484.

Hansen, D. K., Webb, H., Nielson, J. W., Harris, P., Winther, J. R., and Willemoës, M. (2014) Mutational analysis of divalent metal ion binding in the active site of class II α–mannosidase from *Sulfolobus solfataricus*, *Biochemistry 54*, 2032–2039.

Hasson, M. S., Schlichting, I., Moulai, J., Taylor, K., Barrett, W., Kenyon, G. L., Babbitt, C. P., Gerlt, J. A., Petsko, G. A., and Ringe, D. (1998) Evolution of an enzyme active site: The structure of a new crystal form of muconate lactonizing enzyme compared with mandelate racemase and enolase, *Proc. Natl. Acad. Sci. 95*, 10396–10401.

Hay, R. W., (1984) *Bio–inorganic chemistry*, John Wiley and Sons, New York.

Hegeman, G. D. (1970a) Mandelate racemase (*Pseudomonas putida*), *Methods Enzymol. 17*, 670-674.

Hegeman, G. D., Rosenberg, E. Y., and Kenyon G. L. (1970b) Mandelic acid racemase from *pseudomonas putida*. Purification and properties of the enzyme, *Biochemistry 9*, 4029-4036.

Hoggett, J. G., and Kellet, G. L. (1976) Yeast hexokinase. A fluorescence temperature–jump study of the kinetics of the binding of glucose to the monomer forms of hexokinases P–I and P–II, *Eur. J. Biochem. 68*, 347–353.

Helin, S., Kahn, P. C., Guha, B. L., Mallows, D. G., and Goldman, A. (1995) The refined X–ray structure of muconate lactonizing enzyme from *Pseudomonas putida* PRS2000 at 1.85 Å resolution, *J. Mol. Biol.* 254, 918–941.

Helm, L., and Merbach, A. E. (1999) Water exchange on metal ions: experiments and simulations, *Coord. Chem. Rev. 187*, 151–181.

Irving, H. M. N. H., and Williams, R. J. P., (1953) The stability of transition metal complexes, *J. Chem. Soc.* 3192-3120.

IUPAC (1997). Compendium of Chemical Terminology, 2nd ed. (the "Gold Book"). Compiled by A. D. McNaught and A. Wilkinson. Blackwell Scientific Publications, Oxford.

Jahn, H. A., and Teller, E. (1937) Stability of polyatomic molecules in degenerate electronic states I–orbital degeneracy, *Proc. Roy. Soc. A*, *161*, 220–235.

Juranić, N., Niketić, S. R., Andjelković, K., and Juranić, I. (1992) General relationship between ring structural and pseudorotational parameters of five-member rings. Application to aminocarboxylato chelates in cobalt(III) complexes, *J. Mol. Struct. 271*, 209-226.

Kallarakal, A. T., Mitra, B., Kozarich, J. W., Gerlt, J. A., Clifton, J. G., Petsko, G. A., and Kenyon, G. L. (1995) Mechanism of the reaction catalyzed by mandelate racemase: structure and mechanistic properties of the K166R mutant, *Biochemistry 34*, 2788-2797.

Kenyon, G. L., Gerlt, J. A., Petsko, G. A., and Kozarich, J. W. (1995) Mandelate racemase: Structure-function studies of a pseudosymmetric enzyme, *Acc. Chem. Res. 28*, 178-186.

Khalil, M. M., and Fazary, A. E. (2004) Potentiometric studies on binary and ternary complexes of di– and trivalent metal ions involving some hydroxamic acids, amino acids and nucleic acid components, *Monatsh. Chem. 135*, 1455–1474.

Kluger, R., and Chin, J. (1978) Rates of formation and decomposition of tetrahedral intermediates in the hydrolysis of dimethyl aroylphosphonates. Substituent effects on a model for carboxylate ester hydrolysis., *J. Am. Chem. Soc. 100*, 7382–7388.

Kurz, J. L. (1963) Transition state characterization for catalyzed reactions, *J. Am. Chem. Soc. 85*, 987-991.

Kurz, L. C., Weitkamp, E., and Frieden, C. (1987) Adenosine deaminase: viscosity studies and the mechanism of binding of substrate and of ground– and transition–state analogue inhibitors, *Biochemistry 26*, 3027–3032.

Landro, J. A., Gerlt, J. A., Kozarich, J. W., Koo, C. W., Shah, V. J., Kenyon, G. L., Neidhart, D. J., Fujita, S., and Petsko, G. A. (1994) The role of lysine 166 in the mechanism of mandelate racemase from *Pseudomonas putida*: mechanistic and crystallographic evidence for stereospecific alkylation by (*R*)-α-phenylglycidate, *Biochemistry 33*, 635-643.

Landro, J. A., Kallarakal, A. T., Ransom, S. C., Gerlt, J. A., Kozarich, J. W., Neidhart, D. J., and Kenyon, G. L. (1991) Mechanism of the reaction catalyzed by mandelate racemase. 3. Asymmetry in reactions catalyzed by the H297N mutant, *Biochemistry 30*, 9274-9281.

Lawrance, G. A., (2010) *Introduction to coordination chemistry*, John Wiley and Sons, West Sussex.

Leinhard, G. E. (1973) Enzymatic catalysis and transition-state theory, *Science 180*, 149-154.

Li, Y., and Zamble, D.B., (2009) Nickel homeostasis and nickel regulation: an overview, *Chem. Rev. 109*, 4617–4643.

Lietzan, A. D., Nagar, M., Pellmann, E. A., Bourque, J. R., Bearne, S. L., and St. Maurice, M. (2012) Structure of mandelate racemase with bound intermediate analogues benzohydroxamate and cupferron, *Biochemistry 51*, 1160-1170.

Lumry, P., and Erying, H. (1954) Conformation changes of proteins, *J. Phy. Chem, 58*, 110–120

Mader, M. M., and Bartlett, P. A. (1997) Binding energy and catalysis: the implications for transition–state analogs and catalytic antibodies, *Chem. Rev. 97*, 1281-1301.

Maggio, E. T., Kenyon, G. L., Mildvan, A. S., and Hegeman, G. D. (1975) Mandelate racemase. V. Mandelate racemase from Pseudomonas putida. Magnetic resonance and kinetic studies of the mechanism of catalysis, *Biochemistry 14*, 1131-1139.

Maguire, M. E., and Cowan, J. A., (2002) Magnesium chemistry and biochemistry, *Biometals*, *15*, 203-210.

Martell, A. E., Hancock, R. D., and Motekaitis, R. J. (1994) Factors affecting stabilities of chelate, macrocyclic and macrobicyclic complexes in solution, *Coord. Chem. Rev*, *133*, 39-65.

Martin, M. E., Byers, B. R., Olson, M. O. J., Salin, M. L., Arceneaux, J. E. L., and Tolbert, C. (1986) A *Streptococcus mutans* superoxide dismutase that is active with either manganese or iron as a cofactor, *J. Biol. Chem. 261*, 9361–9367.

Martin, R. B. (1998) Metal ion stabilities correlate with electron affinity rather than hardness or softness, *Inorg. Chim. Acta 283*, 30–36.

Mattei, P., Kast, P., and Hilvert, D. (1999) *Bacillus subtilis* chorimate mutase is partially diffusion–controlled, *Eur. J. Biochem. 261*, 25–32.

Min He, M., Clugston, S. L., Honek, J. F., and Matthews, B. W. (2000) Determination of the structure of *Escherichia coli* glyoxalase I suggests a structural basis for differential metal activation, *Biochemistry 39*, 8719–8727.

Mitra, B., Kallarakal, A. T., Kozarich, J. W., Gerlt, J. A., Clifton, J. G., Petsko, G. A., and Kenyon, G. L. (1995) Mechanism of the reaction catalysed by mandelate racemase: importance of electrophillic catalysis by glutamic acid 317, *Biochemistry 34*, 2777-2787.

Morgan, G. T., and Drew, H. D. K. (1920) Researches on residual affinity and co-ordination. Part II. Acetylacetones of selenium and tellurium, *J. Chem. Soc.*, *117*, 1456–1465.

Mulliken, R. S. (1935) Electronic structures of molecules XI. Electroaffinity, molecular orbitals and dipole moments, *J. Chem. Phys. 3*, 573–585.

Nagar, M., Narmandakh, A., Khalak, Y., and Bearne, S. L. (2011) Redefining the minimal substrate tolerance of mandelate racemase. Racemization of trifluorolactate. *Biochemistry 50*, 8846-8852.

Nagar, M., Lietzan, A. D., St. Maurice, M., and Bearne, S. L. (2014) Potent inhibition of mandelate racemase by a fluorinated substrate–product analogue with a novel binding mode. *Biochemistry 53*, 1169-1178.

Narmandakh, A., and Bearne, S. L. (2010) Purification of recombinant mandelate racemase: improved catalytic activity, *Protein Expr. Purif. 69*, 39–46.

Neidhart, D. J., Howell, P. L., Petsko, G. A., Powers, V. M., Li, R. S., Kenyon, G. L., and Gerlt, J. A. (1991) Mechanism of the reaction catalyzed by mandelate racemase. 2. Crystal structure of mandelate racemase at 2.5-Å resolution: identification of the active site and possible catalytic residues, *Biochemistry 30*, 9264-9273.

Neidhart, D. J., Powers, V. M., Kenyon, G. L., Tsou, A. Y., Ransom, S. C., Gerlt, J. A., and Petsko, G. A. (1988) Preliminary X-ray data on crystals of mandelate racemase, *J. Biol. Chem. 263*, 9268-9270.

Nielson, J. W., Poulsen, N.R., Johnsson, A., Winther, J. R., Stipp, S. L., and Willemoes, M. (2012) Metal ion dependent catalytic properties of *Sulfolobus solfataricus* class II α–mannosidase, *Biochemistry 51*, 8039–8046.

Odaka, M., Kobayashi, M, (2013) Encyclopedia of Metalloproteins; Uversky, V. N., Kretsinger, R. H., Permyakov, E. A., Eds.; Springer: New York, p. 670.

Parekh, P. C., Manon, S. K., and Agrawal, Y. K. (1989) The thermodynamic metal–ligand stability constants of hydroxamic acids with some divalent metal ions, *J. Chem. Soc. Perkin Trans. II*, 1117–1123.

Parr, R. G., Donnelly, R. A., Levy, M., and Palke, W. E. (1978) Eletronegativity: The density functional viewpoint, *J. Chem. Phys. 68*, 3801–3807.

Pauling, L. (1948) Chemical achievement and hope for the future *Am. Sci.* 36, 50–58.

Pearson, R. G., (1963) Hard and soft acids and bases, *J. Am. Chem. Soc.* 85, 3533-3539.

Pearson, R.G., (1988) Absolute electronegativity and hardness: Application to inorganic chemistry. *Inorg. Chem. 27*, 734–740.

Powers, V. M. (1989) Ph. D. Thesis, University of California, San Francisco.

Powers, V. M., Koo, C. W., Kenyon, G. L., Gerlt, J. A., and Kozarich, J. W. (1991) Mechanism of the reaction catalyzed by mandelate racemase. 1. Chemical and kinetic evidence for a two-base mechanism, *Biochemistry 30*, 9255-63.

Pocker, Y., and Janjic, N. (1987) Enzyme kinetics in solvents of increased viscosity. Dynamic aspects of carbonic anhydrase catalysis, *Biochemistry 26*, 2597–2606.

Price, N.M., and Morel, M.M. (1990) Cadmium and cobalt substitution for zinc in a marine diatom, *Nature* 344, 658–660.

Quinn, C. F., (2010) Analyzing ITC data for the enthalpy of binding metal ions to ligands, *TA instruments*, MCAPN–2010–02.

Radzicka, A., and Wolfenden, R. (1995) A Proficient Enzyme, *Science 267*, 90-93

Ransom, S. C., Gerlt, J. A., Powers, V. M., and Kenyon, G. L. (1988) Cloning, DNA sequence analysis, and expression in Escherichia coli of the gene for mandelate racemase from Pseudomonas putida, *Biochemistry 27*, 540-545.

Romani, A. M. P. (2011) Cellular magnesium homeostasis, *Arch. Biochem. Biophys. 512*, 1–23.

Rulíšek, L., and Vondrášek, J. (1998) Coordination geometries of selected transition metal ions (Co^{2+}, Ni^{2+}, Cu^{2+}, Zn^{2+}, Cd^{2+}, and Hg^{2+}) in metalloproteins, *J. Inorg. Biochem. 71*, 115–127.

Schafer, S. L., Barret, W. C., Kallarakal, A. T., Mitra, B., Kozarich, J. W., Gerlt, J. A. Clifton, J.G., Petsko, G. A., and Kenyon, G. L. (1996) Mechanism of the reaction catalyzed by mandelate racemase: structure and mechanistic properties of the D270N mutant, *Biochemistry 35*, 5662–5669.

Schramm, V. L. (1998) Enzymatic transition states and transition state analog design, *Annu. Rev. Biochem. 67*, 693-720.

Schramm, V. L. (1986) *Manganese in Metabolism and enzyme function*; Academic Press: Orlando, Fl.

Shannon, R.D. (1976) Revised effective ionic radii and systematic studies of interatomic distances in halides and chalcogenides, *Acta. Cryst. A32*, 751–767.

Sharp, T. R., Hegeman, G. D., and Kenyon, G. L. (1979) A direct kinetic assay for mandelate racemase using circular dichroic measurements, *Anal. Biochem. 94*, 329-334.

Segel, I. H. (1993) in *Enzyme kinetics* pp 34–35, John Wiley and Sons, New York.

Siddiqi, F., Bourque, J. R., Jiang, H., Gardner, M., St. Maurice, M., Blouin, C., and Bearne, S. L., (2005) Perturbing the hydrophobic pocket of mandealte racemase to probe phenyl motion during catalysis *Biochemistry 44*, 9013-9021.

Simopoulos, T. T., and Jencks, W. P. (1994) Alkaline phosphatase is an almost perfect enzyme, *Biochemistry 33*, 10375–10380.

Stanier, R. Y. (1950) Problems of bacterial oxidative metabolism, *Bacteriol. Rev 14*, 179-191.

Stanier, R.Y, Gunsalus, I. C., and Gansalus, C. F. (1953) The enzymatic conversion of mandelic acid to benzoic acid II: Properties of the particulate fractions, *J. Bacteriol. 66*, 543-547.

St. Maurice, M., and Bearne, S. L. (2000) Reaction intermediate analogues for mandelate racemase: interaction between Asn 197 and the α-hydroxyl of the substrate promotes catalysis, *Biochemistry 39*, 13324-13335.

St. Maurice, M., and Bearne, S. L. (2002) Kinetics and thermodynamics of Mandelate racemase catalysis, *Biochemistry 41*, 4048-4058.

St. Maurice, M., Bearne, S. L., Lu, W., and Taylor, S. D. (2003) Inhibition of mandelate racemase by α-fluorobenzylphosphonates, *Bioorg. Med. Chem. Lett. 13*, 2041-2044.

St. Maurice, M., and Bearne, S. L. (2004) Hydrophobic nature of the active site of mandelate racemase, *Biochemistry 43*, 2524-2532.

Slater, J. C. (1930) Atomic shielding constants, Phys. Rev. *36*, 57–64.

Tadolini, B. (1987) Iron autoxidation in mops and hepes buffers, *Free Radic. Res. Commun. 3*, 149–160.

Thompson, T. B., Garrett, J. B., Taylor, E. A., Meganathan, R., Gerlt, J. A., and Rayment, I. (2000) Evolution of enzymatic activity in the enolase superfamily: Structure of *o*–succinylbenzoate synthase from *Eschericia coli* in complex with Mg^{2+} and *o*–succinylbenzoate, *Biochemistry 39*, 10662–10676.

Tulsi, N. S., Downey, A. N., and Cairo, C. W. (2010) A protected L–bromophosphonomethylphenylalanine amino acid derivative (BrPmp) for synthesis of irreversible protein tyrosine phosphatase inhibitors, *Bioorg. Med. Chem. 18*, 8679–8686.

Vallee, B. L., and Williams, R. J. P. (1968) Metalloenzymes: the entatic nature of their active sites, *Proc. Nat. Acad. Sci. 59*, 498–505.

Vallet, V., Wahlgren, U., and Grenthe, I. (2003) Chelate effect and thermodynamics of metal complex formation in solution: a quantum mechanical study, *J. Am. Chem. Soc. 125*, 14941–14950.

Van den Elsen, J. M., Kuntz, D. A., and Rose, D. R. (2001) Structure of golgi α–mannosidase II: A target for inhibition of growth and metastasis of cancer cells, *EMBO J. 20*, 3008–3017.

Waldron, K. J., Rutherford, J. C., Ford, D., and Robinson, N. J. (2009) Metalloproteins and metal sensing, *Nature 460*, 823–830.

Wang, G. P., Cahill, S. M., Liu, X., Girvin, M.E., and Grubmeyer, C. (1999) Motional dynamics of the catalytic loop in OMP synthase, *Biochemistry 38*, 284–295.

Weil-Malherbe, H. (1966) Some properties of mandelate racemase from *Pseudomonas fluorescens*, *Biochem J. 101*, 169-175.

Welch, K. D., Davis, Z., and Aust, S. D. (2002) Iron autoxidation and free radical generation: effects of buffers, ligands and chelators, *Arch. Biochem. Biophy. 397*, 360–369.

Whitman, C. P., Hegeman, G. D., Cleland, W. W., and Kenyon, G. L. (1985) Symmetry and asymmetry in mandelate racemase catalysis, *Biochemistry 24*, 3936-3942.

William, R. J. P., (1985) Metallo–enzyme catalysis: the entatic state, *J. Mol. Catal. 30*, 1–26.

William, R. J. P., (1995) Energised (entatic) states of groups and of secondary structures in proteins and metalloproteins, *Eur. J. Biochem. 234*, 363–381.

Wolfenden, R. (1969) Transition state analogues for enzyme catalysis, *Nature 223*, 704-705.

Wolfenden, R. (1972) Analog approaches to the structure of the transition state in enzyme reactions, *Acc. Chem. Res. 5*, 10-18.

Yu, Q., Salhi, C. A., Ambundo, E. A., Heeg, M. J., Ochrymowycz, L. A., and Rorabacher, D. B. (2001) Direct evidence for a geometrically constrained "entatic state" effect on copper (II/I) electron–transfer kinetics as manifested in metastable intermediates, *J. Am. Chem. Soc. 123*, 5720–5729.

Zhong, W., Kuntz, D.A., Ember, B., Singhe, H., Moremen, K.W., Rose, D.R., and Boons, G.J. (2008) Probing the substrate specificity of golgi alpha–mannosidase II by use of synthetic oligosacchirides and a catalytic nucleophile mutant, *J. Am. Chem. Soc. 130*, 8975–8983.